VAWT Dynamic Stall Model tuning using URANS

Mathis De Vusser

Delft University of Technology

VAWT Dynamic Stall Model tuning using URANS

by

Mathis De Vusser

to obtain the degree of Master of Science
at the Delft University of Technology,
to be defended publicly on Friday January 23 2026 at 10:30 AM.

Student number:	5222591	
Project duration:	April, 2025 – January, 2026	
Thesis committee:	D.A. von Terzi	TU Delft, supervisor
	A. Sciacchitano	TU Delft, chair
	S.J. Hulshoff	TU Delft

TU Delft

Abstract

Vertical-axis wind turbine (VAWT) blades experience large and continuous variations in inflow angle of attack and velocity over a turbine revolution, leading to unsteady aerodynamic effects such as dynamic stall. In aero-elastic tools for VAWT power and load prediction, these effects are often modelled using semi-empirical dynamic stall models, such as the Beddoes-Leishman and Risø models. These models rely on a set of airfoil-specific tuning parameters, which can influence the predicted power coefficient of a floating MW-scale VAWT by more than 5%. Historically, these parameters have been determined using experimental wind tunnel data, which is not readily available for a wide range of airfoils. This thesis investigates whether URANS-based computational fluid dynamics (CFD) can partially or fully replace experimental wind tunnel data for the tuning of semi-empirical dynamic stall models for VAWT applications.

Unsteady Reynolds-averaged Navier-Stokes simulations using an incompressible k-ω SST turbulence model are first assessed for their ability to reproduce unsteady airfoil aerodynamics. It is found that the URANS model can accurately replicate the magnitude, phase, and frequency content of the experimental lift response of a pitching NACA0018 airfoil in attached-flow conditions. As a result, URANS simulations are shown to be suitable for determining the four parameters associated with attached-flow unsteadiness in the semi-empirical Risø dynamic stall model. However, the two remaining time-lag parameters cannot be identified with sufficient confidence, as the incompressible URANS approach is unable to accurately capture the separated-flow regimes and compressibility effects governing these parameters. Experimental data is therefore required to tune this subset of the model parameters.

Based on these findings, multiple tuning strategies are evaluated. A physics-informed hybrid approach is proposed, in which attached-flow parameters are determined using URANS simulations, while parameters governing separated-flow dynamics and compressibility effects are calibrated using experimental data. In addition, two optimisation-based tuning strategies are considered: one minimising the global error over the full unsteady lift response, and one optimising a set of key aerodynamic metrics, including the maximum lift coefficient, the angle of attack at maximum lift, and the phase error. All tuning strategies are evaluated at both the airfoil and the turbine level, demonstrating that relatively small differences in airfoil-level unsteady response can lead to significant differences in predicted VAWT power output when integrated over a full turbine rotation. The results show that while URANS-based CFD cannot fully replace experimental data for dynamic stall model tuning, a hybrid CFD–experimental approach provides a practical method for reducing experimental dependency in VAWT aero-elastic modelling.

Preface

The completion of this thesis would not have been possible without the support of others. First, I would like to thank my supervisor at SeaTwirl, Johanna Stenmark, for her guidance throughout the project and for ensuring that the results were relevant from both an academic and an industrial standpoint. I would also like to thank the rest of the team at SeaTwirl, especially David Österberg, for their continuous support and valuable input.

Additionally, I would like to thank Dominic von Terzi and Cristina Vitulano for sharing their experience in dynamic stall and CFD, and for encouraging me to think critically about the approach taken.

I would also like to thank Jonas Böstrom for initially hiring me as an intern at SeaTwirl and for offering me this thesis opportunity. I have learned a lot during my time at SeaTwirl and will forever be grateful.

Last, but definitely not least, I would like to thank my family and friends for their support, for always encouraging me, and for listening as I continue to explain topics they likely would not understand anyway.

Mathis De Vusser
January 2026

Contents

List of Figures

List of Tables

Nomenclature

AC	Actuator Cylinder
BL	Beddoes–Leishman
CFD	Computational Fluid Dynamics
DNS	Direct Numerical Simulation
DSM	Dynamic Stall Model
DSV	Dynamic Stall Vortex
HAWT	Horizontal-Axis Wind Turbine
LES	Large-Eddy Simulation
LEV	Leading-Edge Vortex
PIV	Particle Image Velocimetry
RANS	Reynolds-Averaged Navier–Stokes
SST	Shear Stress Transport
TSR	Tip-Speed Ratio
URANS	Unsteady Reynolds-Averaged Navier–Stokes
VAWT	Vertical-Axis Wind Turbine
k	Reduced frequency, $k = \frac{\omega c}{2U_\infty}$
K_c	VAWT pitch-rate parameter, $K_c = \frac{c}{2R}$
Re	Reynolds number, $Re = \frac{U_\infty c}{\nu}$
α	Angle of attack
α_0	Zero-lift angle of attack
α_{stall}	Static stall angle
λ	Tip-speed ratio
ν	Kinematic viscosity
ϕ	Inflow angle
θ	Azimuthal position
ω	Angular velocity of the rotor
ρ	Air density
a	Axial induction factor
A_1, A_2	Attached-flow weighting coefficients (Risø)
b_1, b_2	Time-scale coefficients (Risø)

c	Airfoil chord length
C_D	Drag coefficient
C_L	Lift coefficient
C_N	Normal force coefficient
C_P	Power coefficient
C_T	Tangential force coefficient
$C_{L,\max}$	Maximum lift coefficient
D	Drag force
f	Separation factor
F_n	Normal force per blade
F_t	Tangential force per blade
H	Blade height
k_a	Non-linear loading correction factor
L	Lift force
P	Power output
Q	Torque
R	Rotor radius
t	Time
T_f	Flow separation time constant
T_p	Pressure response time constant
U_∞	Freestream velocity
w_x, w_y	Induced velocity components
x_{cp}	Centre of pressure location

1

Introduction

1.1. Why floating wind energy?

The global energy transition from fossil fuels to renewable energy sources, and the ever-growing energy requirements have boosted the deployment of wind energy in recent years [11]. Until present, wind energy has primarily been harvested through onshore and fixed-bottom offshore installations. These configurations have been proven economically viable and highly competitive with fossil energy sources, especially in regions with favourable wind resources and accessible seabeds. However, as these accessible locations become increasingly saturated, the wind industry is turning its attention to floating offshore wind as the next area of renewable energy development.

According to [12], there exists over 14,000 GW of technically extractable floating wind energy potential in deep waters globally, the majority of which is currently unexplored. To extract wind power in these remote, deep waters, floating wind turbines have emerged. However, floating platforms are still in an early development stage, with fairly limited commercial applications. The advantages are clear, however, with easier access to high wind speed areas and limited visual and noise constraints. However, this move to offshore turbines adds a layer of costs to the development of wind energy systems. The cost, and mainly the reduced Levelised Cost of Energy (LCOE) for floating platforms and their turbines, remain significantly higher than for fixed-bottom turbines, primarily due to the complexities of mooring, maintenance, and dynamic effects due to wind and waves [13].

Equinor's Hywind Scotland and Hywind Tampen projects, the first commercial solutions for offshore floating wind using horizontal-axis wind turbines (HAWT), for instance, demonstrated the feasibility of floating wind but also highlighted economic struggles, with a prime example being the recent tow-to-shore for maintenance [14]. This presents a critical challenge to the scalability of floating wind: without cost-effective operation and maintenance (O&M) strategies in unstable maritime environments, large-scale deployment remains financially constrained.

1.2. Vertical-axis wind turbines

In response to these challenges, alternative turbine architectures such as vertical-axis wind turbines (VAWTs) are being revisited. While historically underutilised in large-scale energy production due to lower efficiency and reliability concerns, VAWTs present unique advantages for offshore floating applications. Their symmetric geometry, lower centre of gravity, and insensitivity to wind direction eliminate the need for yaw mechanisms and allow for simplified platform designs. Moreover, the rotor, gearbox, and generator can be positioned closer to the water surface, facilitating easier access for maintenance.

Despite these advantages, VAWTs have seen limited commercial deployment, largely due to lower reported power extraction at given wind speeds, structural vibrations, and complex flow phenomena that are less well understood compared to their horizontal-axis counterparts. These complex flow phenomena originate from the inherent unsteady nature due to the cyclic motion of VAWTs, which will cause a high variation in angle of attack and inflow velocity. HAWTs, on the contrary, typically operate at a relatively steady, optimised angle of attack. Effects such as dynamic stall are thus more pronounced in VAWT designs, and will majorly impact the power production and structural loads.

However, the recent shift towards floating offshore wind presents an opportunity to re-evaluate the potential of VAWTs within this emerging niche. With fewer stability constraints and the potential for simpler and cheaper floating structures, VAWTs could provide a viable alternative for offshore wind development—provided that their aerodynamic performance and reliability can be improved. [15]

The research is being done in collaboration with SeaTwirl, a Swedish company that is developing a floating VAWT design for remote offshore applications. SeatTwirl aims to use the advantages of VAWTs to good use. The low centre of gravity, fewer moving components and the location of key components near the waterline will facilitate easier operations and design, and thus lower costs, compared to current floating HAWTs. By developing a floating VAWT concept with an integrated floater-rotor, SeaTwirl will aim to overcome some of the major problems associated with VAWTs, such as loads on the shaft bearing. Additionally, due to the SeaTwirl turbine being stall-regulated, it removes the need for a pitching system, which can lead to high costs and failures in both VAWT and HAWT applications. [15]

1.3. Dynamic stall and its modelling

Dynamic stall is a transient and highly non-linear flow phenomenon that occurs when an airfoil is subjected to rapid or cyclic variations in angle of attack. These unsteady variations can lead to features such as the formation and convection of a leading-edge vortex, lagged pressure and lift responses, and a hysteresis in the aerodynamic coefficients. For stall-regulated VAWTs such as SeaTwirl's concept, accurately capturing these effects is essential, as dynamic stall strongly influences peak loads, fatigue accumulation, and overall power performance. The inherently unsteady inflow conditions in VAWTs, driven by their cyclic kinematics, make turbine-level predictions particularly sensitive to the accuracy of the dynamic stall prediction.

Modern aeroelastic simulation tools used for wind turbine design, including DeepLinesWind [16] and QBlade [17], incorporate dynamic stall through semi-empirical models such as the Beddoes-Leishman [10], Øye [18], or Risø [7] formulations. These models attempt to reproduce the unsteady aerodynamic response using state-space representations or lagged response functions. These models require careful tuning of parameters, typically derived from experimental data, to match the physics of a particular airfoil under specific flow conditions.

Conducting such wind-tunnel campaigns for each new airfoil design or Reynolds-number regime remains costly and time-consuming. With the increasing interest in novel rotor architectures such as floating VAWTs, there is a growing need for more flexible and scalable approaches to dynamic stall model tuning. Recent work [19] suggests that Computational Fluid Dynamics (CFD) may offer an alternative to experiments for this purpose. Furthermore, prior studies have demonstrated that CFD, and in particular Unsteady Reynolds-Averaged Navier-Stokes (URANS) simulations, can capture key features of dynamic stall for VAWT-relevant airfoil motions [20].

Despite these developments, a critical gap remains: no systematic comparison has been made between dynamic stall model parameters tuned using experimental data and those obtained from CFD. While URANS produces time-resolved aerodynamic coefficients and is known to reproduce the integral hysteresis behaviour reasonably well, it is fundamentally limited by its reliance on turbulence-averaged flow fields. This prevents the method from fully resolving the fine-scale, three-dimensional vortex dynamics that govern the onset and evolution of dynamic stall. Whether these modelling limitations introduce biases in the derived dynamic stall parameters, and whether such biases are tolerable for aeroelastic simulations of VAWTs, remains unknown.

This thesis addresses this gap by investigating the viability of using CFD-based data for dynamic stall model tuning and by assessing how the resulting parameters compare with those derived from wind-tunnel experiments. In doing so, the work evaluates both the potential benefits and the inherent limitations of replacing experimental data with high-fidelity simulations for the aerodynamic modelling of vertical-axis wind turbines.

1.4. Research questions

The main research question to be answered will be

How does CFD-based tuning of dynamic stall model parameters compare to experimental methods in predicting aerodynamic loads and power performance of vertical-axis wind turbines?

With subquestions to break down the main research question and guide the chapters.

1. Can Unsteady Reynolds-Averaged Navier–Stokes (URANS) simulations reliably capture the dynamic stall characteristics (e.g., hysteresis behaviour, delay in reattachment) required for parameter tuning of semi-empirical models?
2. How do CFD-tuned dynamic stall model parameters compare to experimentally tuned parameters in predicting aerodynamic coefficients under unsteady inflow conditions at the airfoil level?
3. How does the use of CFD-tuned dynamic stall parameters affect the predicted aerodynamic loads, torque, and power output in an aeroelastic VAWT simulation compared to the use of standard parameters?

1.5. Thesis structure

This thesis is organised as follows:

- **Chapter 2: VAWT performance and working principles** Discusses the key aerodynamics and physics in VAWT power production, including tools used for power prediction, and areas for research.
- **Chapter 3: Dynamic Stall** Reviews the physical concept of dynamic stall, as well as different models used to implement dynamic stall effects in aero-elastic solvers. A brief history and limitations of these models are presented.
- **Chapter 4: Numerical Analysis and CFD** Details the computational and analytical methods used in the study, including CFD simulation setup, mesh generation, and turbulence modelling. Also presents a validation of the CFD setup against existing experimental data, followed by a detailed assessment of the accuracy of URANS in capturing key features of dynamic stall.
- **Chapter 5: Tuning and airfoil performance** Provides a method for tuning dynamic stall models using CFD and experimental data. This chapter compares the performance of different tuning methods for dynamic stall models.
- **Chapter 6: Turbine performance:** Investigates how the tuned parameters influence turbine-level predictions when implemented in an aeroelastic solver. Torque, power output, and structural loads are evaluated for various inflow scenarios.
- **Chapter 7 – Conclusions and Recommendations:** Summarises the main findings, addresses the research questions, and offers recommendations for future work, including experimental validation strategies and extensions to other unsteady flow phenomena.

2

Vertical axis wind energy

Vertical-axis wind turbines have a long history of development, starting with Savonius drag-based turbines, to more recent Darrieus lift-based turbines. To date, however, most real-world applications have been at small scales or in urban settings, where the ability to receive wind from any direction without yaw control is a great advantage. Large-scale deployment has been lacking due to a number of factors. VAWTs experience highly unsteady aerodynamic phenomena that are harder to predict and to certify. Additionally, VAWT power coefficients have historically been lower than the more optimised HAWTs. The cyclic loading also introduces some challenges from a structural point of view. [21]

Despite these challenges, VAWTs also offer advantages that become more relevant as the industry moves to offshore (floating) platforms. VAWTs are omnidirectional, which removes the need for a yaw system, and can place heavy generator and gearbox components near deck level, which can simplify maintenance and improve platform stability due to the lower centre of gravity. Their wake behaviour also shows promising signs, with early studies indicating good wind park performance [22] [23].

HAWTs have dominated the global wind energy market in recent times because they achieve high aerodynamic efficiency, with mature control systems and supply chains, and benefit from decades of research and development [24]. However, as rotor sizes keep on growing and projects are moving to floating platforms in deeper waters, HAWTs start to push the boundaries of their design. The nacelle mass high above the waterline increases platform size and cost, yaw and pitch are complicated due to platform motion, and offshore O&M remains a major cost driver. In this context, it is crucial to re-examine different design philosophies, such as VAWTs, as purpose-fit designs for specific (floating) offshore energy generation cases. [15]

In this chapter, a basic introduction to VAWTs will be given. First, floating VAWTs will be introduced in section 2.1, which is the target application for this study. Secondly, basic VAWT aerodynamics and working principles behind the power generation will be presented in section 2.2. Following this, an actuator cylinder model for VAWTs is presented in section 2.3, which is a critical tool in the power prediction of VAWTs. This chapter aims to provide the reader with a basic understanding of aerodynamics and flow phenomena that are experienced by VAWTs in operation.

2.1. Rotor design

Throughout the history of VAWTs, several major design philosophies have been explored. Both on rotor-level and airfoil-level, many options are available. In this section, a short overview of possible rotor geometries and airfoils used in VAWT applications is provided. The type of VAWT analysed in this thesis is also presented.

2.1.1. Rotor geometry

Modern HAWT systems have clearly converged to a dominant, efficient, three-bladed design after years of research. VAWTs have not converged to such a main design. The design space for VAWTs remains very open. There are two main design approaches: drag-based (such as Savonius) and lift-based (such as Darreius) turbines. It has been concluded that lift-based turbines provide a higher power output. Within the lift-driven turbines, there are still a plethora of different options and design shapes available. Some examples are shown in Figure 2.1. Design variables such as the number of blades, height-to-diameter ratio, and blade shapes are still highly variable and differ from application to application.

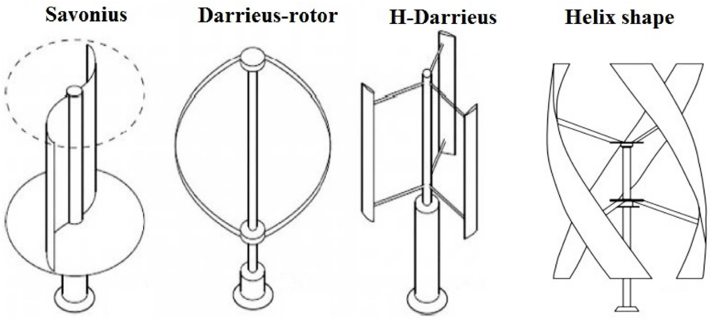

Figure 2.1: Different types of vertical-axis wind turbines, adapted from [1]

Vertical-axis wind turbines also have less need for control systems, since the need for a yaw system is removed. Pitch systems can be included to control the speed of the blade by pitching the airfoil away from the optimal angle of attack. However, due to the very high cyclic loading, this is not common in VAWTs. They are therefore often stall-regulated.

In this study, all analyses will be performed for a three-bladed H-Darrieus rotor. The rotor is stall-regulated. This means that there is no pitching system. The angle of attack experienced by the airfoil will thus only be governed by the tip-speed ratio and the static pitch angle.

2.1.2. VAWT airfoils

Vertical-axis wind turbines have historically employed thick, symmetric airfoils, as the belief was that the same aerodynamic behaviour was required in both the upwind and downwind half of the rotation. Kato showed that this assumption was not valid, and showed that asymmetric airfoils could provide a higher efficiency for VAWTs[25].

In this research, the analyses are performed using a VAWT with a NACA0018 airfoil, which can be seen in Figure 2.2. This airfoil is chosen because there is sufficient open-source experimental data available for both static and dynamic tests. The thickness is also representative of that found in VAWT applications. [2]

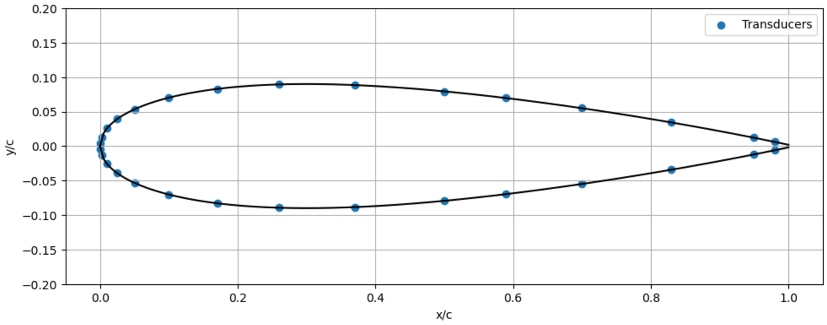

Figure 2.2: NACA0018 airfoil with locations of pressure transducers for the experimental tests performed in [2]

2.2. VAWT aerodynamics

In this section, the basic aerodynamics and power generation mechanisms of VAWTs will be discussed. Different models that can be employed to predict the performance and loading of a VAWT will also be presented. There are two main power generation philosophies, namely drag-driven and lift-driven power generation. Drag-driven VAWTs have considerably lower power coefficients; therefore, only lift-driven power generation will be considered.

2.2.1. Power generation

The power output of a VAWT is related to the torque (Q) generated by aerodynamic forces acting on the blades, and the rotational speed (ω) at which the VAWT is spinning.

$$P = Q\omega \tag{2.1}$$

A first estimate of the power production can be calculated by taking a theoretical blade element approach. The torque is based on the aerodynamic lift and drag produced by the blades. If a two-dimensional cross-section is taken of the rotor, the N airfoils will each produce a lift and drag, given by Equation 2.2 and Equation 2.3.

$$L' = C_L(\alpha)\frac{1}{2}\rho V^2 c \tag{2.2}$$

$$D' = C_D(\alpha)\frac{1}{2}\rho V^2 c \tag{2.3}$$

The lift (L) and drag (D) are then linked to the force tangential to the rotation of the blade by Equation 2.4. With ϕ being the inflow angle.

$$F'_t = L' sin(\phi) - D' cos(\phi) \tag{2.4}$$

Integrating this force, which depends on the azimuthal position of the blade, over a full rotation of the blade, and multiplying it by the respective moment arm of the blade, will yield the torque generated by the full rotor.

$$Q = \frac{1}{2\pi}\int_0^{H_{blade}}\int_0^{2\pi} N_{blades}F'_T(\theta)R(h)d\theta dh \tag{2.5}$$

Combining Equation 2.1 and Equation 2.5, the power outputted by a 2D rotor is given by Equation 2.6

$$P = \frac{\omega}{2\pi}\int_0^{H_{blade}}\int_0^{2\pi} N_{blades}F'_T(\theta)R(h)d\theta dh \tag{2.6}$$

As seen in Equation 2.2 and Equation 2.3, the forces generated by the blade depend on the velocity and angle of attack experienced by the blade. A two-dimensional top-view cross-section of a VAWT can be taken (see Figure 2.3) to determine the inflow velocities and angle of attack at the blades. Figure 2.3 also shows different definitions for azimuthal angles ($\theta = 0$ is where the blades are the furthest upstream), normal and tangential force coefficients, and lift and drag.

For VAWTs, the inflow velocity magnitude and angle of attack vary strongly with the azimuthal angle. The range of angles of attack and velocities is mainly determined by the tip speed ratio $\lambda = \omega R/U_\infty$. The variation in angle of attack and velocity magnitude can be seen in Figure 2.4. Note that this is an idealised case with no wake effects or unsteady effects. Only the variation of the angle of attack and velocity due to the inflow velocity and airfoil motion is presented. This velocity and angle of attack can be used to calculate the loads on the blades.

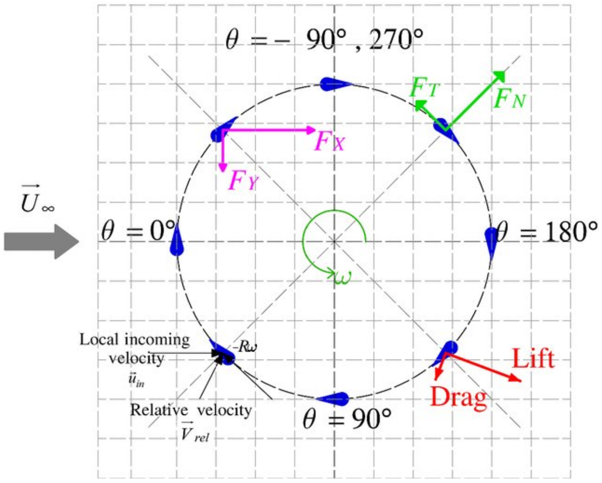

Figure 2.3: Schematic of VAWT forces and velocities, adapted from [3]

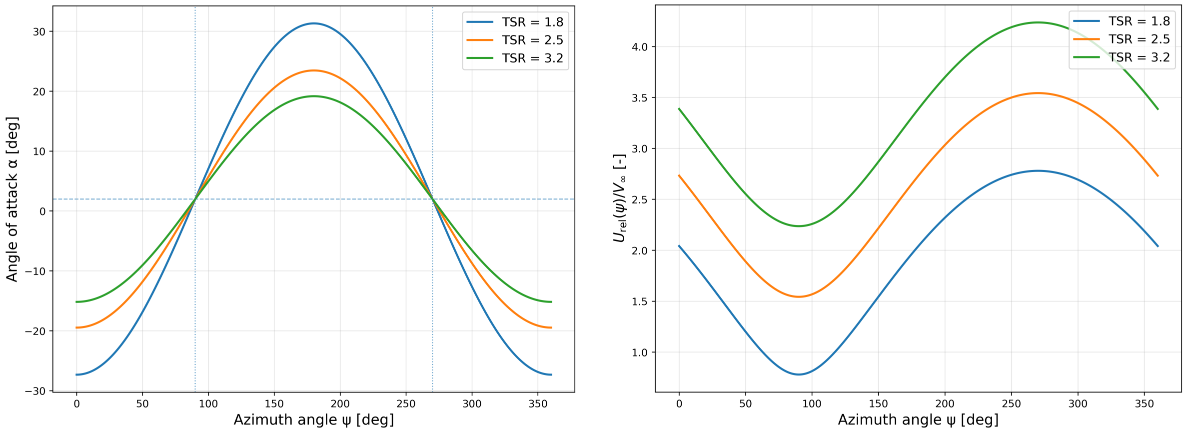

(a) Variation of angle of attack

(b) Relative velocity variation

Figure 2.4: Angle of attack and relative velocity for different tip speed ratios as variation of azimuthal angle, ignoring airfoil wake effects

2.2.2. Non-ideal rotor effects

While Equations 2.2–2.6 provide a first-order prediction of VAWT performance, these relations assume steady, two-dimensional aerodynamics. In reality, the rotor experiences highly unsteady, three-dimensional phenomena that modify both the instantaneous blade forces and the averaged power output. A distinction can be made between phenomena that are common to all finite-span lifting systems, such as tip losses, which reduce the lift generated near the blade ends, interference from struts and supports, which causes an increase in drag, and induced velocities that modify the effective inflow velocity magnitude and angle. Similarly, dynamic inflow creates a time lag in the induced velocity field caused by the finite response time of the wake to changes in blade loading. This results in a delayed adjustment of the wake during transient conditions.[21]

The second category includes effects that are more common in (vertical-axis) wind energy. The cyclic nature of the VAWT motion leads to three main phenomena that influence VAWT power generation. These are flow curvature effects, blade-vortex interactions, and dynamic stall. Dynamic stall originates from the large angle-of-attack excursions experienced, which frequently leads to the effective angle of attack exceeding the static stall angle. Flow curvature is a phenomenon that originates from the curved path of a VAWT airfoil, which affects the local effective angle of attack and pressure distribution [26]. Lastly, blade-vortex interactions will cause an unsteady loading when a blade passes through the wake vortices shed by previous blade passages, or upstream shed vortices. These interactions will amplify unsteady forces and moments, especially at low tip-speed ratios [27].

The combination of these unsteady effects makes the performance prediction of VAWTs highly challenging. Several phenomena, such as tip losses and interference losses, have been researched thoroughly outside of the VAWT context, and can be predicted with reasonable confidence. However, for VAWT applications, phenomena such as blade-vortex interactions and dynamic stall have not been modelled to great detail. Especially, dynamic stall has a major influence on the power prediction of wind turbines [5].

2.3. Actuator cylinder model

In this study, the aerodynamic prediction of VAWTs relies on a 3D actuator cylinder model, based on the actuator cylinder (AC) model developed by [4] and based on the original formulation by [28], but adapted to analyse a three-dimensional rotor. The extension of this model includes the effect of tip losses and junction losses between the blades and the struts connecting the blades and the tower.

The actuator cylinder approach provides a computationally efficient, quasi-steady representation of the rotor aerodynamics by replacing the rotating blades with an equivalent body-force distribution acting on a cylindrical control surface. This model bridges the gap between detailed computational fluid dynamics (CFD) and momentum-theory-based methods.

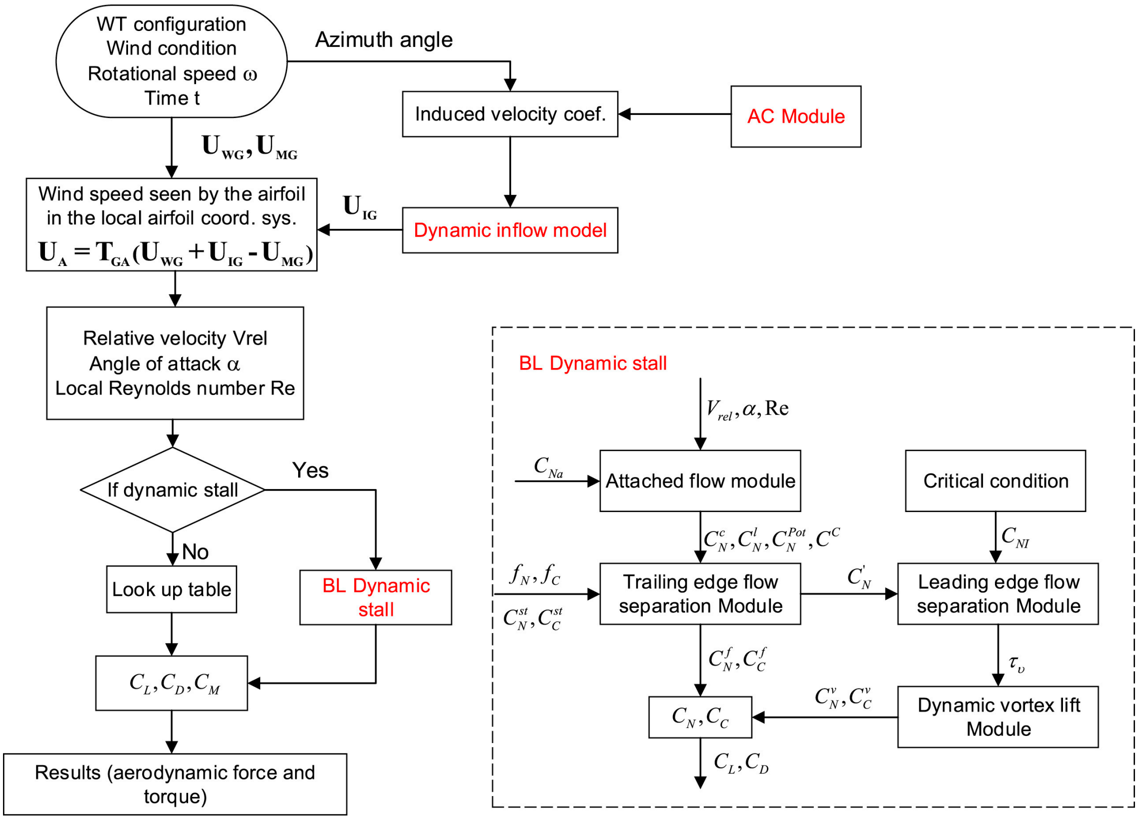

Figure 2.5: Flowchart of the actuator cylinder presented in [4]. Figure adapted from [4]

2.3.1. Model formulation

The actuator cylinder represents the swept area of the rotor as a hollow cylindrical surface of radius R and infinitesimal thickness.

Within this surface, the blades are replaced by a force field that exerts distributed normal and tangential forces on the flow. The model assumes incompressible, steady, two-dimensional flow in the rotor plane, governed by the Euler equations with body forces that correspond to the aerodynamic loading of the blades.

The instantaneous velocity field is determined by the freestream velocity U_∞, and the (normalised) induced velocities w_x and w_y. The induced velocities are influenced by the aerodynamic performance of the actuator cylinder rotor. The local velocity at any point (x, y) can then be expressed in non-dimensional (non-dimensionalised by U_∞) form as:

$$u_x = 1 + w_x \qquad u_y = w_y \tag{2.7}$$

[4] derive a linearised solution for the induced velocities, given in Equation 2.8 and Equation 2.9. This is based on the body forces given by Equation 2.10 and Equation 2.11.

$$
\begin{aligned}
w_x(f) = &-\frac{1}{2\pi}\int_0^{2\pi} Q_n(\theta)\frac{-(x+\sin\theta)\sin\theta+(y-\cos\theta)\cos\theta}{(x+\sin\theta)^2+(y-\cos\theta)^2}\,d\theta \\
&-\frac{1}{2\pi}\int_0^{2\pi} Q_t(\theta)\frac{-(x+\sin\theta)\cos\theta-(y-\cos\theta)\sin\theta}{(x+\sin\theta)^2+(y-\cos\theta)^2}\,d\theta \\
&-Q_n(\arccos y)-Q_t(\arccos y)\frac{y}{\sqrt{1-y^2}} \qquad \text{(In the cylinder and wake)} \\
&+Q_n(-\arccos y)^{**}-Q_t(-\arccos y)\frac{y}{\sqrt{1-y^2}} \qquad \text{(In the wake)}
\end{aligned} \tag{2.8}
$$

$$
\begin{aligned}
w_y(f) = &\frac{1}{2\pi}\int_0^{2\pi} Q_n(\theta)\frac{(x+\sin\theta)\cos\theta+(y-\cos\theta)\sin\theta}{(x+\sin\theta)^2+(y-\cos\theta)^2}\,d\theta \\
&-\frac{1}{2\pi}\int_0^{2\pi} Q_t(\theta)\frac{(x+\sin\theta)\sin\theta-(y-\cos\theta)\cos\theta}{(x+\sin\theta)^2+(y-\cos\theta)^2}\,d\theta
\end{aligned} \tag{2.9}
$$

$$
Q_n(\theta) = \lim_{\epsilon\to 0}\int_{1-\epsilon}^{1+\epsilon} f_n(\theta,r)dr \tag{2.10}
$$

$$
Q_t(\theta) = \lim_{\epsilon\to 0}\int_{1-\epsilon}^{1+\epsilon} f_t(\theta,r)dr \tag{2.11}
$$

In practice, Q_n and Q_t are obtained through a blade-element approach: for each azimuthal position θ, the relative velocity and instantaneous angle of attack are computed, from which the local lift and drag coefficients (C_l, C_D) yield the corresponding blade forces. These forces are then projected onto the cylinder as distributed body forces.

$$
Q_n = \frac{BF_{nB}}{2\pi R\rho U_\infty^2} \tag{2.12}
$$

$$
Q_t = \frac{BF_{tB}}{2\pi R\rho U_\infty^2} \tag{2.13}
$$

Where $B/2\pi$ stands for the number of blades that will serve as time-averaging in one revolution, F_{nB} and F_{tB} are the normal and tangential forces acting on one blade, respectively. R is the radius of the turbine. The forces are non-dimensionalised using ρU_∞^2
Since the aerodynamic forces depend on the induced velocity field, an iterative solution is required:

1. Initialise $w_x, w_y = 0$;
2. Compute the blade-element aerodynamic forces and corresponding volumetric body forces;
3. Solve for the induced velocity field using the integral formulation;
4. Update the local aerodynamic forces and repeat until convergence.

2.3.2. Non-linear loading correction and 3D effects

The linearised solution is valid primarily for lightly loaded rotors. To extend applicability to higher loading, [29] introduced a non-linear correction factor, k_a, which scales the induced velocities to maintain consistency with momentum-theory thrust coefficients:

$$
w_x^{\text{corr}} = k_a w_x^{\text{lin}} \qquad w_y^{\text{corr}} = k_a w_y^{\text{lin}} \tag{2.14}
$$

With k_a being equal to

$$
k_a = \begin{cases} \dfrac{1}{1-a} & (a \leq 0.15) \\ \dfrac{1}{1-a}\,(0.65+0.35\exp[-4.5(a-0.15)]) & (a > 0.15) \end{cases} \tag{2.15}
$$

The derivation of this relationship, as well as the estimation of the induction factor a can be found in [4].

This correction improves the accuracy of thrust and power predictions, particularly at moderate to high tip-speed ratios where the loading on the turbine is higher, and the induced velocity effects are more pronounced.

In addition to the non-linear loading correction, 3D effects such as tip and strut losses have a significant impact on the aerodynamic performance of a wing, and thus the performance of the rotor. The actuator cylinder model assumes an infinitely long rotor, neglecting end effects that arise due to the finite blade span. In reality, the flow near the blade tips is characterised by strong spanwise gradients and the formation of tip vortices, which lead to a reduction in the effective circulation and lift near the blade edges. These losses reduce the overall torque production and modify the induced velocity distribution along the span. This effect will be larger for turbines with relatively low aspect ratios. In the actuator cylinder model employed in the present work, this is implemented using Prandtl's theory, which is described by [30].

Strut interference is another important 3D effect, especially in vertical-axis wind turbines operating at higher tip speed ratios [31] [32]. The presence of support struts introduces additional drag and local flow disturbance on the wing, influencing the local performance near the struts. Depending on the strut geometry and its orientation relative to the free stream, the effect of the strut can not be ignored. In the case of aerodynamically optimised strut design, the struts themselves could have a positive effect on the power production [33] [34].

2.3.3. Dynamic stall implementation

As can be seen in Figure 2.5, the last step in the performance production of the actuator cylinder model is the determination of the aerodynamic force and moment coefficients that the blades experience due to the inflow and induced velocities. In [4] two different paths are proposed, one where a dynamic stall is included and one without. This dynamic stall model (DSM) enables the steady actuator cylinder model to include the prediction of highly unsteady VAWT airfoil phenomena, such as separation delay, vortex shedding, and post-stall reattachment. In [35]the importance of dynamic stall modelling in VAWT was shown, concluding that the loads and performance of VAWTs are highly dependent on dynamic stall (model) behaviour. This can also be seen in Figure 2.6, showing the power coefficient responses for a VAWT with and without the dynamic stall module included.

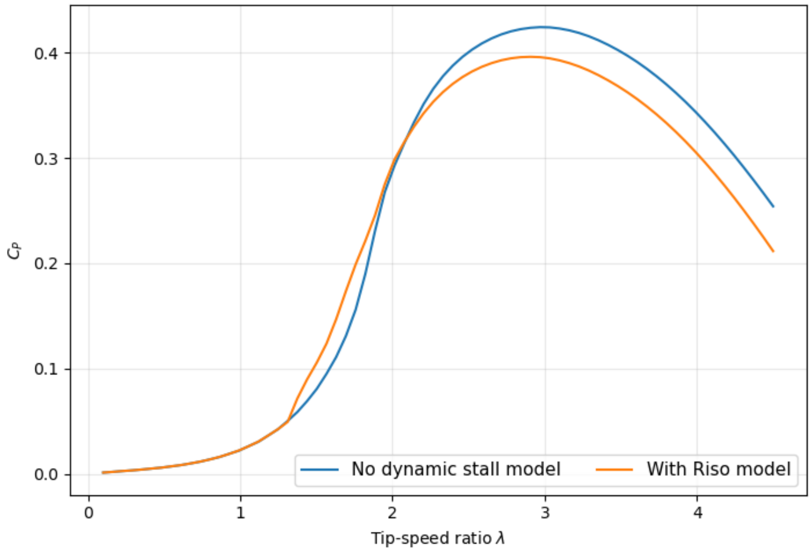

Figure 2.6: Impact of dynamic stall model included in power prediction of actuator cylinder model

Cheng et al. [4] couples the actuator cylinder model with the Beddoes-Leishman dynamic stall model [36]. However, this choice of dynamic stall module is arbitrary and can be chosen based on personal preference.[19] provides a clear overview of different dynamic stall models available, and their assumptions and limitations. Different dynamic stall models have been developed for different applications, for which the most commonly used are the Risø [7], Øye [18], ONERA [37], and many others.[38] provides an assessment for the performance of these different models for HAWT applications.

Extensive studies have been performed to compare different types of dynamic stall models for HAWTS [38], [39], [40]. However, no exhaustive performance review has been carried out in the context of VAWT performance prediction.

An extensive review of the dynamic stall phenomena, including the implementation of dynamic stall models and their applicability and limitations, will be presented in chapter 3. This chapter will also discuss the origins of dynamic stall, and flow and turbine parameters influencing the airfoil response to a dynamic input.

2.3.4. Applications and Limitations

The actuator cylinder model provides a computationally efficient framework to predict the aerodynamic performance of VAWTs. By representing the rotor as a cylindrical control volume, the AC model allows for the estimation of induced velocities and power output based on momentum theory, making it suitable for conceptual design and parametric studies. It has been successfully applied to steady-state analyses and array simulations where computational simplicity is prioritised [41]. When coupled to aero-elastic tools, such as the Deeplines Wind solver [16], the model can provide a first-order aerodynamic input for dynamic simulations. However, due to its reliance on steady induction assumptions, the AC approach inherently neglects unsteady phenomena and wake–rotor feedback effects, which limits its predictive accuracy slightly in typical VAWT operating conditions.

Several studies have identified additional limitations of the AC model. Ferreira et al. [42] observed that the model predicts an increasing power coefficient with thrust coefficient even beyond the physical maximum, a behaviour linked to inaccuracies in the correction of the linear momentum solution under high loading. Cheng et al. [4] similarly reported reduced accuracy at high tip-speed ratios, where empirical corrections become less reliable. Moreover, the model does not inherently resolve wake expansion or dynamic inflow effects, and unsteady mechanisms such as flow curvature and dynamic stall are not represented [21]. Consequently, while the AC model is valuable for steady performance predictions, a more detailed load estimation can be achieved by coupling the AC with a blade element or free-vortex model to capture the cyclic aerodynamic loads on individual blades. This extension is not employed in this thesis due to the additional computational cost and complexity. The AC serves the purpose to analyse the impact of dynamic stall models to a sufficient extent.

3

Dynamic stall

As discussed in chapter 2, vertical axis wind turbine (VAWT) airfoils experience continuously changing inflow conditions during operation. Due to the periodic variation in both the velocity and direction of the apparent wind, the aerodynamic forces acting on the blades exhibit significant unsteady behaviour. This necessitates the inclusion of unsteady aerodynamic effects in the modelling of VAWT performance. Among these effects, dynamic stall plays a crucial role, alongside other phenomena such as flow curvature, dynamic inflow, and blade-vortex interactions. For the scope of this thesis, only dynamic stall will be considered.

This chapter aims to provide a comprehensive overview of the dynamic stall phenomenon, with particular focus on its physical origins and governing parameters. section 3.1 discusses the fundamental mechanisms and influences underlying dynamic stall. Subsequently, section 3.3 reviews the principal dynamic stall models developed in the literature, including their historical context, theoretical formulation, and limitations in practical applications.

3.1. Physical phenomenon

In the literature, dynamic stall is often broadly defined as the unsteady aerodynamic behaviour of airfoils subjected to time-varying inflow conditions, typically without a formal distinction between attached and separated flow regimes. However, a more nuanced view recognises the existence of three distinct flow cases, with varying levels of separation ranging from no separation to full separation. The level of separation depends on the time evolution of the angle of attack, and its maximum values, as defined in [43]. A visualisation of these three types of stall mechanisms can be seen in Figure 3.1.

1. **Attached flow:** The flow remains fully attached throughout the motion, even as the angle of attack varies. The aerodynamic response exhibits minor hysteresis effects due to unsteady circulation, but no large flow separation or stall vortex formation occurs. This regime is often encountered when the instantaneous angle of attack does not exceed the dynamic stall threshold.

2. **Light-moderate stall:** The airfoil momentarily exceeds the dynamic stall angle, leading to flow separation and the formation of a transient dynamic stall vortex (DSV). However, the flow reattaches during the pitch-down or recovery phase. This regime is characterised by moderate hysteresis loops at higher angles of attack and partial loss of aerodynamic efficiency, yet without a persistent separated flow state. According to [44], light stall refers to trailing edge separation, similar to classic static stall.

3. **Deep stall:** The angle of attack surpasses the critical limit beyond which the flow remains fully separated, and reattachment does not occur during the motion cycle. The formation and convection of the DSV produce a sharp overshoot in lift followed by a substantial drop, often accompanied by increased drag and fluctuating moments. The airfoil remains in a stalled condition for a significant portion of the cycle. A large hysteresis is present, following the separated flow in most of

the angle of attack range. [44] describes deep stall as being categorised by mainly leading edge separation. In normal wind energy applications, this will be limited due to a combination of thick airfoils with larger leading edge radii, higher Reynolds numbers, and moderate angle of attack ranges. [45] [46]

Dynamic stall is therefore not a single flow phenomenon with only stalled flow, but a continuum of behaviours with varying degrees of unsteadiness and flow separation. Unsteady attached flows could therefore also be categorised as dynamic stall. The transition between these regimes is governed by parameters such as the mean and oscillatory components of the angle of attack, the reduced frequency, Reynolds number, and airfoil geometry. A visualisation of these different types of stall has been presented in [43] and an adaptation with data from [2] can be seen in Figure 3.1

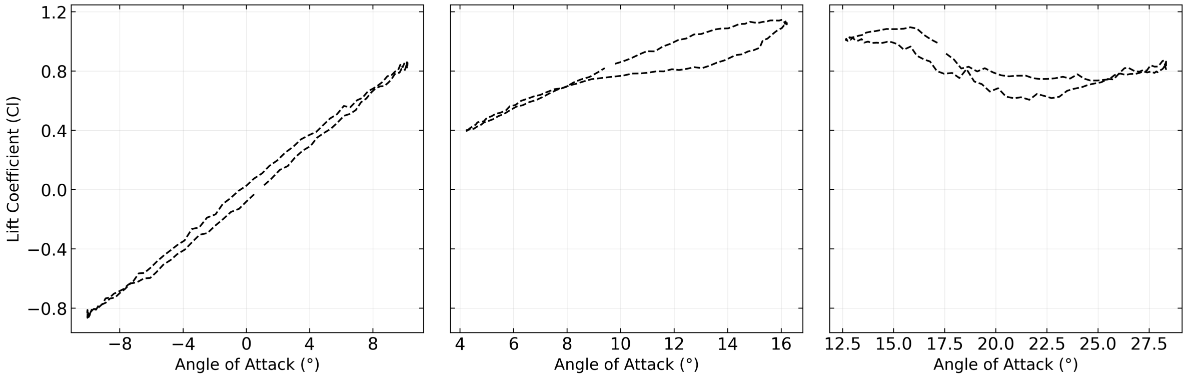

Figure 3.1: Lift coefficient hysteresis loops for three dynamic stall regimes. Attached-flow (left), light-moderate stall (centre), deep stall (right). Own figure, based on data by [2]

Generally, dynamic airfoil motion mainly affects the maximum lift coefficient and the stall angle of an airfoil [47]. This increase in lift and stall angle arises due to the unsteady nature of the flow field during rapid changes in angle of attack. Since the fluid takes a finite amount of time to travel over the airfoil surface, different portions of the airfoil are effectively exposed to different local angles of attack during motion.

When an airfoil pitches up, the leading edge is the first to encounter the increased angle of attack. In contrast, the trailing edge initially experiences a lower, lagging angle of attack due to the delay in the flow. As a result, flow separation near the trailing edge is postponed, and stall is delayed compared to the quasi-steady case. This delay in flow separation leads to an increase in the maximum lift coefficient and a higher stall angle.

Conversely, during a pitching-down motion, the leading edge experiences the reduced angle of attack first, while the trailing edge retains a higher effective angle of attack for a short duration. This causes the separated flow near the trailing edge to persist even at lower angles of attack, thus reducing both the lift coefficient and stall angle compared to steady-state conditions.

[5] shows in detail how the airflow evolves over the airfoil for a pitching airfoil experiencing dynamic stall. This can be seen in Figure 3.2. It shows flow phenomena occurring that will increase the lift generated to values above the static $C_{l_{max}}$.

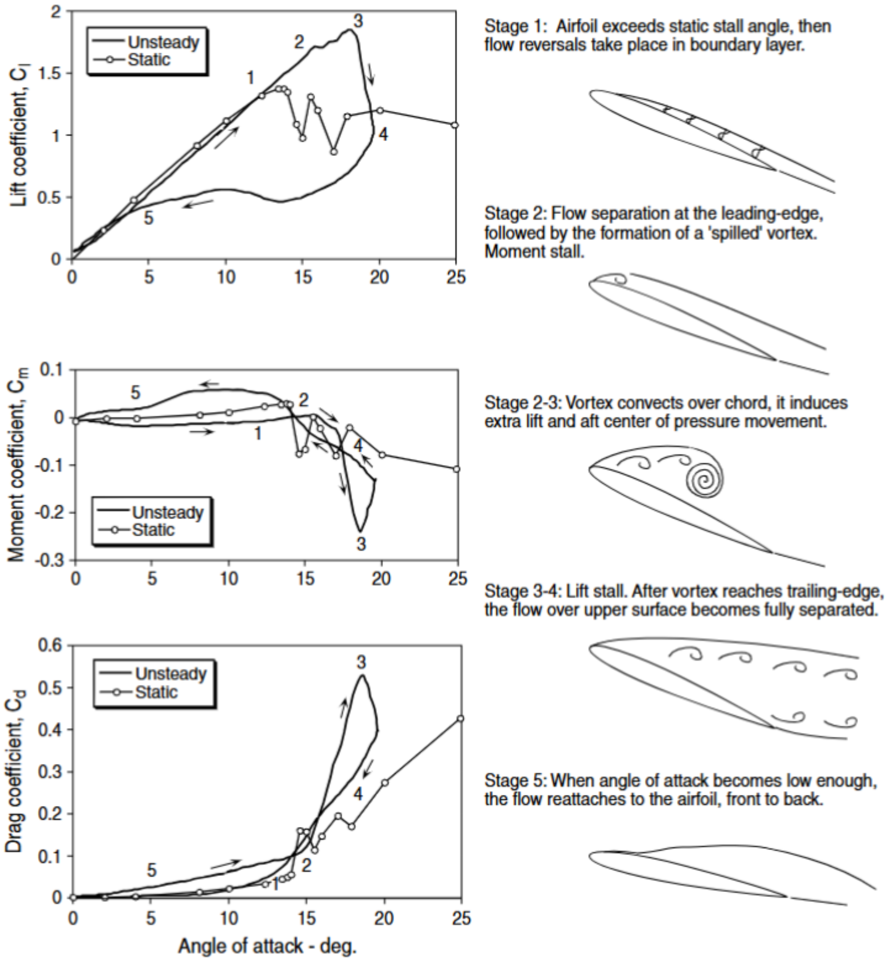

Figure 3.2: Illustration of the unsteady aerodynamic loading and flow field evolution during dynamic stall for a pitching airfoil. Adapted from [5]

As discussed in chapter 2, at higher tip speed ratios, the angle of attack excursion are less, and light-moderate stall will happen. Since the VAWT analysed is a stall-regulated turbine, higher angles of attack will also be experienced (up to $30°$ and more), which happens more in the deep stall region. These high excursions increase the need for accurate dynamic stall modelling. Since these angle of attack excursions reach both positive angles of attack, reattachement is expected.

Dynamic stall occurs at both positive and negative angles of attack. In the case of symmetric airfoils, the effects of positive and negative stall are similar, if not the same. Only for asymmetric airfoils, there is a difference in dynamic stall behaviour. However, this is beyond the scope of this thesis.

3.1.1. Origins of dynamic stall

The phenomenon of dynamic stall can be triggered by various types of unsteady airfoil motion, most notably plunging and pitching . [44] Each induces time-varying effective angles of attack, but through fundamentally different mechanisms.

- **Plunging motion** involves vertical translation of the airfoil normal to the freestream velocity. Although the geometric angle of attack remains constant, the vertical velocity modifies the inflow velocity, effectively modifying the angle of attack experienced by the airfoil. This transient variation can lead to dynamic stall if the rate or magnitude of motion drives the flow into a separated state.

- **Pitching motion**, on the other hand, involves rotational motion of the airfoil about a fixed axis. This motion directly alters the geometric angle of attack, and its effect on the effective inflow angle is amplified by the pitch rate. Pitching is particularly influential in dynamic stall onset, as the pitch rate term introduces a lag between angle of attack and the aerodynamic response, especially on the aft side of the airfoil, inducing overshoot and vortex formation. In VAWT motion, pitching occurs inherently due to the circular motion of the blade. This is irrespective of any active pitching systems included in the design.

Relevance for VAWTs: In vertical-axis wind turbines, the blades naturally experience a periodic variation in apparent wind speed and direction due to their rotation. This results in an effective pitching-like motion, even in the absence of any structural pitching. The angle of attack experienced by the blade varies cyclically and can exceed the static stall limit, particularly at low tip-speed ratios. Therefore, dynamic stall in VAWTs is most appropriately modelled as a response to an effective pitching motion.

While plunging-like effects may occur in the presence of structural flexibility or dynamic inflow modulation, they are secondary compared to the dominant pitching dynamics. Consequently, this thesis considers only the pitching-induced origin of dynamic stall, consistent with both the physics of VAWT blade kinematics and the assumptions underlying widely used dynamic stall models.

3.2. Dynamic stall in VAWTs

The origin of dynamic stall in vertical-axis wind turbines differs slightly from that observed in conventional horizontal-axis configurations. In a VAWT, each blade experiences a continuously varying inflow velocity and direction due to the blade's rotational motion. This periodic variation leads to a cyclic angle of attack that depends on the tip-speed ratio (TSR), azimuthal position, and local induction velocities. As a result, the aerodynamic loading on each blade undergoes strong temporal fluctuations, with the instantaneous angle of attack often exceeding the static stall limit during parts of the revolution. These unsteady effects make dynamic stall an inherent feature of VAWT aerodynamics rather than an uncommon occurrence. Compared to HAWT motion, the angle of attack excursions will also be considerably larger.

Experimental flow-visualisation studies at relatively low Reynolds numbers have shown that the unsteady nature of VAWT aerodynamics leads to distinct dynamic stall phenomena, particularly at lower tip-speed ratios. In the work of Simao Ferreira et al., two-dimensional particle image velocimetry (PIV) was used to visualise the flow around a straight-bladed VAWT [48]. The study demonstrated that, as the TSR decreases, strong leading-edge vortices (LEVs) form and convect over the airfoil during the upwind half of the rotation, producing a significant overshoot in the normal force coefficient. This is also shown in Figure 3.3 [6]. These vortices detach and shed into the wake, leading to large hysteresis loops in the lift–angle of attack relation and highly unsteady aerodynamic loads. This work shows experimental evidence that dynamic stall in VAWTs is not only present but also impacts the aerodynamic response under realistic operating conditions.

Building on this, Buchner et al. provided a detailed overview of the governing parameters underlying dynamic stall in VAWTs [49]. Through PIV measurements for a set of tip speed ratios and Reynolds numbers, they showed that the flow and vortex dynamics cannot be described solely by the tip speed ratio. Instead, the development and strength of the leading-edge vortex are governed by a combination of the freestream velocity and the post-stall azimuthal distance travelled by the turbine blades, which can be expressed through a dimensionless pitch-rate parameter ($K_c = c/2R$). Their results showed that circulation production and vortex shedding scale more consistently with K_c than with λ, indicating that the dynamic stall process in VAWTs is mainly controlled by purely unsteady kinematic airfoil effects rather than mean operating conditions on the wind turbine alone. Importantly, they observed that for $\lambda \gtrsim 3$–3.5, the variation in relative velocity and effective angle of attack during a revolution becomes sufficiently small that no leading-edge vortex is formed. In this regime, the aerodynamic response approaches quasi-steady behaviour, and dynamic stall effects are less impactful.

However, it is important to note that all of these experimental studies were conducted at relatively low

Reynolds numbers, typically of the order of 10^4–10^5, due to wind-tunnel and PIV constraints. Extending the understanding and calibration of dynamic stall models to higher Reynolds numbers remains an essential research need, particularly for large-scale turbines such as SeaTwirl, which operate at Reynolds numbers in the range of $\mathcal{O}(10^6 - 10^7)$. Numerical studies have been conducted, attempting to predict the dynamic stall response, but these have mainly been done on airfoil level [20] only and not on full turbine scale, as has been done in previously mentioned PIV research.

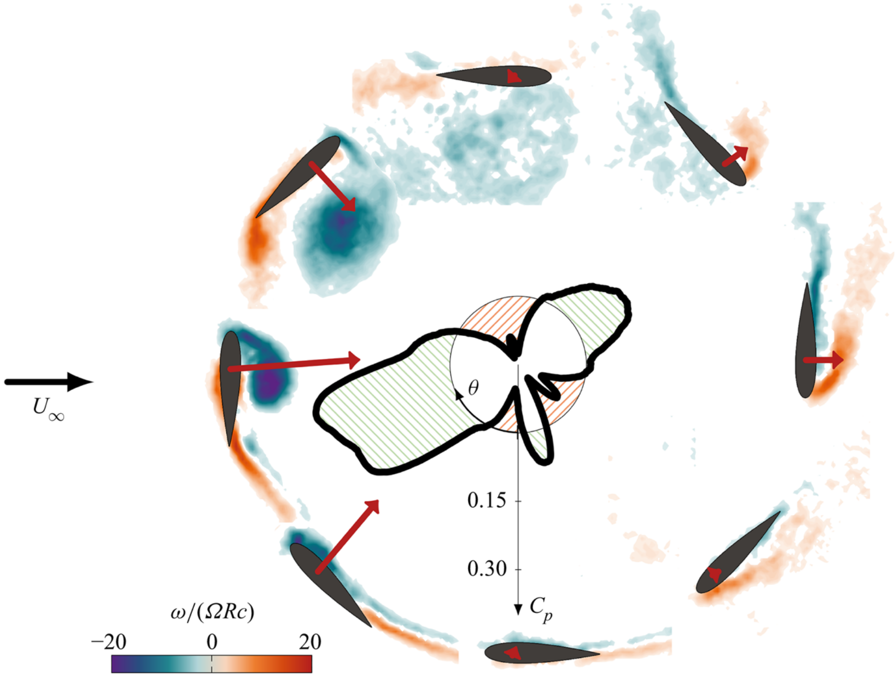

Figure 3.3: Evolution of the circulation of leading-edge separated vortex for k = 2 at 90, 108, 133 and 158, from [6]

While the physical understanding of dynamic stall in VAWTs has improved substantially, modelling it remains a major source of uncertainty in performance and loads prediction. In [50], the effect of uncertainty in dynamic stall model parameters on predicted turbine performance is quantified. Their results demonstrated that although dynamic stall models introduce noticeable variability in predicted torque and power at low TSRs, their influence near rated conditions remains within the range of experimental uncertainty. Nevertheless, the inclusion of dynamic stall modelling significantly improved the agreement between model predictions and experimental data. These findings highlight the need for accurate, yet computationally efficient, dynamic stall models for VAWTs, especially for turbines such as SeaTwirl that operate in stall-regulated regimes where blade aerodynamics directly influence power production and load control.

The results from these studies confirm that dynamic stall is an unavoidable and dominant aerodynamic feature in VAWT operation. Its effects extend beyond transient load fluctuations, influencing average power production, fatigue loading, and the overall aeroelastic behaviour of the rotor. A proper representation of dynamic stall is therefore important for the design of modern VAWTs. In the context of this thesis, understanding and accurately modelling dynamic stall is essential to predict the aerodynamic forces acting on the blades and, consequently, the performance of stall-regulated turbines.

3.3. Dynamic stall models

It can be concluded from previous sections that dynamic stall poses a significant challenge for the prediction of unsteady aerodynamic loads, as it involves highly non-linear, time-dependent flow separation and reattachment processes. To avoid the high computational cost of (fully resolved) rotor-scale simulations, a range of empirical and semi-empirical models has been developed that capture the essential physics of dynamic stall with limited computational effort. These models typically decompose the unsteady lift, drag, and moment into attached and separated contributions, and employ state-space or indicial response functions to represent the lagged development of the boundary layer and the dynamic stall vortex. The primary objectives of dynamic stall models are to predict the overshoot in lift and moment due to vortex shedding, capture the hysteresis in the aerodynamic coefficients over the pitch cycle, and maintain robustness and ease of calibration across a variety of airfoil geometries and reduced frequencies.

The historical development of dynamic stall modelling has its origins in classical unsteady aerodynamics. The first theoretical framework for unsteady lift was established by Theodorsen [51], who derived an analytical expression for the lift response of a thin airfoil undergoing harmonic oscillations in incompressible flow. While Theodorsen's model assumes small perturbations and fully attached flow, it laid the foundation for the following modern models. Thedorsen theory is also used for the verification of newly developed models.

Building upon these early concepts, empirical dynamic stall models were introduced to account for the non-linear effects of large-angle, time-dependent separation. The Beddoes-Leishman model [36] became one of the most influential formulations, combining a lagged response to changes in angle of attack with empirical rules for vortex shedding and lag effects. Many variations and simplifications have been developed based on the Beddoes-Leishman model for different applications (see Melani [19] for an extensive review), with the Risø model [7] being developed for wind turbine applications. Additionally, Øye [18] proposed a more computationally efficient approach using first-order differential equations to model the unsteady lift development, particularly suited for wind turbine applications. There are a plethora of other models and variations of models available that have been developed for different applications. The most notable for wind turbine applications are the ones mentioned above, and the ONERA [37] and Snel [52] model. All models have their advantages and disadvantages, but [39] concludes that the Øye and Risø models show themselves to be the most robust and accurate for wind turbine applications. For the scope of this thesis, these will thus be considered only.

The physical basis of dynamic stall models typically includes several key elements: a linear or quasi-linear response at low angles of attack, governed by potential flow theory (Theodorsen's approach); a delay in boundary layer response to angle-of-attack changes, often modelled using lagged state-space equations; a sharp lift overshoot associated with the formation and convection of a dynamic stall vortex; and a gradual decay of lift and moment as the vortex convects downstream and flow reattachment occurs. Modern models blend these elements with empirical calibration based on wind tunnel experimental data to achieve both accuracy and computational efficiency.[53, 36, 54, 19]

SeaTwirl has implemented both the Risø and Øye model in their aeroelastic solver. For the scope of this research, only the Risø and Øye model are included, but similar processes can be applied to other models.

3.3.1. Risø model

As mentioned before, a widely used dynamic stall model, performing well in wind turbine applications, is the Risø model [7], which is a simplification of the Beddoes-Leishman model [36], specifically applied to wind turbines. [7] presents both a state-space analysis and an indicial formulation. The state-space formulation will be presented here, as it is physically more intuitive.

The Beddoes-Leishman model aims to represent actual flow phenomena semi-empirically, with physics-based modelling. However, since the model has been developed for helicopter blades, it includes effects experienced on helicopter airfoils, but not (or rarely) in wind turbine airfoils, such as leading-edge separation and compressibility. For VAWTs, the flow Mach numbers typically remain below 0.3, justifying the incompressibility assumption. However, for large, modern HAWTs, particularly those operating at high tip-speed ratios, local Mach numbers may approach or exceed this threshold [55] [56], potentially invalidating the assumption of incompressibility. Additionally, leading-edge separation is less likely to occur in wind turbine applications due to the thicker airfoil used [45]. It has to be noted that the Beddoes-Leishman model does show good prediction for dynamic stall for wind turbine airfoils, as well as has been concluded from [54]. However, by removing the need to model these phenomena, the model can be simplified significantly, removing computational cost in aero-elastic simulations.

A flowchart of the Risø model with colour-code calculation inputs can be seen in Figure 3.4.

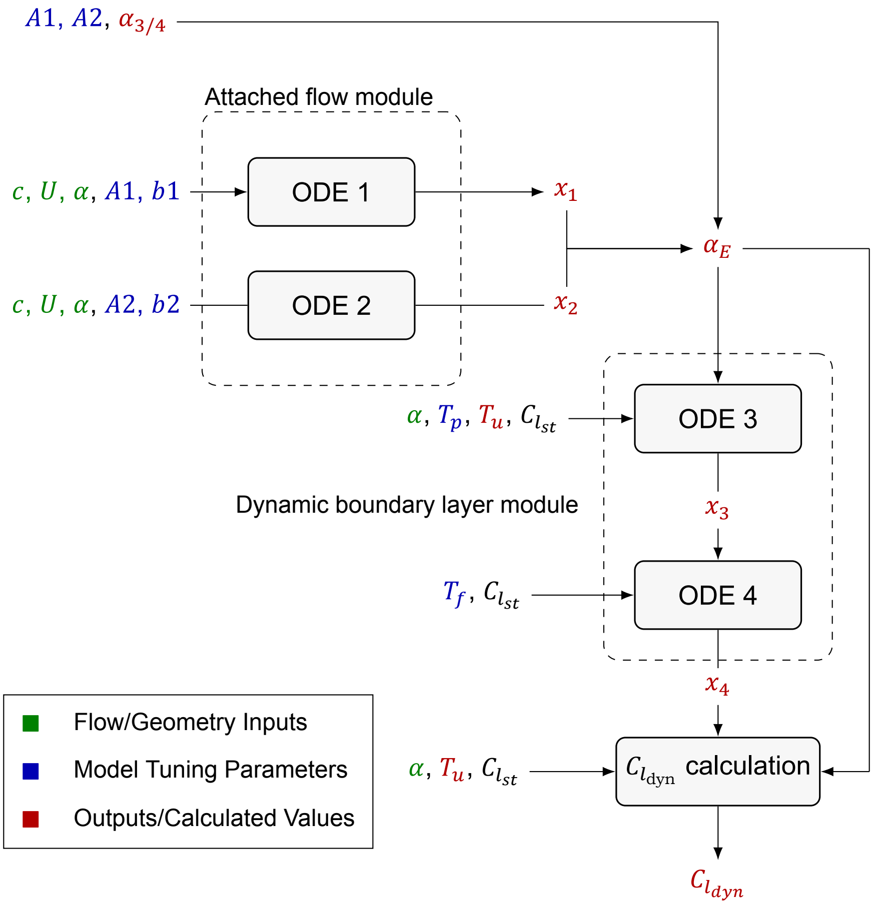

Figure 3.4: Flowchart for the Risø-BL dynamic stall model

Attached Flow

The first module of the Risø model predicts the unsteady lift on a symmetric airfoil performing harmonic pitching and/or plunging motion in attached flow. It has its origins from Theodorsen's theory [51], which assumes small amplitude and incompressible, attached flow. In this module, the effective, unsteady angle of attack that the airfoil experiences will be determined. This angle will replace the geometric angle of attack at the three-quarter point of the airfoil in quasi-steady force calculations. Equation 3.1 shows the effective angle of attack, based on two time-lag constants (A_1 and A_2), and two aerodynamic state variables (x_1 and x_2), that serve as a memory term.

$$\alpha_E = \alpha_{3/4}(1 - A_1 - A_2) + x_1(t) + x_2(t) \tag{3.1}$$

The state variables x_1 and x_2 can be determined by two ODEs, which describe the time lag in aerodynamic response. They can be seen in Equation 3.2, with $i = 1, 2$. The three-quarter chord angle of attack can be calculated from unsteady Theodorsen [51] airfoil theory. Assuming a pitching axis around the quarter-chord, the three-quarter chord angle of attack is given by Equation 3.3

$$\dot{x}_i + \frac{2U}{c}(b_i + \frac{c\dot{U}}{2U})x_i = b_i A_i \frac{2U}{c}\alpha_{3/4} \tag{3.2}$$

$$\alpha_{3/4} = \alpha_{1/4} + \frac{c}{2U}\dot{\alpha} \tag{3.3}$$

The solutions of these ODEs serve as memory terms for virtual angles of attack resulting from an effective downwash at the three-quarter point due to shed vorticity at previous timesteps. They originate from the approximation of Duhamel's integral formulation in the circulatory terms of the unsteady lift. Duhamel's integral formulation uses an indicial function $\phi(s)$, which is approximated by Equation 3.4.

$$\phi(s) = 1 - A_1 e^{-b_1 s} - A_2 e^{-b_2 s} \tag{3.4}$$

Where s is the non-dimensional time (Equation 3.5). The constants A_1, A_2, b_1, and b_2, originate from Wagner and Kussner functions (Equation 3.4), which model the response to a step change in angle of attack and inflow, respectively. By integrating the response to infinitesimally small step changes using Duhamel's integral, the airfoil response to an arbitrary angle of attack and inflow velocity variation can be determined. More information on Wagner and Kussner functions can be found in [57].

$$s = \frac{2}{c}\int_0^t U dt \tag{3.5}$$

The full derivation of Eqs. 3.1 - 3.4 can be found in the original description by Madsen [7].

Stalled flow with trailing edge separation

The next module covers the trailing edge separation, which occurs when the stall happens. The original Beddoes-Leishman dynamic stall model also includes leading-edge separation. However, this leading edge separation is not included in the Risø model as it is not expected to be a dominant effect in wind turbine applications due to the use of thicker airfoils [45] [46].

The trailing edge separation module is based on the assumption that the static lift curve can be represented by the lift on a flat plate in a potential Kirchhoff flow [58], as seen in Equation 3.6

$$C_l^{st} = C_{l,\alpha}\left(\frac{1+\sqrt{f^{st}(\alpha)}}{2}\right)^2 (\alpha - \alpha_0) \tag{3.6}$$

With $C_{l,\alpha}$, the lift slope of the lift curve in the linear attached flow regime. $f^{st}(\alpha)$ is a function that determines the chordwise separation point location. $f = 1$ for fully attached flow and $f = 0$ for fully separated flow. Other methods of estimating this separation point location, such as those presented in [59]. However, Kirchhoff's assumptions provide sufficient accuracy in the light of dynamic stall models. Assuming the static lift curve has been determined, the $C_{l,\alpha}$ and $f^{st}(\alpha)$ can thus be determined.

Next, the static lift curve can be assumed using Equation 3.7. Solving for C_l^{fs} allows one to determine the so-called fully separated lift curve. This is the lift curve that describes the static lift curve after the flow is fully separated. However, at angles of attack lower than the angle at which the flow is fully separated, this lift curve is non-physical. An example of this rebuilt static lift curve can be seen in Figure 3.5, together with the error introduced due to the approximation. The static lift curve is based on data from Glasgow University [60]

$$C_l^{st} = C_{l,\alpha}(\alpha - \alpha_0) f^{st} + C_l^{fs}(\alpha)(1 - f^{st}) \tag{3.7}$$

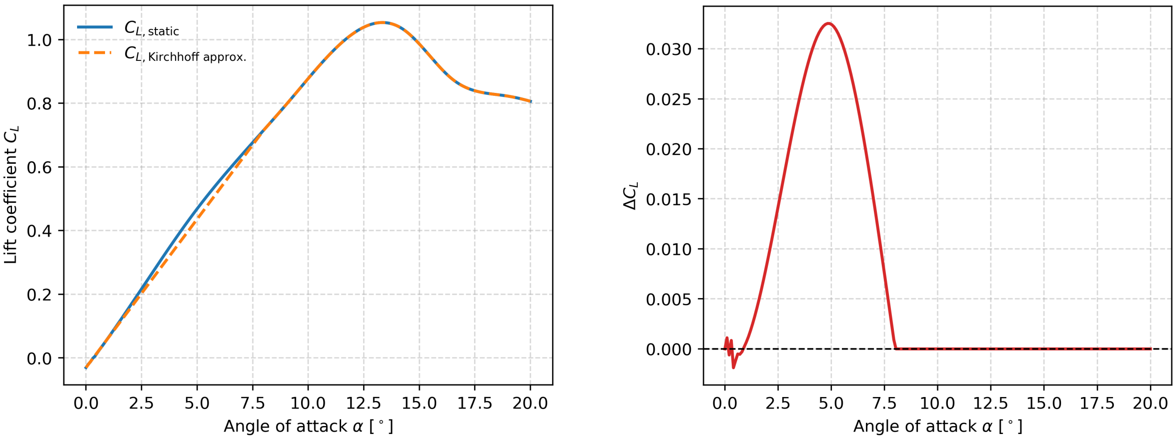

(a) Static lift curve vs Kirchhoff approximation.

(b) Error between the two curves.

Figure 3.5: Comparison of the static lift curve and its Kirchhoff approximation.

As can be seen in Figure 3.5, a small error is introduced around $\alpha = 5$, mainly due to some small non-linearity in the measured lift curve. However, this error is within the bounds of the engineering accuracy that dynamic stall models aim to achieve.

Dynamics of trailing edge separation

The static aerodynamic properties of the trailing edge separation have now been established, but similar to the attached flow regime, trailing edge separation also experiences two time-lag effects: the pressure lag and the boundary layer lag.

The pressure lag effect is assumed based on the time delay between the lift and the corresponding pressure distribution. Since a certain lift is associated with a specific pressure distribution, and this distribution in turn determines the separation point, it follows that the separation dynamics can be modelled through this delayed pressure response. The pressure lag is described as

$$\dot{x}_3 + T_p^{-1} x_3 = T_p^{-1} C_l^p(t) \tag{3.8}$$

Where $C_l^p(t)$ is the unsteady lift coefficient for attached flow given by Equation 3.9, state variable x_3 is a time-lagged lift coefficient $C_l^{p'}$ compared to the lift coefficient C_l^p for attached flow. This time-lagged lift coefficient can be used together with the attached flow coefficient to determine an equivalent quasi-steady angle of attack given by Equation 3.10. T_p is a time constant for the pressure lag.

$$C_l^p = 2\pi(\alpha_E - \alpha_0) + \pi c \dot{\alpha}/(2U) \tag{3.9}$$

$$\alpha_f = C_l^{p'}/C_{l,\alpha} + \alpha_0 \tag{3.10}$$

Based on this equivalent angle of attack, an equivalent quasi-steady separation point $f' = f^{st}(\alpha_f)$ based on Equation 3.7. The second state variable of trailing edge separation is determined by Equation 3.11.

$$\dot{x_4} + T_f^{-1} x_4 = T_f^{-1} f'(t) \tag{3.11}$$

Where T_f is a time constant for the lag in the boundary layer, state variable $x_4(t) = f''$ describes the unsteady separation point location, and can be used to determine the unsteady lift coefficient using Equation 3.12.

$$C_l^{dyn} = C_{l,\alpha}(\alpha_E - \alpha_0) f'' + C_l^{fs}(\alpha_E)(1 - f'') + \pi T_u \dot{\alpha} \tag{3.12}$$

Drag

The dynamic drag estimation model presented by Hansen [7] differs from the original Beddoes-Leishman model. Hansen describes the unsteady drag as the sum of the static drag, with a viscous and an induced term, as seen in Equation 3.13

$$C_D^{dyn} = C_D^{st}(\alpha_E) + \Delta C_D^{ind} + \Delta C_D^{f''} \tag{3.13}$$

ΔC_D^{ind} is based on the shift of the unsteady lift angle due to wake downwash. In contrast to the steady case, where no circulation is shed and the aerodynamic force is perpendicular to the geometric angle of attack, unsteady flow conditions induce circulation through the wake, causing the effective angle of attack α_E to lag behind the geometric angle α. As a result, the unsteady lift vector becomes perpendicular to α_E, and thus has a projection in the drag direction defined by α. This leads to an additional drag component referred to as induced drag. A visualistion of this process can be seen in Figure 3.6.

It is important to note that, in two-dimensional flows, induced drag is solely an unsteady phenomenon, unlike the always-present induced drag in finite-span wings. Small-angle approximations are employed as the difference between the geometric and effective angle of attack is assumed to be small. A more detailed derivation and explanation can be found in [7].

The induced drag coefficient is modelled as

$$\Delta C_D^{ind} = (\alpha - \alpha_E) C_l^{dyn} \tag{3.14}$$

where α_E and C_l^{dyn} are the effective angle of attack and dynamic lift coefficient, respectively.

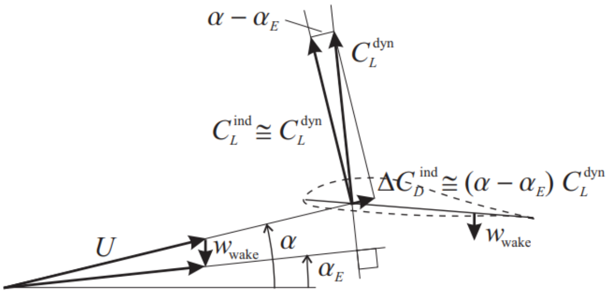

Figure 3.6: Visualisation of induced drag calculations based on dynamic lift coefficients for Risø model. Adapted from [7]

The second unsteady drag component, $\Delta C_D^{f''}$, accounts for variations in pressure drag due to the unsteady motion of the trailing edge separation point. This term originates from an analytical expression for pressure drag on a flat plate in potential Kirchhoff flow [58], where drag is expressed as

$$C_D^{\text{Kirchhoff}} = C_{l,\alpha}\alpha^2 \left(\frac{1-\sqrt{f}}{2}\right)^2 \tag{3.15}$$

However, this expression was found to yield poor agreement with experimental data except for minor separation cases, as shown by Beddoes and Leishman [10]. The Risø model, therefore, implements a modified approach, still inspired by Kirchhoff's formulation. The unsteady contribution is estimated by considering the lag between the unsteady separation point f'' and the quasi-steady separation location $f^{\text{st}}(\alpha_E)$:

$$\Delta C_D^{f''} = \left(C_D^{\text{st}}(\alpha_E) - C_{D0}\right)\left[\left(\frac{1-\sqrt{f''}}{2}\right)^2 - \left(\frac{1-\sqrt{f^{\text{st}}(\alpha_E)}}{2}\right)^2\right] \tag{3.16}$$

Here, $C_D^{\text{st}}(\alpha_E)$ is the static drag coefficient curve, and C_{D0} is the drag at zero lift. The difference $C_D^{\text{st}} - C_{D0}$ effectively replaces the $C_{l,\alpha}\alpha^2$ term in Kirchhoff's expression, isolating the pressure drag component.

Moment

Similar to the drag, the unsteady moment is defined as the steady moment at the equivalent angle of attack, with some additional terms accounting for airfoil motion and separation point location. This can be seen in Equation 3.17

$$C_M^{dyn} = C_M^{st}(\alpha_E) + \Delta C_M^{f''} - \pi c \dot{\alpha}/(4U) \tag{3.17}$$

Where $C_M^{st}(\alpha_E)$ is the steady moment coefficient at the equivalent angle of attack, $\Delta C_M^{f''}$ is the unsteady moment due to dynamic trailing edge separation, and the last term is the added mass effect, originating from the pitching motion of the airfoil.

Madsen [7] models the effect of trailing edge separation on the moment by assuming a relation between the separation point and the position of the centre of pressure. This relation can be described by a distance a^{st}, which is described by

$$a^{st} = \frac{C_M^{st} - C_{M_0}}{C_l^{st}} \tag{3.18}$$

Where C_{M_0} is the zero-lift moment coefficient, and a^{st} the distance from the quarter chord (assumed to be the aerodynamic centre of the airfoil at low angles of attack and attached flow, consistent with thin airfoil theory [61]). Since thin airfoil theory predicts the moment to be constant around the quarter chord, the change in moment can only be attributed to a lift force acting on a different centre of pressure. A visualisation of all geometry and forces acting in the process above can be seen in Figure 3.7.

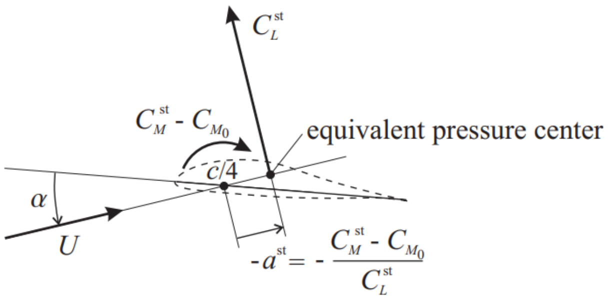

Figure 3.7: Definition of the distance a^{st} from the quarter-chord to the equivalent pressure center. From [7]

f_{st} is related to the moment arm, as can be seen in Figure 3.8, which is also a function of the angle of attack. The moment coefficient change originating from trailing edge separation is then given by Equation 3.19.

$$\Delta C_M^{f''} = C_l^{dyn}\left[a^{st}(f'') - a^{st}(f^{st}(\alpha_E))\right] \tag{3.19}$$

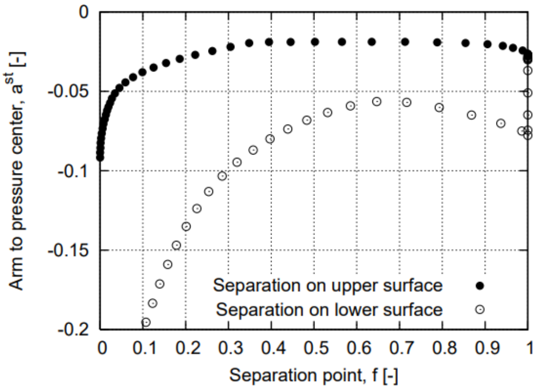

Figure 3.8: Distance of equivalent pressure centre as a function of separation factor. From [7]

Summary

To conclude, the closed set of coupled equations is presented below. These can be used, together with geometric input data from aero-elastic solvers, to determine the aerodynamic performance of a dynamic airfoil.

$$\dot{x}_1 + T_u^{-1}\left(b_1 + c\,\frac{\dot{U}}{2U^2}\right)x_1 = b_1 A_1 T_u^{-1}\alpha_{3/4} \tag{3.20}$$

$$\dot{x}_2 + T_u^{-1}\left(b_2 + c\,\frac{\dot{U}}{2U^2}\right)x_2 = b_2 A_2 T_u^{-1}\alpha_{3/4} \tag{3.21}$$

$$\dot{x}_3 + T_p^{-1}x_3 = T_p^{-1}\left(C_{l,\alpha}(\alpha_E - \alpha_0) + \pi T_u^{-1}\dot{\alpha}\right) \tag{3.22}$$

$$\dot{x}_4 + T_f^{-1}x_4 = T_f^{-1}f^{\mathrm{st}}\left(\frac{x_3}{C_{l,\alpha}} + \alpha_0\right) \tag{3.23}$$

The unsteady aerodynamic coefficients are given by:

$$C_l^{\mathrm{dyn}} = C_{l,\alpha}(\alpha_E - \alpha_0)x_4 + C_l^{\mathrm{fs}}(\alpha_E)(1 - x_4) + \pi T_u^{-1}\dot{\alpha} \tag{3.24}$$

$$\begin{aligned} C_D^{\mathrm{dyn}} &= C_D^{\mathrm{st}}(\alpha_E) + (\alpha - \alpha_E)C_l^{\mathrm{dyn}} \\ &\quad + \left(C_D^{\mathrm{st}}(\alpha_E) - C_{D_0}\right)\left(\frac{\sqrt{f^{\mathrm{st}}(\alpha_E)} - \sqrt{x_4}}{2} - \frac{f^{\mathrm{st}}(\alpha_E) - x_4}{4}\right) \end{aligned} \tag{3.25}$$

$$C_M^{\mathrm{dyn}} = C_M^{\mathrm{st}}(\alpha_E) + C_l^{\mathrm{dyn}}\left(a^{\mathrm{st}}(x_4) - a^{\mathrm{st}}(f^{\mathrm{st}}(\alpha_E))\right) - \frac{\pi}{2}T_u^{-1}\dot{\alpha} \tag{3.26}$$

Madsen [7] also presents recommended tuned model parameters based on experimental data by Jones [62] for a flat plate, and numerical data obtained by Madsen for the Risø A1-24 airfoil [63]. It is worth noting that these parameters are optimised for a specific geometry, so they should be verified and adjusted accordingly for different applications. The flat plate values are often used in commercial aero-elastic solvers, as they provide a good approximation for a wide range of wind turbine applications.

Table 3.1: Risø coefficients for attached motion according to [7]

Coefficient	Flat plate (Jones) [62]	Risø A1-24 airfoil [7]
A_1	0.165	0.294
A_2	0.335	0.331
b_1	0.0455	0.0664
b_2	0.3000	0.3266

Table 3.2: Beddoes-Leishman coefficients for time-lag constants according to [10]

Coefficient	NACA0012
T_p	1.7
T_f	3

3.3.2. Øye

The Øye [18] model is significantly simpler than the Risø model developed by Stig Øye and presented in 1991. It uses a single first-order ordinary differential equation (ODE) to predict the unsteady lift coefficient based on the time lag introduced by unsteady inflow conditions. The model can tackle dynamic stall originating from airfoil pitching and dynamic freestream conditions. Similar to the Risø model, the Øye model aims to predict the unsteady lift coefficient based on a dynamic separation factor f, which interpolates between an attached and fully separated lift curve. This separation factor is modelled as an ordinary differential equation with a time-lag constant τ. Compared to the Risø model, the Øye model only utilises one differential equation, against four in the Risø model, making it more computationally efficient. Some complex dynamics, such as vortex shedding, however, are modelled less accurately.

The original Øye paper presents the following steps to determine the dynamic lift coefficient.

1. Define attached $C_{l,\alpha}$
2. Define fully separated $C_l^{sep}(\alpha)$
3. Define f_{st}
4. Calculate f from Equation 3.27
5. Calculate dynamic lift coefficient from Equation 3.28

Øye does not specify a method to define the attached and fully separated lift curve, so that is open to implementation as desired. The same approach can be taken as has been done in the Ris ø model, by using Kirchhoff flat plate theory, as seen in Equation 3.7. This is a common approach taken in multiple solvers. However, it is also possible to determine the separation point location differently. Based on the separation point location, the Øye ODE can be solved:

$$\frac{df}{dt} = \frac{f_{st} - f}{\tau} \tag{3.27}$$

Where f is the dynamic separation point location, f_{st} is the static separation point location, according to Kirchhoff's theory, and τ is a time constant for the lag. τ is usually defined as $A \cdot c/V$, with c the chord, V the freestream flow velocity, and A between $4 - 8$. However, it is mentioned in the original paper by Øye [18] that the lift response is relatively insensitive to the time constant value.

Using the f achieved from solving the ODE, the dynamic lift coefficient can be determined using Equation 3.28.

$$C_{l_{dyn}} = C_{l,\alpha}(\alpha - \alpha_0)f + C_l^{fs}(1 - f) \tag{3.28}$$

Øye did not present an unsteady drag or moment estimation in his original paper [18]. Different commercial aeroelastic tools have varying implementations; some assume the moment and drag coefficients correspond to their static counterparts, as done by Principia [16]. Others, such as Qblade [17], utilise a similar method as the drag estimation in the Risø model (Equation 3.25), but adapted to the Øye model, as presented in Equation 3.29

$$C_{d_{dyn}} = C_d^{st} + \left(C_d^{st} - C_{d_0}^{st}\right)\left(0.5\left(\sqrt{f^{st}} - \sqrt{f}\right)\right) - 0.25(f - f^{st}) \tag{3.29}$$

Where C_d^{st} and $C_{d_0}^{st}$ are the steady drag coefficient and zero drag coefficient, respectively.

3.3.3. Tuning

Both the Risø and the Oye dynamic stall models are semi–empirical formulations. Their structure is grounded in aerodynamic theory, but they rely on a set of tunable parameters that must be calibrated to reproduce the unsteady aerodynamic response of a specific airfoil and operating regime. Historically, many of these parameters trace back to helicopter aeroelasticity, where early dynamic stall models, such as the Beddoes–Leishman model, were tuned using rotorcraft wind tunnel data [10]. When later adopted in wind turbine research, only minor modifications have been made to account for different operating regimes and airfoils [5].

A central challenge in tuning is defining the optimisation target. Depending on the intended use of the model, the objective function may prioritise peak lift predictions, phase lag in the hysteresis loop, aerodynamic damping and flutter stability, or accurate cycle–averaged loads relevant for fatigue design [64]. For VAWTs in particular, the cyclic nature of aerodynamic loading makes accurate prediction of both the load excursions and their phasing crucial. This implies that calibration requires a sufficiently rich dataset spanning relevant reduced frequencies, Reynolds numbers, and angles of attack [19]. Overfitting to a narrow subset of cases can lead to non-physical behaviour when the model is subsequently extrapolated. Based on a large dataset, not only can general parameters be determined, but the parameters can also be estimated based on flow and airfoil conditions. An example for this is the shape-based optimisation of parameters done by Wala et al. [65]

Multiple strategies exist for tuning. A purely numerical optimisation, as followed by Mert[53] and Faber [39], can deliver significant error reduction; however, such approaches risk obscuring the physical meaning of the constants and producing parameter sets that compensate for underlying modelling deficiencies. A risk that is also highlighted in [19]. A more physics-informed strategy constrains parameters such that they continue to reflect aerodynamic time scales and separation dynamics as originally intended by Leishman and Beddoes [36]. This philosophy is evident in recent work by Melani et al. [19], who calibrate the Beddoes-Leishman model while preserving the physical role of lag coefficients and separation point evolution. Beyond experiments, high-fidelity CFD has increasingly been used as an additional data source for tuning, demonstrating that the achievable agreement with both CFD and experiments is typically within acceptable engineering accuracy [66, 67]. Experimental campaigns remain the cornerstone of high-quality calibration, with a wide range of studies demonstrating improved predictive capability after targeted tuning [54, 53, 39, 19]. These efforts show that carefully constrained tuning can substantially enhance the fidelity of dynamic stall predictions while maintaining a clear connection to the governing aerodynamics.

Tuning of the models does not have to be limited to the determination of typical model parameters. Different implementations can also improve accuracy. For example, in the determination of the separation point location, Risø and Øye both use the Kirchhoff stall model; however, this estimation can be improved upon [59]. This can be seen in different commercial implementations of the Øye and Beddoes–Leishman-type formulations in aero-elastic solvers [16, 17, 68], where each solver estimates these parameters in their own, optimised and verified way.

In summary, tuning serves as a bridge between generalised dynamic stall theory and the specific flow physics of the application of interest. The most robust approaches avoid overfitting by analysing diverse datasets, explicitly defined objectives, and physically interpretable parameters. As shown across both experimental and CFD-assisted studies [64, 53, 66], this balance enables dynamic stall models such as Risø and Øye to remain computationally efficient while achieving the accuracy required for reliable performance and load predictions in modern wind turbine design.

3.3.4. Accuracy and limitations

These dynamic stall models allow for a more accurate aerodynamic force prediction compared to static lift curves only. However, there are some inherent limitations apparent. These limitations originate from the nature of dynamic stall and the dynamic stall model assumptions.

Dynamic stall, just like static stall, is a highly unsteady phenomenon, as mentioned in section 3.1. This means that real-life flows that experience dynamic stall will never (or very rarely) experience exactly the same behaviour again. In order to analyse these flows, averages should thus be used over multiple iterations. This adds some uncertainty to the analysis. Similarly, dynamic stall models only predict these ”steady-state” averaged results. There is thus an inherent physical discrepancy between dynamic stall models and the physical phenomenon.

Another limitation of dynamic stall is that they are semi-empirical models. This implies that they rely on calibration procedures to ensure sufficient accuracy of the model. The original Bedoes-Leishman model was tuned with helicopter blade data [36], and many studies have been performed to tune/adapt these models for HAWTs [7, 69, 39, 53, 19, 5]. However, for VAWT applications, fewer research and tuning efforts have been done. This increases the uncertainty of these models for VAWT(-like) applications. Faber [39] also showed that tuning of the models for certain flow characteristics might reduce the accuracy in other flow regimes. Finally, the tuning method also influences the uncertainty and predictive ability of dynamic stall models, as highlighted by Melani [19] for the Bedoes-Leishman model.

More specifically, the Risø [7] model has been developed as a simpler version of the Bedoes-Leishman [36] model, targeted towards wind turbines. However, assumptions have been made regarding compressibility and vortex shedding. It has been assumed that compressibility effects are negligible, which can be justified for VAWTs. However, the assumption that no leading-edge vortices will appear might not hold for VAWT aerodynamics, as the angle of attack variations experienced by VAWTs largely exceed those experienced by HAWTs. [33, 7]

Lastly, the Risø dynamic stall model adds unsteady effects to the static lift curve to determine the dynamic properties of airfoils in pitching motion. It is thus crucial to have an accurate determination of the static performance of an airfoil, as the results of the dynamic stall model would otherwise be inherently skewed. [10]

4

Numerical analysis

Computational Fluid Dynamics (CFD) has been commonly used throughout the history of aerospace design to predict the performance of airfoils and other lifting structures. CFD has already been widely used to predict unsteady aerodynamics, including the prediction of dynamic stall [20]. However, the link to the tuning of dynamic stall models has been researched less intensely. Huang and Hand have shown the potential of CFD to accompany wind tunnel tests to tune dynamic stall models [66, 20]. In this chapter, the approach taken to model an accurate dynamic numerical simulation will be presented. All simulations were performed using OpenFOAM [70], an open-source CFD software. The simulations were performed on Delft University's supercomputer, DelftBlue [71].

Firstly, the turbulence modelling methodology adopted in the present analysis will be discussed in section 4.1. A suitable approach should be taken into account to balance computational efficiency with accuracy. As discussed in subsection 3.3.3, for adequate tuning of dynamic stall models, a sufficiently large database should be constructed with a wide variety of run cases. This can only be achieved in case a computationally efficient analysis is performed. Similar to the turbulence modelling choice, it is also critical to determine a suitable numerical grid that strikes a balance between computational efficiency and accuracy. A grid convergence study is performed to assess the minimal grid spacing to achieve suitable results in section 4.2.

Finally, the CFD model is validated against experimental data to build confidence in the model. This is performed for both static and dynamic cases in section 4.3. Since the goal is to model dynamic stall, a database should be found that includes both static airfoil data, as well as dynamic, pitching motion data. For the NACA0018 airfoil analysed, the amount of options are limited. However, Glasgow University [60] conducted an experimental campaign, specifically designed to analyse dynamic stall for different airfoils.

4.1. Turbulence modelling

The flow around a vertical-axis wind turbine is inherently unsteady and dominated by strong flow separation at lower angles of attack, as discussed in chapter 2 and chapter 3. However, given the relatively low flow velocities involved, the inflow Mach number remains well below the compressibility threshold, and the flow can therefore be considered incompressible. The governing equations are thus derived from the incompressible and unsteady regime, using the Navier–Stokes (NS) equations, which describe the conservation of mass and momentum for a Newtonian fluid:

$$\nabla \cdot \mathbf{U} = 0 \tag{4.1}$$

$$\frac{\partial \mathbf{U}}{\partial t} + (\mathbf{U} \cdot \nabla)\mathbf{U} = -\frac{1}{\rho}\nabla p + \nu \nabla^2 \mathbf{U} \tag{4.2}$$

Where $\mathbf{U}$ denotes the velocity field, p the pressure, ρ the density, and ν the kinematic viscosity.

To model turbulent flows efficiently, the instantaneous quantities in Equation 4.2 are decomposed into mean and fluctuating components using the Reynolds decomposition:

$$\mathbf{U} = \overline{\mathbf{U}} + \mathbf{u}', \qquad p = \overline{p} + p' \tag{4.3}$$

Where overbars denote ensemble-averaged quantities and primes denote turbulent fluctuations. Substituting these expressions into the NS equations and averaging yields the Reynolds-Averaged Navier–Stokes (RANS) equations. These introduce additional terms representing the Reynolds stresses, which must be modelled to close the system.

For unsteady flows such as those around a VAWT, a temporal resolution of the RANS equations can be employed, leading to the unsteady RANS (URANS) formulation. URANS retains the ensemble-averaged turbulence modelling framework but allows the resolution of large-scale, time-dependent features, an essential capability for capturing the cyclic aerodynamic behaviour of VAWTs. While URANS models provide an efficient tool to resolve time-dependent simulations, major limitations still exist, as discussed in [72]. Hybrid models, such as wall-modelled large-eddy simulations or detached eddy simulations [73], provide a way to overcome these limitations.

4.1.1. The $k - \omega SST$ Model

To close the RANS equations, the two-equation k–ω Shear Stress Transport (SST) model developed by Menter [74, 75] is adopted. This model blends the robustness of the Wilcox k–ω model in the near-wall region with the free-stream independence of the k–ε model in the outer flow. It has proven effective in predicting flow separation under adverse pressure gradients, making it well-suited for aerodynamic applications with strong unsteadiness and separation, such as those encountered in VAWTs. The simulation is run in OpenFOAM [70], which utilises the 2003 model [75]. The choice for the $k-\omega SST$ model was made for several reasons. First of all, it is a widely used model, allowing for many references on the use of it. Additionally, the blend between the $k - \omega$ and $k - \varepsilon$ model provides a stable model for external aerodynamics that provides suitable results and separation prediction for unsteady flows and dynamic stall analysis.

The transport equations for the turbulent kinetic energy k and the specific dissipation rate ω are:

$$\frac{\partial(\rho k)}{\partial t} + \frac{\partial(\rho U_j k)}{\partial x_j} = P_k - \beta^* \rho k \omega + \frac{\partial}{\partial x_j}\left[(\mu + \sigma_k \mu_t)\frac{\partial k}{\partial x_j}\right] \tag{4.4}$$

$$\frac{\partial(\rho \omega)}{\partial t} + \frac{\partial(\rho U_j \omega)}{\partial x_j} = \alpha \frac{\omega}{k} P_k - \beta \rho \omega^2 + \frac{\partial}{\partial x_j}\left[(\mu + \sigma_\omega \mu_t)\frac{\partial \omega}{\partial x_j}\right] + 2(1 - F_1)\rho \sigma_{\omega 2} \frac{1}{\omega}\frac{\partial k}{\partial x_j}\frac{\partial \omega}{\partial x_j} \tag{4.5}$$

where P_k denotes the production of turbulent kinetic energy, μ_t the turbulent eddy viscosity, and F_1 the blending function governing the transition between the k–ω and k–ε regions. The turbulent viscosity is defined as:

$$\mu_t = \frac{\rho a_1 k}{\max(a_1 \omega, S F_2)} \tag{4.6}$$

Where S is the strain-rate magnitude and F_2 is a secondary blending function.

4.1.2. Boundary conditions

To ensure physically realistic and numerically stable solutions, appropriate boundary conditions must be prescribed at all domain boundaries. The inflow turbulence quantities can be defined in terms of the turbulence intensity I and turbulence length scale L, which together determine the turbulent kinetic energy k and the specific dissipation rate ω as follows:

$$k = \frac{3}{2}(IU)^2 \tag{4.7}$$

$$\omega = \frac{k^{1/2}}{C_\mu^{1/4} L} \tag{4.8}$$

where U is the mean velocity magnitude and C_μ is an empirical constant ($C_\mu = 0.09$). The turbulence intensity represents the ratio of the root-mean-square of velocity fluctuations to the mean velocity, while the length scale characterises the size of the largest energy-containing eddies. Both parameters strongly influence the onset and extent of flow separation and thus must be chosen carefully.

Based on turbulence intensity measurements from the Handley Page wind tunnel at the University of Glasgow [8], shown in Figure 4.1, a turbulence intensity of $I = 1\%$ was adopted. A turbulence length scale of $L = 0.0055c$ was adopted. This value was chosen such that the static lift curve closely matches the experimental results in the linear regime. At the airfoil wall, the boundary conditions for the turbulence quantities are specified as $k_{wall} = 0$ and

$$\omega_{wall} = 10\frac{6\nu}{\beta_1(\Delta d_1)^2} \tag{4.9}$$

as defined by [76]. In OpenFOAM, these relationships are automatically imposed through the default wall-function treatment for k–ω-based turbulence models. These wall models switch off for fully resolved boundary layers ($y^+ < 1$) in the OpenFOAM implementation.

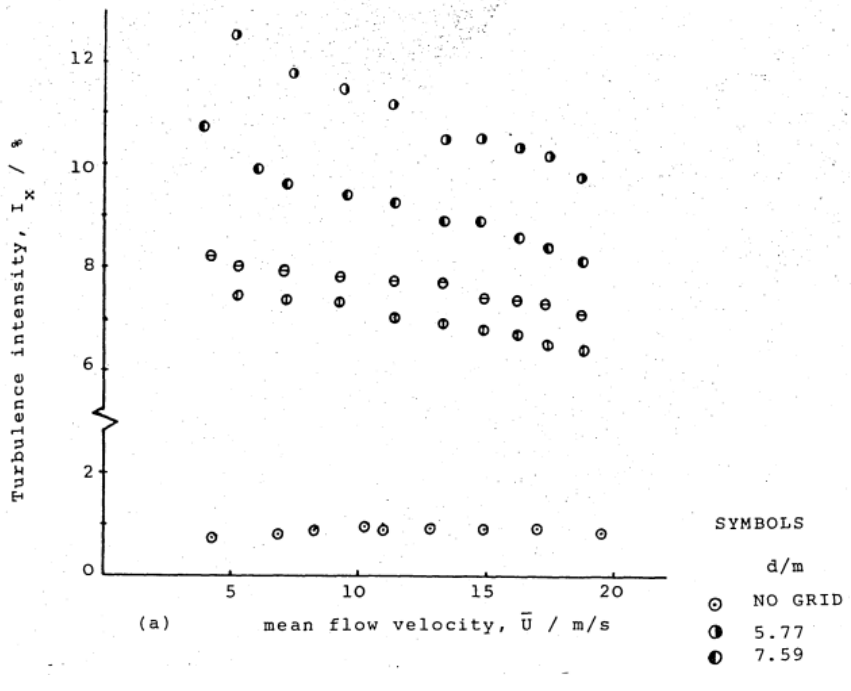

Figure 4.1: Turbulence intensity measured in Glasgow University Handley-Page wind tunnel, including values with turbulence-generating grids. From [8].

In addition to the inflow conditions, the remaining boundary conditions are defined as follows. At the inlet, a uniform velocity U_∞ is prescribed, representing the free-stream velocity, while a zero-gradient condition is applied for pressure. The turbulence quantities k and ω are fixed according to Equations (4.7)–(4.8), ensuring that the specified inflow turbulence characteristics are achieved. At the outlet, a zero-gradient condition is applied to the velocity to allow the flow to exit the domain naturally. The static pressure is fixed to zero gauge pressure ($p = 0$) to set the reference pressure level for the entire flow field. The turbulence quantities are also treated with zero-gradient conditions, allowing turbulent structures to convect freely out of the domain.

In OpenFOAM [70], the inlet and outlet conditions are automatically detected using the freestream boundary types. These automatically switch between the inflow and outflow boundary conditions depending on the local flow direction. This prevents unphysical reflections and allows a smooth entering and exiting of the flow in the domain.

The airfoil surface is modelled as a no-slip wall, enforcing $\mathbf{U} = 0$ at the surface. A zero-gradient condition for pressure ensures proper pressure recovery near the wall. This setup allows for an accurate representation of the boundary layer and separation phenomena, which are essential for capturing dynamic stall behaviour. The front and back boundaries of the domain are assigned empty conditions using OpenFOAM's empty boundary types. These allow for a 2D analysis, to keep computational requirements low. The analysis will be performed using a non-dimensional incompressible simulation. This means that the velocity and chord are fixed to be the unit velocity and chord. The Reynolds number will be set by adapting the dynamic viscosity constant ν.

A summary of the boundary conditions used in the simulations is given in Table 4.1. All conditions were verified through sensitivity tests and mesh refinement studies (see section 4.2) to ensure their influence on the aerodynamic coefficients remained negligible.

Table 4.1: Summary of boundary conditions used in the OpenFOAM simulations.

Boundary	**Velocity $\mathbf{U}$**	**Pressure p**	k	ω
Inlet	fixedValue (U_∞)	zeroGradient	fixedValue (Eq.4.7)	fixedValue (Eq.4.8)
Outlet	zeroGradient	fixedValue ($p = 0$)	zeroGradient	zeroGradient
Airfoil surface	fixedValue ($\mathbf{U} = 0$)	zeroGradient	fixedValue ($k = 0$)	wallFunction (ω_{wall})
Far-field	empty	empty	empty	empty

Overall, these boundary conditions were designed to closely replicate the experimental wind tunnel setup at Glasgow University while ensuring numerical robustness. They provide a physically consistent flow environment necessary for accurately resolving the onset and progression of dynamic stall, forming the foundation for the subsequent model validation and dynamic stall tuning.

4.2. Numerical discretisation methods

4.2.1. Grid geometry

The grid topology adopted in this work is an O-grid. This choice is mainly motivated by the need for robustness across a wide range of inflow angles of attack, which is essential for both dynamic stall and VAWT-related analyses, as discussed in chapter 2 and chapter 3. Because of its circumferential, radially expanding structure, an O-grid preserves near-orthogonality to the airfoil surface for essentially all inflow directions. This is one of the main advantages of using the O-grid topology. During dynamic stall, the instantaneous angle of attack can vary by tens of degrees [44], and mesh topologies that depend on alignment with a single nominal inflow direction can introduce direction-dependent numerical errors. The O-grid reduces this sensitivity and maintains consistent resolution of the leading-edge, trailing-edge, and separated-flow regions across the full angle of attack range. Additionally, an O-grid provides precise control of the wall-normal spacing, which is required for boundary-layer-resolving RANS simulations. The first-cell height can be set to enforce $y^+ \approx 1$ while maintaining low skewness in the viscous sublayer. The radial structure of the grid also aligns reasonably well with the convection of dynamic-stall vortices, helping to limit artificial diffusion as these structures move into the wake.

These advantages, however, come with important drawbacks. The most significant is the geometric coupling between inflow and outflow areas: enlarging the far-wake domain to minimise reflections or premature dissipation of shed vortices increases the inflow region by the same amount. This adds computational cost, particularly for URANS simulations where long physical-time integrations are required.

A balance must therefore be found between adequate wake resolution and acceptable computational cost. A second drawback is the rapid growth of cell size away from the airfoil. The further you get away from the centre of the O-grid, the larger the spacing will be between the cell boundaries originating from the centre of the O-grid. This introduces additional numerical diffusion. While this is acceptable for RANS, the far-field dissipation can still influence the flow results, especially in unsteady cases. The grid geometry is presented in Figure 4.2.

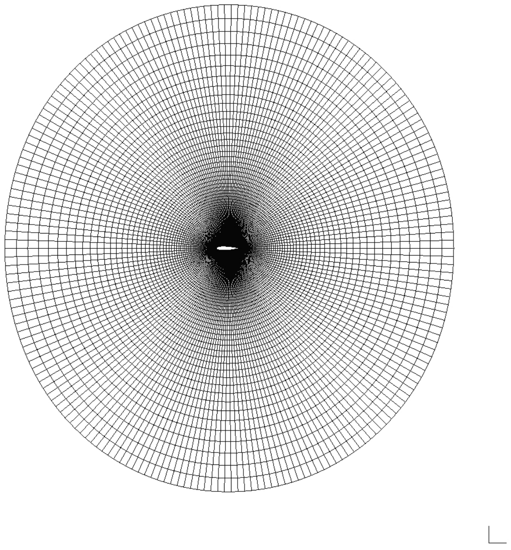

Figure 4.2: Mesh for NACA0018 airfoil at $Re = 1.5\text{e}6$

Figure 4.2 shows that the cells are strongly concentrated near the airfoil surface, which is mainly caused by the requirement of the fully resolved laminar boundary layer requirement of $y^+ \leq 1$. Since the boundary layer is thinner at higher Reynolds numbers, this requires very thin cells wrapped around the airfoil.

4.2.2. Grid convergence

The accuracy of any RANS simulation strongly depends on a mesh that balances geometric resolution with computational cost. For two-dimensional airfoil flows, three aspects of the grid dominate this balance: the discretisation along the airfoil surface, the normal spacing away from the wall, and the outer-domain extent. Each governs a distinct physical mechanism: pressure recovery and stall onset are particularly sensitive to tangential clustering, the boundary-layer growth and separation behaviour depend on the wall-normal resolution, and the far-field size determines how effectively the outer boundary decouples from the near-field disturbances. Reducing any of these parameters without care leads either to unnecessary computational expense or to a systematic distortion of the aerodynamic coefficients. A mesh-convergence study is therefore required. [77]

The present analysis focuses on the influence of the tangential surface resolution, since this parameter showed the strongest influence on both lift and drag over the angle-of-attack range relevant for the dynamic-stall simulations. Four meshes were constructed with $N = \{100, 200, 300, 600\}$ points distributed along the airfoil surface, while the normal spacing and far-field size were kept fixed. The resulting lift and drag coefficients for three representative angles of attack are displayed in Figure 4.3. Visually, the grids with more than 200 airfoil points provide a similar level of accuracy, within some engineering accuracy.

To assess the discretisation uncertainty more systematically, the Grid Convergence Index (GCI) in the sense of Roache [78] was employed. The GCI provides two complementary pieces of information: an estimate of the asymptotic convergence rate and a bound on the numerical error relative to the finest mesh. For three successively refined grids with characteristic spacings $h_1 < h_2 < h_3$, the GCI between two grids is defined as in Equation 4.10. The three finest grids are analysed, which correspond to 200, 300, and 600 points along the airfoil surface.

$$\mathrm{GCI}_{21} = F_s \frac{|\phi_1 - \phi_2|}{\phi_1\,(r^p - 1)}, \qquad r = \frac{h_2}{h_1}, \qquad h = (1/N \sum_{i=1}^{N} \Delta V_i)^{1/3} \tag{4.10}$$

where ϕ_i denotes the aerodynamic coefficient on grid i, p is the observed order of accuracy identified through a standard Richardson extrapolation, and F_s is a safety factor conventionally taken as $F_s = 1.25$. While the GCI cannot replace rigorous verification, it offers a transparent measure of how rapidly the solution approaches its grid-independent limit.

The computed GCI values and associated discretisation errors for all considered angles of attack are summarised in Table 4.2. Several trends emerge. The lift coefficient exhibits comparatively fast convergence: for $\alpha = 5°$ the finest-grid estimate differs by less than 0.04% from its Richardson extrapolation, and similar behaviour is observed at $15°$. Drag converges more slowly; the coarse-to-medium GCI$_{32}$ values are appreciably larger. Nonetheless, they remain modest across all cases. Interestingly, the behaviour of the lift and drag is reversed for $\alpha = 10°$. The drag shows better convergence compared to the lift.

The combined evidence from the raw coefficient trends in Figure 4.3 and the quantitative GCI analysis suggests that the $N = 300$ grid delivers aerodynamic loads for all attached-flow angles of attack that should be within the desired accuracy. However, since the expected run time of the simulations is long, the $N = 200$ grid is preferred. The estimated grid discretisation error remains fairly limited, but the gain in computational speed is noticeable.

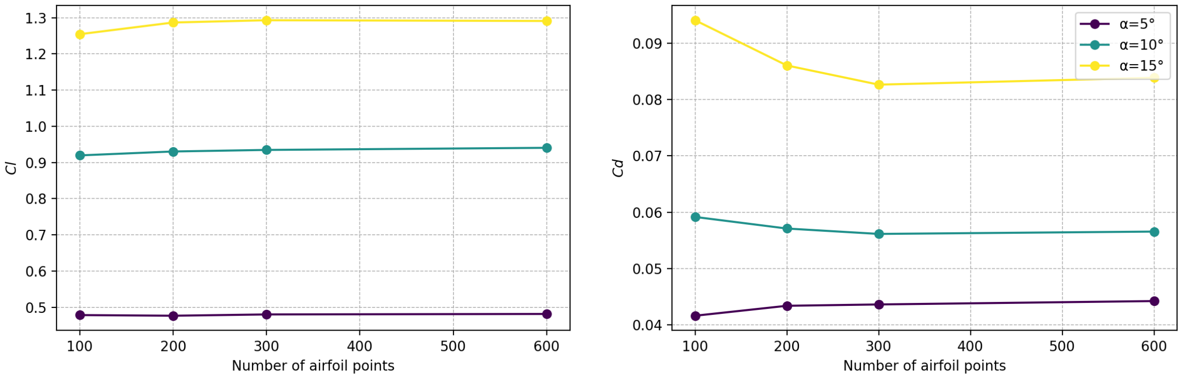

(a) C_l convergence across all angles of attack. **(b)** C_d convergence across all angles of attack.

Figure 4.3: Mesh convergence behaviour for all simulated angles of attack for (a) lift coefficient C_l and (b) drag coefficient C_d.

Table 4.2: Grid metrics, grid convergence indices, and discretisation errors for all angles of attack and coefficients.

α [°]	Coeff.	N_1	N_2	N_3	GCI [%]		Discretisation error ϵ [%]		
					GCI_{21}	GCI_{32}	ϵ_{h_1}	ϵ_{h_2}	ϵ_{h_3}
5	Cl	600	300	200	0.0438	0.3899	0.0350	0.3110	1.0538
	Cd	600	300	200	5.1577	3.9338	3.9626	5.2670	5.7811
10	Cl	600	300	200	1.8474	2.6409	1.4564	2.0690	2.5177
	Cd	600	300	200	0.3817	2.1653	0.3044	1.0350	0.6486
15	Cl	600	300	200	0.0460	0.3892	0.0368	0.1994	0.2907
	Cd	600	300	200	0.4834	3.7048	0.3853	1.8287	2.2113

4.2.3. Discretisation schemes

URANS cannot fully resolve small-scale turbulence, but rather computes the mean flow field and models the effects of turbulence. This introduces a less finely resolved flow field. Additionally, the grid can also introduce a diffusivity contribution through skewness, non-orthogonality, and interpolation errors. To respond to this, the numerical discretisation was chosen to limit the amount of diffusion added to the simulation. This was achieved by implementing second-order discretisation schemes.

The time discretisation was chosen to be the Crank-Nicolson time scheme as implemented in OpenFOAM [79]. It is a second-order, implicit scheme in time. The OpenFOAM implementation of the schemes allows blending between the Crank-Nicolson time scheme and the first-order implicit Euler time scheme. A blending factor of 0.9 is selected, which provides stability. The time step is adapted dynamically to maintain a maximum Courant number of 0.5. A Courant-Friedrichs-Lewy (CFL) number of 0.5 will allow for an accurate and stable solution in combination with the Crank-Nicolson time scheme. Implicit timestepping methods will allow for larger timesteps than a CFL of 1, and still be stable. However, to resolve the dynamic effects of dynamic stall, a fine enough time step is needed. By ensuring the CFL is lower than unitiy at all times, the resolution will not be time-step limited.

The spatial schemes were set up in a similar way. Spatial schemes ”rely heavily on interpolation schemes to transform cell-based quantities to cell faces, in combination with Gauss’s Theorem to convert volume integrals to surface integrals”, according to [80]. The main aim was to have an accurate solution with as little diffusion as possible. There are four spatial schemes to be defined: gradient schemes, divergence schemes, Laplacian schemes, and surface-normal gradient schemes. The gradient is discretised using Gauss’s theorem, with a cell-based linear interpolation scheme. The divergence schemes used for all flow quantities are the second-order, unbounded Gauss linear upwind. The OpenFOAM implementation is based on Warming and Beam [81]. The Laplacian is discretised in the same way as the gradient, Gauss Linear. It also requires a non-orthogonal correction. The surface-normal scheme employed is the corrected surface-normal scheme implemented in OpenFOAM. This scheme is slower than the other options. However, a dynamic mesh changes cell geometry and/or introduces face misalignment. The corrected surface-normal scheme provides suitable accuracy for these cases. Lastly, OpenFOAM requires a method to calculate the distance from a wall, needed for the $k - \omega SST$ model. The calculation method employed is meshWave. A summary of all numerical interpolation and Finite Volume schemes can be found in Table 4.3, and all control settings without a formal order in Table 4.4.

Table 4.3: Temporal and spatial discretisation schemes used in the URANS simulations

Category	Scheme	Order
Time discretisation	Crank-Nicolson 0.9	2nd (blended with 1st)
Gradient	Gauss linear, cell-centred interpolation	2nd
Divergence	Gauss linearUpwind	2nd
Laplacian	Gauss linear with non-orthogonal correction	2nd
Surface-normal gradient	Corrected surface-normal scheme	2nd

Table 4.4: Algorithms required by the solver that do not have a formal discretisation order.

Category	Algorithm
Time-step control	Adaptive time step, CFL = 0.5
Wall-distance calculation	`meshWave` algorithm
Mesh motion / dynamic mesh	Laplace-based mesh deformation
Non-orthogonal correction	Explicit correction loop

4.2.4. Linear solvers and algorithmic settings

To complement the numerical discretisation described previously, the linear solver setup must ensure stable convergence of the URANS equations at every time step. Since the simulations involve strong unsteadiness and a dynamically deforming mesh, the solver configuration is chosen to provide robustness without introducing unnecessary damping of the flow field.

The pressure equation is solved using the geometric–algebraic multigrid (GAMG) solver. Multigrid methods are well-suited for large finite-volume systems because they reduce both high- and low-frequency errors efficiently through grid coarsening. The smoother selected is DIC, which generally converges faster than Gauss–Seidel, and is widely used [82]. A strict absolute tolerance of 10^{-8} is imposed, while the relative tolerance is set to 0.01 so that intermediate solves do not iterate more than necessary. For the final pressure correction, the same solver configuration is used, but with a fixed relative tolerance of zero to fully converge the pressure field before updating the time step. A separate pressure-correction solve (pcorr) is also included to stabilise the flux update inside the PIMPLE loop. The velocity and turbulence equations (U, k, ω) are solved using the smoothSolver with a DILU smoother. DILU is more robust than symmetric Gauss–Seidel for dynamically deforming meshes, and it handles cross-coupling between turbulent transport terms well. A tolerance of 10^{-7} and a relative tolerance of 0.01 are applied for these fields. As with the pressure equation, final iterations for each field are solved with a stricter tolerance and relTol $= 0$ to ensure a fully converged solution at the end of each PIMPLE cycle. These settings provide stability without artificially overdamping the turbulence fields, which is important for resolving the onset and recovery of dynamic stall.

Coupling between pressure and velocity is handled by the PIMPLE algorithm. [83] A flowchart can be seen in Figure 4.4. Five outer correctors and three inner correctors are employed, which is significantly more than the OpenFOAM defaults. This is intentional: the combination of dynamic mesh motion, rapid variations in angle of attack, and the stiffness introduced by the k–ω SST model requires a stronger coupling strategy to avoid divergence during the most unsteady phases of the cycle. One non-orthogonal correction is included, consistent with the mesh quality and the Laplacian settings described previously. The momentum predictor is activated, providing a better initial estimate for the velocity field at each time step. Moderate under-relaxation is applied to improve numerical stability. The pressure is relaxed by 0.5, velocity by 0.7, and turbulence quantities by 0.5–0.7, depending on the variable. Lower relaxation improves robustness, but excessively low values can mask instabilities that should physically appear in the solution. The selected relaxation levels were found to provide stable convergence across all tested meshes and operating conditions. A summary of the solver configuration is provided in Table 4.5.

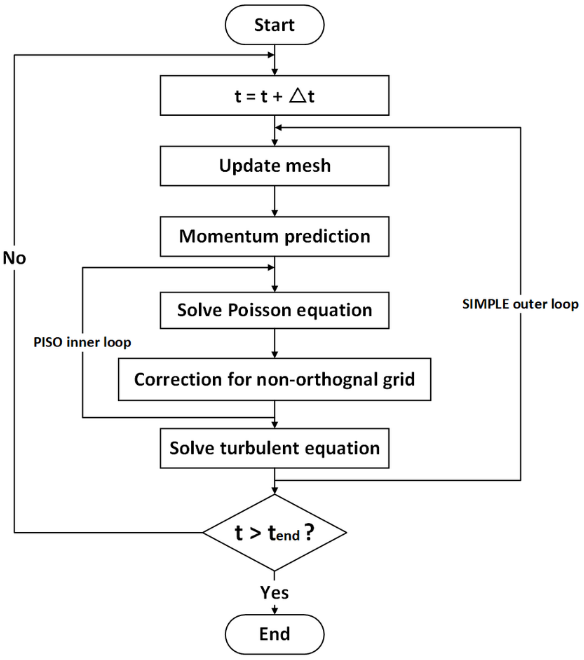

Figure 4.4: Flowchart of the PIMPLE algorithm, adapted from [9]

Table 4.5: Linear solvers and algorithmic settings used in the URANS simulations.

Quantity	Solver / Smoother	Tolerances
Pressure p	GAMG (DIC smoother)	tol $= 10^{-8}$, relTol $= 0.01$
Velocity U	smoothSolver (DILU)	tol $= 10^{-7}$, relTol $= 0.01$
k, ω, $\tilde{\nu}$	smoothSolver (DILU)	tol $= 10^{-7}$, relTol $= 0.01$
Final pressure/fields	same as above	relTol $= 0$
PIMPLE loop	5 outer, 3 inner, 1 non-orthogonal corrector	momentum predictor on

4.3. Validation

4.3.1. Validation data

For the validation of the numerical simulations, experimental data from the University of Glasgow dynamic stall database were used. [2] The database provides both static and dynamic measurements of aerodynamic coefficients for a range of airfoils under controlled conditions. In this study, the NACA0018 airfoil at a chord-based Reynolds number of approximately $1.5e6$ was analysed. In chapter 3, it was concluded that the static lift curve has a strong influence on the dynamic stall response of the airfoil; therefore, it is important to have the static and dynamic experiments performed in the same wind tunnel to reduce the uncertainties originating from wind tunnel effects.

Figure 4.6 presents the static lift curve obtained from the experimental dataset. The measurements were performed in the Handley-Page wind tunnel, and the data were obtained using pressure transducers distributed along the airfoil surface. The locations of the pressure transducers on the surface of the NACA0018 airfoil are presented in Figure 4.5. The data points represent time series of the normal and tangential force components, converted into lift and drag coefficients using standard definitions. A spline fit is performed on the time-averaged values at each angle of attack.

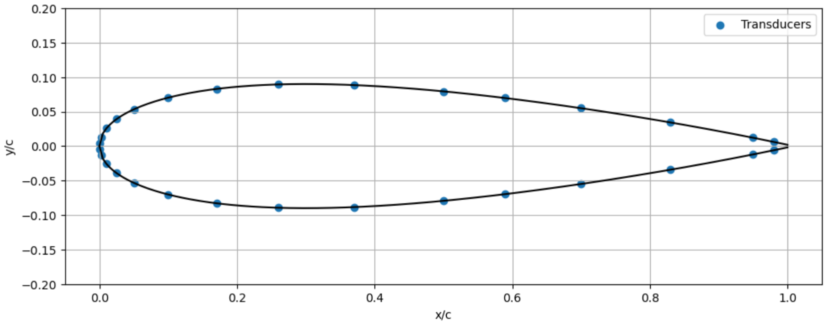

Figure 4.5: Pressure transducer locations on NACA0018 airfoil

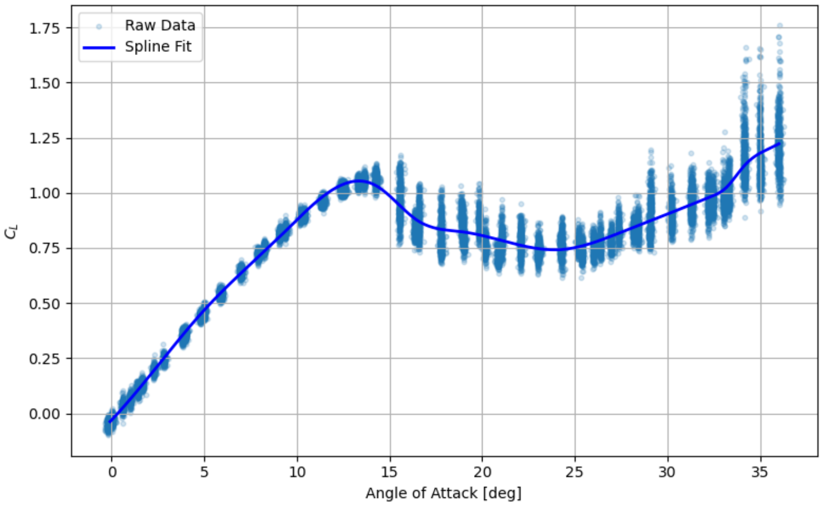

Figure 4.6: Static lift curve of the NACA0018 airfoil from the Glasgow University dataset at $Re = 1.5 \times 10^6$ [2]

According to Figure 4.6, the lift coefficient increases approximately linearly with angle of attack up to about $\alpha = 12.5°$, after which the flow undergoes a transition to stall. Beyond this point, large variations in the measured lift coefficients are observed, primarily due to the unsteady, separated flow in the post-stall regime. Such variations are typical for separated flow, as it is dominated by vortex shedding and alternating periods of attached and detached flow.

In addition to inherent flow unsteadiness, other sources of experimental deviations can be identified. These include wind-tunnel blockage and wall interference effects, particularly significant for thick airfoils like the NACA0018 when tested at high angles of attack [84, 85]. Furthermore, small deviations in angle-of-attack calibration and the finite resolution of the pressure transducers can also contribute to measurement uncertainty, albeit limited. Additionally, the measured angle of attack often strongly differs ($\mathcal{O}(1)$) from the angle of attack reported in the experiment design. Despite these factors, the Glasgow University dataset provides a reliable and well-characterised benchmark for validation of CFD simulations, having been used in previous studies on dynamic stall and unsteady aerodynamics [69, 39].

4.3.2. Static lift curve

An essential step in CFD validation is to replicate the static lift curve of an airfoil. Using the data prescribed previously, the static lift curve of the NACA0018 airfoil at Reynolds number $1.5e6$ was reconstructed. Figure 4.7 compares the experimentally-determined lift curve to the one found with URANS.

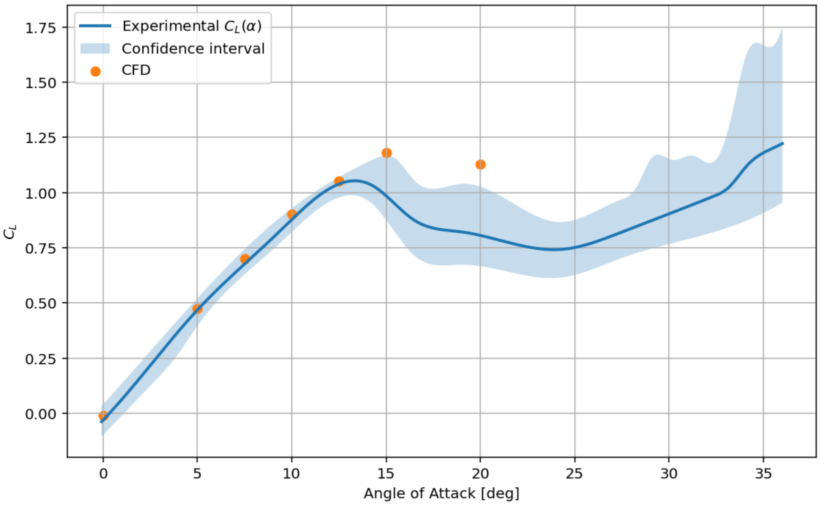

Figure 4.7: Static lift curve: University of Glasgow data [2] (line) and URANS data (orange dots).

As can be seen in Figure 4.7, the linear part of the lift curve is modelled accurately, but larger deviations start to appear after the experimental stall angle. This is consistent with the historical performance of (U)RANS models at high Reynolds numbers [86, 87]. This is a key limitation of (U)RANS models, and should be taken into account during further analyses with the CFD model. The confidence in flow cases that will be analysed at higher angles of attack with strong separation and reattachment behaviour is relatively low.

A comparison between the experimental static lift curve and the CFD is presented in Table 4.6. In this table, the static stall angle $\alpha_{C_{L,max}}$, $C_{L,max}$, $\alpha_{C_L=0}$ and lift curve slope C_{L_α} are presented.

Parameter	**Experiment**	**CFD**
Static stall angle $\alpha_{C_{L,\text{max}}}$	$13.5°$	$15°$
$C_{L,\text{max}}$	1.05	1.18
Zero-lift angle $\alpha_{C_L=0}$	0	0
Lift curve slope C_{L_α}	5.34rad^{-1}	5.43rad^{-1}

Table 4.6: Comparison between experimental static lift curve and CFD

4.3.3. Static pressure distribution

The static pressure distribution is also an important factor in the validation of a CFD model, and especially for the tuning of dynamic stall models, as these depend on the pressure evolution. Two angles of attack, within the attached range, will be analysed: $5°$ and $10°$. The pressure coefficient is determined as given by Equation 4.11.

$$c_p = \frac{p - p_\infty}{0.5\rho U_\infty^2} \tag{4.11}$$

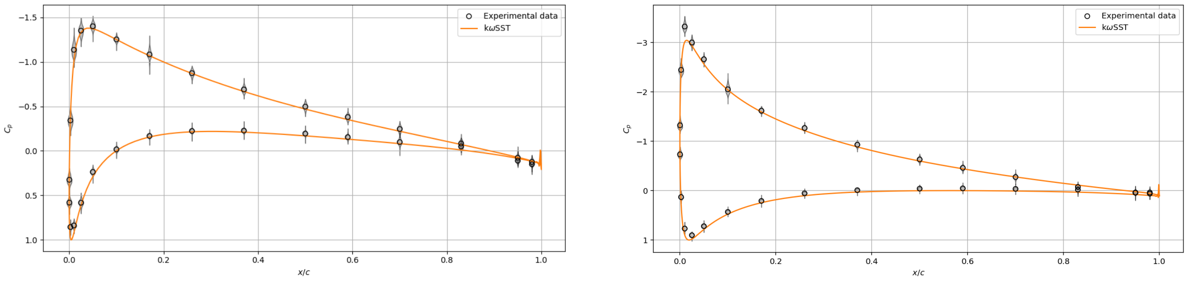

(a) Caption for $\alpha = 5°$ **(b)** Caption for $\alpha = 10°$

Figure 4.8: Pressure coefficient distributions for angles of attack $\alpha = 5°$, $\alpha = 10°$ CFD data compared to experimental data from [2]

Figure 4.8 shows that the pressure coefficient distribution obtained from URANS agrees with experimentally obtained pressure data. For the higher angle of attack $\alpha = 10°$, the predicted peak pressure coefficient is lower than the experimentally found data. This is consistent with typical (U)RANS performance. These results build confidence in the model to be able to predict the pressure evolution over the airfoil.

4.3.4. Dynamic flow cases

The Glasgow University dataset also contains dynamic airfoil data of the NACA0018 airfoil. This data is used to provide an additional validation of the model. Four main flow cases are compared, representative of those needed to tune dynamic stall models. The airfoil response is presented in Figure 4.9 for one of the four representative cases. It uses the average of 10 converged cycles.

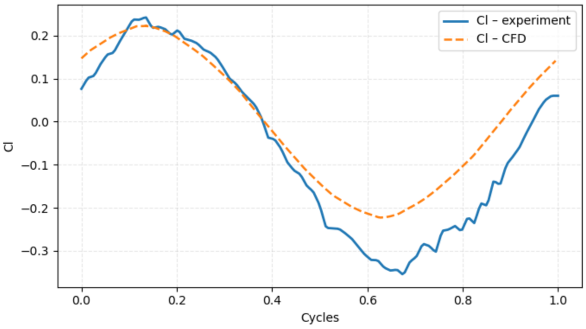

Figure 4.9: Dynamic experimental data from [2] (blue line), compared to computed CFD Data (orange line)

Figure 4.9 shows that the order of magnitude of the lift coefficient time series is similar to the experimental one. However, some differences exist. A first origin could be from measurement and/or reporting errors in angles of attack in the experiment. The reported and measured angle of attack differ, as can be seen in Figure 4.10. Additionally, dynamic experiments introduce strong unsteady effects in the tunnel, which can also influence the lift experienced. It can also be seen in Figure 4.9 that the experimental data are fairly noisy, indicating unsteadiness and measurement uncertainty.

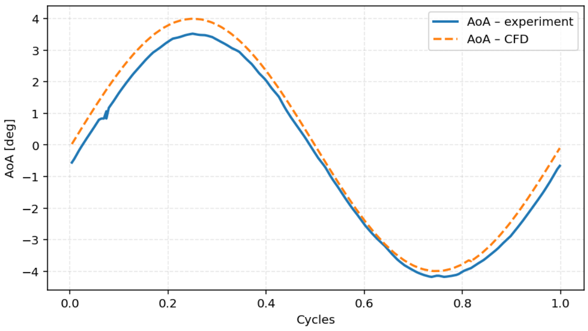

Figure 4.10: Measured angle of attack in [2] (blue line), compared to reported angle of attack used for CFD Data (orange line)

To conclude, given the validated static lift curve and pressure distribution around the airfoil. The confidence in the URANS calculations are sufficient in the attached-flow region.

5

Tuning

The calibration of dynamic stall models has been a recurring challenge in aeroelastic modelling. According to Melani et al., many variants of the Beddoes-Leishman (BL) model have historically been tuned by sub-optimal procedures, often relying on numerical optimisation over a limited set of airfoils while neglecting the physical assumptions underlying the model [19]. In contrast, this chapter proposes a more systematic approach to tuning, combining both global numerical optimisation on a large set of airfoil experimental simulations and physics-based procedures.

Two tuning strategies are analysed in the present work, using experimental data from the Glasgow University dynamic stall database [60]. The first is a global numerical tuning, which aims to optimise the dynamic stall model to the entire dataset, simultaneously to obtain parameter sets that minimise error across a wide range of operating conditions. The second follows a physics-informed approach, based on the original procedure described by Beddoes and Leishman [36] and highlighted in [19], in which different parameter groups are tuned sequentially according to the flow regime they represent. This procedure from Leishman and Beddoes [36] is adapted to the Risø dynamic stall model [7], which is derived from the BL model but employs a more compact formulation.

Madsen [7] provided tuned parameters for a flat plate and a Risø A1-24 airfoil, yet without offering a general calibration methodology. Moreover, values for the time constants T_p and T_f were not reported. In current aeroelastic solvers and the default values in this thesis, flat-plate values from Risø are often combined with the original BL time constants [36], a practice which underscores the need for a consistent and physically grounded tuning framework. Establishing such a framework can significantly improve the predictive capability of the model.

In addition to the experimental database, the proposed tuning strategies will later be applied to data obtained from CFD simulations, as introduced in chapter 4. Although the CFD dataset will be smaller due to computational constraints, the same methodology can be extended to larger numerical databases in future work.

5.1. Sensitivity of dynamic stall parameters

Before defining tuning strategies, it is essential to understand how each dynamic stall parameter influences the aerodynamic response and the resulting VAWT-level performance. Using the actuator cylinder model, as defined in section 2.3. This section quantifies how variations in A_i, b_i, T_p, and T_f influence the power coefficient of a VAWT.

5.1.1. A_i, b_i

The parameters A_1, A_2, b_1, and b_2 define the indicial lift response derived from Wagner and Kussner theory (see subsection 3.3.1). Here, $\pm 30\%$ perturbations are applied to assess their influence on attached-flow lift dynamics and the resulting C_P variation predicted by the actuator-cylinder rotor model.

The impact on the power curve is shown in Figure 5.1, and key performance indicators are presented in Table 5.1.

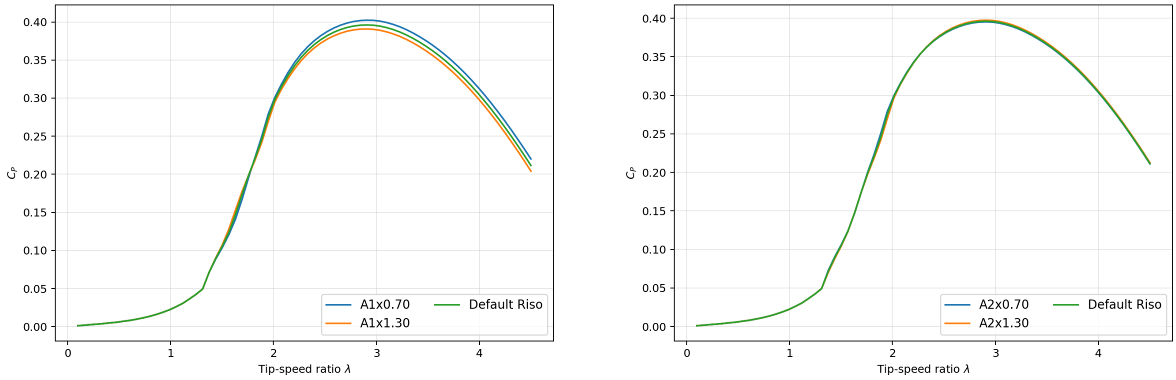

(a) A_1 sensitivity

(b) A_2 sensitivity

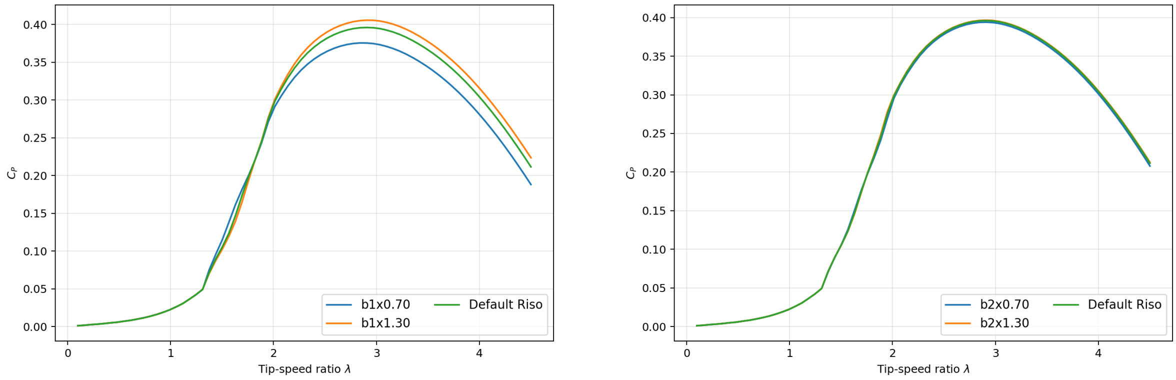

(c) b_1 sensitivity

(d) b_2 sensitivity

Figure 5.1: Sensitivity of pressure coefficient curve to variations in dynamic stall parameters A_1, A_2, b_1, and b_2

Table 5.1: Sensitivity of A_1, A_2, b_1, and b_2 to a $\pm 30\%$ change in the parameter

Parameter	$\Delta \mathbf{C}_{\mathbf{p,max}}^{-30\%}$ [%]	$\Delta \mathbf{C}_{\mathbf{p,max}}^{+30\%}$ [%]
A_1	6.1	1.3
A_2	-0.2	0.3
b_1	-5.2	2.4
b_2	-0.5	0.1

The impact of the attached flow parameters can be seen in Figure 5.1 and Table 5.1. A change of 30% can influence the maximum power coefficient by more than 6%. Contrary to the maximum power coefficient, the optimal tip speed ratio remains constant.

The results of the sensitivity study clearly show an increase in power with a decrease in A_1 and A_2. These A_1 and A_2 regulate the magnitude of the transient response compared to the static (instantaneous) response (see Equation 5.1, Equation 5.2). A lower value thus indicates that the airfoil response to a change in angle of attack will be closer to the instantaneous static value of the lift curve at that angle of attack. The higher power production at lower A_1 and A_2 indicates that the VAWT analysed has a higher power output for airfoils that have a smaller transient response to a change in angle of attack.

For b_1 and b_2, the power output of the VAWT increases with an increase in b_1 and b_2. The reasoning is similar to the reasoning for A_1 and A_2. A larger b_1 and b_2 cause the airfoil to reach the so-called ”steady-state” response more quickly. A higher b_1 and b_2 thus has a similar effect to a lower A_1 and A_2, so that the transient response is less pronounced. Thus, the VAWT will generate a higher power.

$$C_L^p = 2\pi\alpha_E = 2\pi(1 - A_1 - A_2 + x_1 + x_2) \tag{5.1}$$

$$\begin{aligned} x_1 &\propto A_1 e^{-b_1 s} \\ x_2 &\propto A_2 e^{-b_2 s} \end{aligned} \tag{5.2}$$

5.1.2. T_p, T_f

A similar approach can be taken to analyse the effect of varying T_p and T_f. The power output of a VAWT is computed with varying T_p and T_f. The variation is again taken as $\pm 30\%$. The results of the analysis can be seen in Figure 5.2 and Table 5.2.

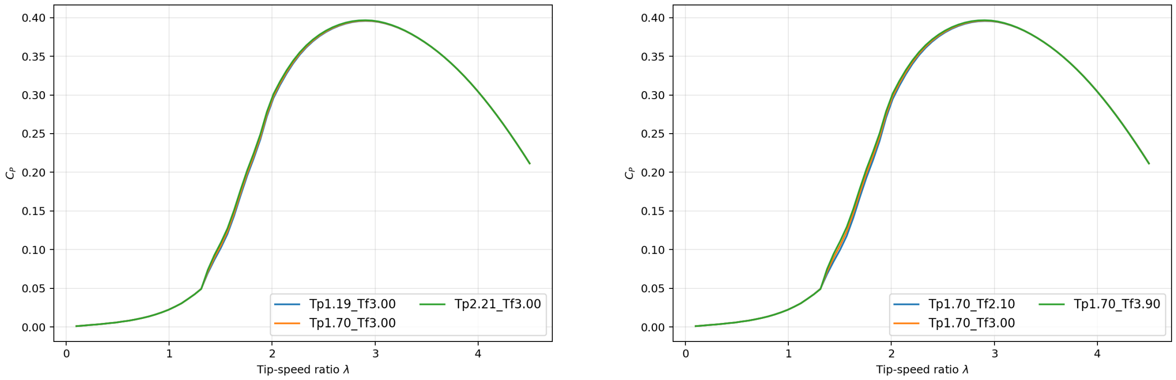

(a) T_p sensitivity

(b) T_f sensitivity

Figure 5.2: Sensitivity of the pressure coefficient distribution to variations in the time constants T_p and T_f.

Table 5.2: Sensitivity of T_p and T_f to a $\pm 30\%$ change in the parameter, increase in max power coefficient in percentage

Parameter	$\mathbf{C_{p,max}^{-30\%}}$ [%]	$\mathbf{C_{p,max}^{+30\%}}$ [%]
T_p	-0.13	0.13
T_f	-0.15	0.13

As shown in Figure 5.2 and Table 5.2, the effect of a varying T_p and T_f is less pronounced than the effect of the attached flow parameters. There is only a small effect at lower tip speed ratios. These time parameters have a lower impact on the optimal tip speed ratio because the flow will be attached for a larger part of the cycle at these higher tip speed ratios. Since the T_p and T_f mainly model the delay of pressure build-up and stall, these effects are less pronounced. Contrarily, at lower tip-speed ratios, the angle of attack excursion will be larger. Therefore, more separation and stall-like behaviour will occur, which increases the effect of the time lag parameters T_p and T_f.

5.2. Physics-informed tuning using experimental data

Following the framework of Beddoes-Leishman and the refinements by Melani [19], the Glasgow University dataset (section 4.3) is used to sequentially tune the parameters of the Risø model in a physically meaningful way. These parameters are tuned under attached flow (A_1, A_2, b_1, b_2), light stall (T_p), and early separation (T_f) conditions.

5.2.1. Attached flow: A_i, b_i

The first set of parameters to be calibrated is A_1, A_2, b_1, and b_2. As described in section 3.3, these govern the unsteady aerodynamic response of the airfoil to harmonic motion. They are rooted in Theodorsen's theory [51], which applies to thin, incompressible airfoils under small-amplitude oscillations and low reduced frequencies, i.e. conditions corresponding to attached flow.

The parameters A_1, A_2, b_1, and b_2 represent the indicial response to an arbitrary motion, by integrating the response to a step change of angle of attack or velocity using Duhamel's integral, as discussed in subsection 3.3.1. These indicial functions are Wagner functions for step changes in angle of attack, and Kussner functions for velocity steps [57].

Wagner functions assume that the resulting lift force is precisely half of the steady-state step value and that the response increases monotonically to the steady-state limit. This would lead to the bounds: $A_1 + A_2 = 0.5$. Kussner functions, on the other hand, assume that the lift response rises from an initial value of zero. This would lead to the constraint that $A_1 + A_2 = 1$, which clashes with the Wagner function constraint. The original Bedoes-Leishman model [10] suggests using Kussner functions and constrains the values of A_1 and A_2 accordingly. However, the original description of the Risø model acknowledges the different applications of these functions. The default values proposed by Risø for a flat plate dynamic response correspond to the Wagner function constraint (see Table 3.2). However, tuned values for the Risø A1-24 airfoil presented show no strong constraint on these values that correspond to either Wagner or Kussner functions, but lie somewhere in between: $0.5 < A_1 + A_2 < 1$. Unfortunately, no formal description of the tuning process is outlined. However, it is reasonable to assume the combined response to a gust and an angle of attack will be somewhere in between the theoretical responses of both. b_1 and b_2 are parameters related to the timescales, and should be larger than 0.

To identify suitable cases for tuning, experimental data from the Glasgow University database are selected for configurations that most closely match these assumptions. Specifically, cases with reduced frequency $k < 0.2$ and maximum angle of attack $\alpha < 5$ are selected. The parameters are then obtained through a least-squares optimisation, minimising the mean squared error between the experimental and modelled normal force coefficients. An example of the resulting calibration is shown in Figure 5.3, where the lift response using potential flow theory is plotted against experimental results.

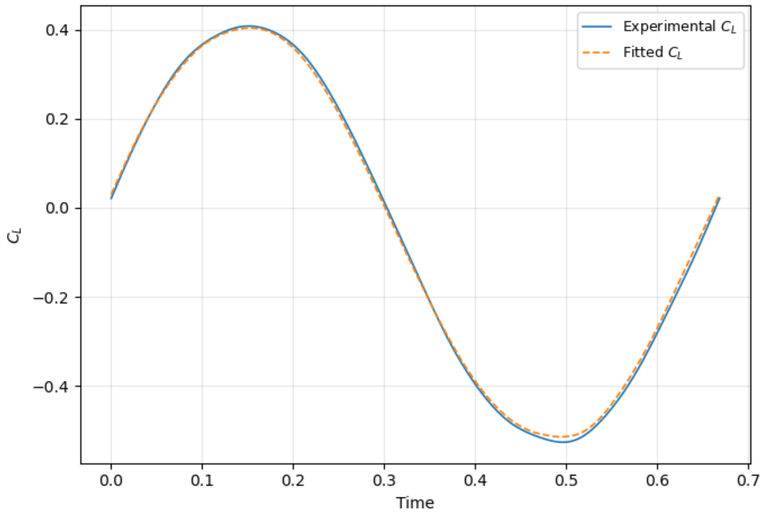

Figure 5.3: Illustration of A_i, b_i tuning based on attached-flow cases. Example of one case.

Figure 5.3 shows a representative tuning case, where the lift response to a small sinusoidal oscillation in angle of attack is compared between the experimental data and the attached flow module of the Risø model. The close agreement in amplitude and phase demonstrates that the selected cases are suitable for identifying A_i, b_i, and that the tuning procedure effectively captures the unsteady lift dynamics under attached-flow conditions.

Table 5.3: Attached flow parameters tuned with experimental data and physics-informed method

Parameter	Value
A_1	0.3720
A_2	0.6140
b_1	0.2876
b_2	0.5268

5.2.2. Pressure-lag constant T_p

The next variable, T_p, is a time constant associated with the lag in pressure response. This lag occurs between the forcing of the airfoil motion (e.g. angle of attack oscillations) and the corresponding normal coefficient predicted by potential flow. In both the Risø and original Beddoes-Leishman models, T_p regulates the delay of the leading-edge pressure peak in a mathematical sense. Physically, it models how long the attached flow conditions persist after the static stall limit has been exceeded. Therefore, the most suitable tuning cases are those where the flow is expected to remain attached, but the static separation point is slightly surpassed.

To tune T_p, the normal force coefficient C_N is compared to the pressure coefficient C_p measured at $x/c = 0.01$. By applying the correction for the dynamic lag using Equation 5.3 and Equation 5.4 with an appropriate value of T_p, the unsteadiness can be removed, and the C_p-C_N curve should collapse onto a single line. This procedure is illustrated in Figure 5.4.

The collapsing is performed by resampling the C_p-C_N curve so that all regions of the curve are equally represented. Subsequently, the C_p values are binned at each C_N, and the interquartile range as well as the maximum spread of the values are minimised. In this way, T_p is determined as the value that produces the tightest collapse of the curves.

$$C'_N = C_N - D_{Pn} \tag{5.3}$$

$$D_{P_n} = D_{P_{n-1}} e^{-\frac{\Delta S}{T_p}} + (C_{N_n} - C_{N_{n-1}}) e^{-\frac{\Delta S}{2T_p}} \tag{5.4}$$

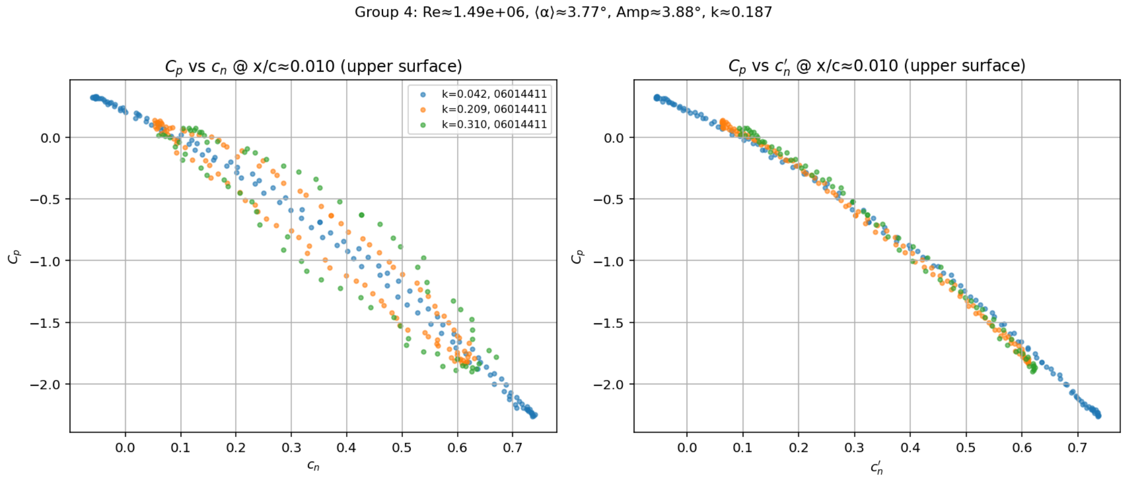

Figure 5.4: Collapse of C_p-C_N curves through tuning of the time constant T_p, performed by resampling and minimising the interquartile range of binned data.

From this procedure, an optimised value of $T_p = 1.06$ was obtained using Glasgow University data. This result differs somewhat from values reported in the literature, such as those by Mert [53], Melani [19], and Beddoes and Leishman [36], who reported values typically in the range of 1.7 to 2.5 for low subsonic flows. Nonetheless, the order of magnitude is consistent, indicating that the present tuning lies within the expected physical range. [10] also presents a range of T_p values based on Mach number. Inspecting these values, it can be seen that the T_p-value decreases with Mach number, with the lowest value presented being $T_p = 1.7$ at $M = 0.3$. This could be a potential justification of the lower value, as the experimental Mach number is equal to $M \approx 0.15$.

5.2.3. Boundary-layer lag constant T_f

T_f is a boundary-layer lag constant, weakly dependent on Mach number [36], and the effect of airfoil shape is still uncertain [19]. It is a parameter that regulates the movement of the unsteady separation point along the airfoil chord. It is thus best tuned with dynamic cases that experience light separation and/or stalling behaviour. It is best tuned on a case-by-case basis using unsteady boundary layer data or tuning it to unsteady airfoil data [19, 36].

Since there is no detailed boundary layer data available in the Glasgow University dataset, T_f is tuned by fitting the lift response of the Risø model with previously found attached flow parameters and pressure-lag time constant T_p to the unsteady airfoil lift data available. A mean-squared error (MSE) optimisation is performed on a selected number of VAWT motion experimental runs performed by Glasgow University. This combines experimental data with different flow cases related to VAWT operation.

The tuning using this method yields a value of $T_f = 9.61$

5.3. Global numerical optimisation

Several historical studies have been performed that also tuned the Bedoes-Leishman model (or derivatives of it) using a purely numerical optimisation method [53, 65]. This simplifies the tuning process and ensures the error between tuning data and the Risø model is guaranteed to be the smallest, assuming the global minimum error is found. A disadvantage of this method is that any link to the physics of the model is removed, a purely numerical minimum is found, without taking into account any physical meaning of the parameters.

Two different approaches are taken. The first one is an MSE optimisation, which minimises the error between the Risø model lift response and the experimentally found lift response to a change in angle of attack. The second approach takes a more results-centred approach. For each time series, some key criteria are defined, and the error between these criteria is minimised.

5.3.1. Mean-squared error tuning

A baseline tuning is performed using a mean-squared-error (MSE) objective applied to time-series $C_L(t)$ across selected sinusoidal and VAWT-relevant trajectories from the Glasgow dataset. The optimised Risø parameters can be seen in Table 5.5.

Since the parameter set has 6 variables, and the solution domain is not guaranteed to be smooth and linear, two different optimisation stages are used. First, a coarse least-squares optimisation is performed, with different starting guesses for the Risø parameters. The best solution from this coarse search is then used to further narrow down the solution near the coarse optimum. The optimisation is bounded according to previously established bounds. These can also be seen in Table 5.4.

Parameter	Lower bound	Upper bound
A_1	0	1
A_2	0	1
$A_1 + A_2$	0.5	1
b_1	0	-
b_2	0	-
T_p	0	-
T_f	0	-

Table 5.4: Bounds of Risø model tuning parameters

Table 5.5: Optimal Risø parameters using global MSE optimisation process

Parameter	Value
A_1	0.0872
A_2	0.4121
b_1	0.0116
b_2	0.9999
T_p	3.9146
T_f	9

5.3.2. Custom objective functions

A second objective function is designed to optimise the error in a more results-oriented manner. Instead of looking at the full timeseries, some key parameters are identified that describe the accuracy of a set of Risø parameters. These parameters can be seen in Table 5.6.

Table 5.6: Custom objective tuning parameters

Parameter	Weight
Phase-free MSE	1
$\Delta C_{L,max}$	5
$\Delta \alpha_{C_{L,max}}$	1
Phase lag $\Delta\phi$	0.5

The phase-free MSE forms the baseline component of the objective function. It measures the overall amplitude error between the modelled and reference lift response while intentionally removing phase effects. This ensures that the optimiser does not incorrectly penalise solutions that reproduce the correct load magnitude but differ slightly in temporal alignment, which could generate large errors in the pure MSE tuning presented previously. The lag is estimated using a fast Fourier transform (FFT)-based circular cross correlation. The Risø timeseries is then shifted to reduce the lag as much as possible. Although the phase is excluded from the MSE component, it nevertheless plays a key role in VAWT performance and load predictions. Assigning it a moderate weight ensures that the optimiser accounts for dynamic consistency without allowing phase error to dominate the solution.

The difference in maximum lift coefficient, $\Delta C_{L,\text{max}}$, is assigned the largest weight because the magnitude of the lift overshoot is one of the dominant features of dynamic stall. Errors in predicting this peak directly affect blade load estimates, making this metric critical for ensuring that the model accurately captures the severity of the dynamic stall event. The shift in the angle of attack at maximum lift, $\Delta \alpha_{C_{L,\text{max}}}$, is included to evaluate whether the timing of stall onset is captured correctly. Even if the magnitude of $C_{L,\text{max}}$ is well reproduced, an inaccurate stall angle can alter the predicted sequence of aerodynamic events, affecting both stability analyses and fatigue-relevant loading cycles.

Together, these metrics form a balanced objective function that evaluates both the magnitude and timing of the key aerodynamic phenomena relevant to dynamic stall modelling. A least-square optimisation is utilised to obtain the optimal solution. The result in tuned parameters can be seen in this targeted approach provides an alternative optimisation. However, it is also important to acknowledge that this method does not necessarily provide a better solution compared to the pure MSE tuning.

Table 5.7: Optimised parameters using custom objective tuning

Parameter	Value
A_1	0.345
A_2	0.287
b_1	0.784
b_2	0.700
T_p	7.94
T_f	9.73

5.4. CFD-based tuning

A similar approach to the one presented in section 5.2 is taken using CFD-tuned data. The data is obtained using methods described in chapter 4. This chapter showed the potential of CFD to estimate the lift response to a varying angle of attack in the attached region.

5.4.1. Attached-flow parameters from CFD

The same approach is taken as the physics-based approach in subsection 5.2.1. CFD cases in the attached flow region are averaged over their last 5 cycles. The attached flow module of the Risø is then tuned using an MSE least-squares optimisation. The same bounds are employed as explained previously. Example fits can be seen in Figure 5.5.

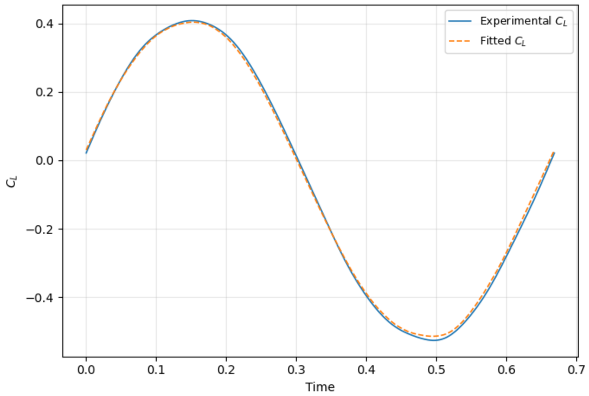

Figure 5.5: Illustration of A_i, b_i tuning based on attached-flow cases with CFD. Example of one case

Figure 5.5 shows very good agreement with the CFD data for the attached flow cases it has been designed for. However, for analyses at higher angles of attack, both the CFD and the attached flow model reach their limitations, and therefore, the fit and accuracy are less accurate. The final tuned values can be seen in Table 5.8.

Table 5.8: Attached flow parameters tuned with CFD data and physics-informed method

Parameter	Value
A_1	0.3488
A_2	0.6501
b_1	0.3406
b_2	0.4980

5.4.2. Lag constants from CFD

T_p-values are estimated from CFD time-series using the same collapse method as in the experimental tuning (subsection 5.2.2). Nonetheless, when applied to the numerical dataset, the method failed to produce results that could be considered consistent or physically meaningful. This has been attributed to the following causes: first, since the T_p is mainly dependent on the Mach number, this information is lost in the incompressible URANS simulation. This is also indicated in one of the CFD cases, which shows no lag between the pressure coefficient C_p and the normal coefficient C_n. This can be seen in Figure 5.6. However, this is not conclusive. Other CFD cases showed a negative lag, meaning that the pressure coefficient preceded the normal coefficient change, see Figure 5.7. In experimental data, the pressure coefficient response trails the normal coefficient. This is also the basis of the T_p parameter. It models how much the pressure coefficient C_p lags the normal coefficient C_N. It can therefore be concluded that the T_p-tuning cannot be performed reliably using incompressible URANS simulations.

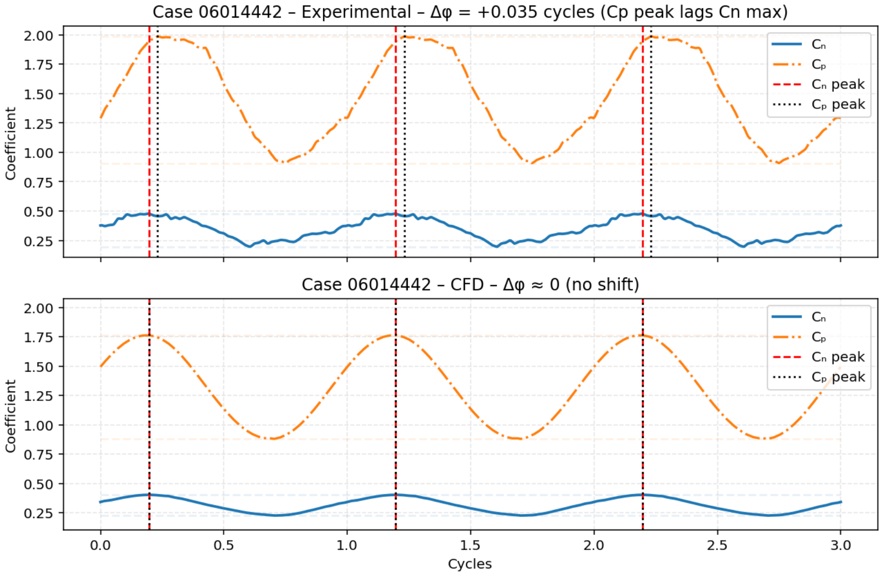

Figure 5.6: Comparison of timeseries of experimental data time lag between pressure coefficient and normal coefficient (top) with CFD lift and pressure coefficient timeseries (bottom)

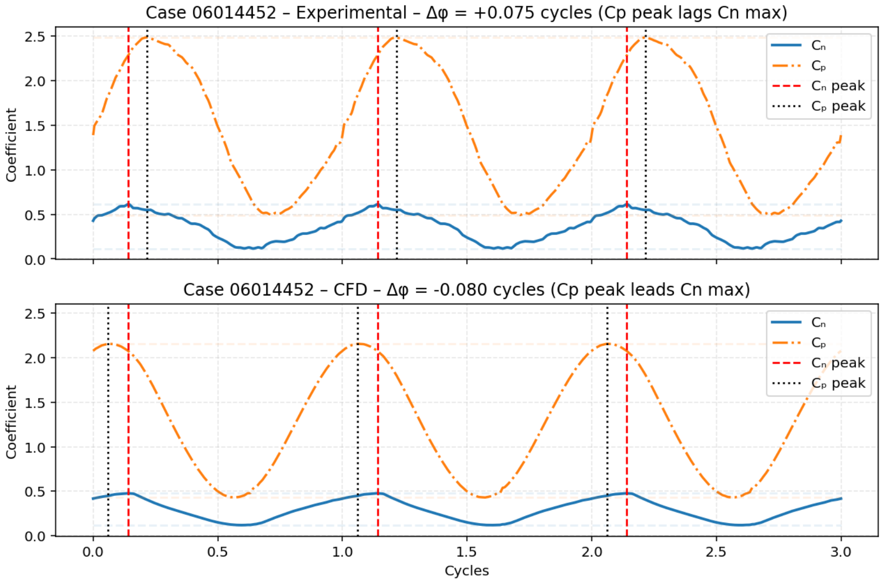

Figure 5.7: Comparison of timeseries of experimental data time lag between pressure coefficient and normal coefficient (top) with CFD lift and pressure coefficient timeseries (bottom)

Figure 5.6 and Figure 5.7 show the inability of CFD to tune the T_p coefficient. In the experimental data (top half of the graph), the peak in the pressure coefficient lags behind the peak of the normal coefficient. In the CFD-data, this lag is either not apparent (Figure 5.6) or negative (Figure 5.7).

The T_f parameter can also not be tuned reliably with incompressible URANS data. It is tuned using flow cases with high levels of separation and reattachment. chapter 4 has shown that the CFD setup presented cannot catch these flow phenomena accurately. The T_f-tuning will therefore not be carried out in this study.

5.5. Tuning results and model performance

Based on the different tuning methods presented, 4 new parameter sets have been determined. They are presented in Table 5.9, which also includes the default values presented in [7]. The impact of varying these changing values will be analysed on the airfoil-level and the VAWT-level.

Table 5.9: Risø tuning parameters

Data source	**Tuning Method**	$\mathbf{A_1}$	$\mathbf{A_2}$	$\mathbf{b_1}$	$\mathbf{b_2}$	$\mathbf{T_p}$	$\mathbf{T_f}$
-	Default values	0.165	0.335	0.0455	0.300	1.7	3
Glasgow University	Physics-informed	0.372	0.614	0.288	0.527	1.06	9.6
Glasgow University	MSE-based	0.087	0.412	0.0116	0.999	3.92	9
Glasgow University	Custom objective function	0.345	0.287	0.784	0.700	7.94	9.7
CFD	Physics-informed	0.349	0.650	0.341	0.498	1.06	9.6

While the individual parameter values differ strongly, this does not necessarily translate into a significant variation in the resulting airfoil response. Multiple combinations of attached-flow parameters are capable of producing airfoil-level dynamics that remain largely equivalent

5.5.1. Airfoil-level performance

Using the Glasgow University dataset, the response of different tuning parameters can be compared to the experimental response to a change in angle of attack representative of VAWT cases. This allows the comparison of the different models on the airfoil level. Both the lift timeseries and the $C_L(\alpha)$ curve are analysed. These graphs allow a qualitative interpretation of the results. Additionally, some error parameters are shown in Table 5.10 to have a quantitative error assessment. These errors are computed as averages for the whole Glasgow University VAWT dataset, which consists of 56 different run cases. They all have VAWT-like angle of attack motion, with amplitudes ranging from $5.4°$ to $32.8°$. A sample of the response of the different tuning parameters (shown in Table 5.9) is shown in Figure 5.8. This allows a visual comparison between the different tuning methods.

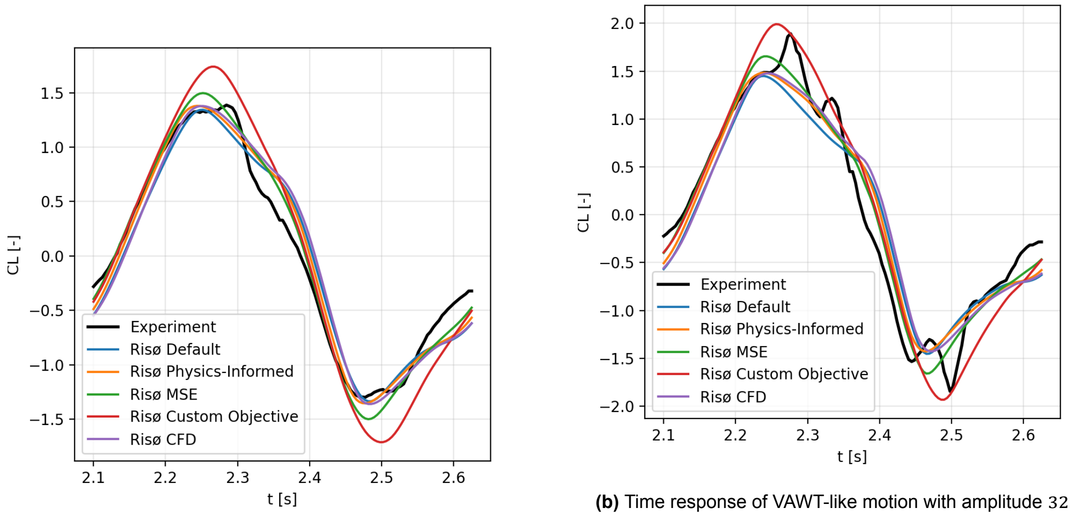

(a) Time response of VAWT-like motion with amplitude $22.6°$

(b) Time response of VAWT-like motion with amplitude $32.8°$. Different tuning parameters are compared to the experimental response

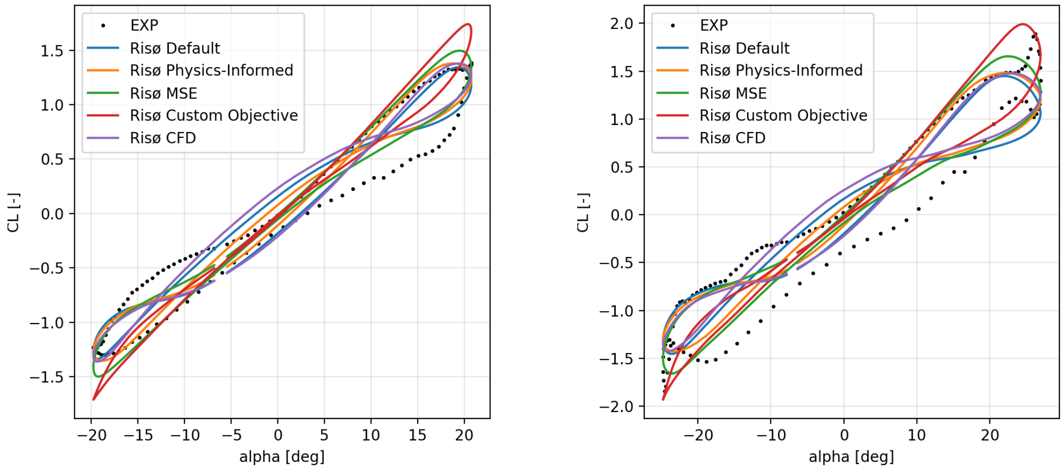

(c) $C_L(\alpha)$ of VAWT-like motion with amplitude $22.6°$

(d) $C_L(\alpha)$ of VAWT-like motion with amplitude $32.8°$

Figure 5.8: Timeseries and $C_L(\alpha)$ responses for VAWT-like motion with amplitudes 22.6 and 32.8

Figure 5.8 shows that the different tuning parameters all have different strengths and weaknesses. One general conclusion is that none of the models can accurately model the reattachment phase of the flow. The default parameter set visually lies very close to the physics-informed tuning sets, found by both CFD and experimental data. The major difference between these three sets is their phase. The three aforementioned tuning sets all have a phase lag compared to the experimental data. The global MSE error does not show this phase error as pronounced. This, however, comes with a slight lift overshoot compared to the other models.

Table 5.10: Different error metrics

Data source	Tuning Method	Mean Absolute Error
Risø	Default values	0.093
Glasgow University	Physics-informed	0.067
Glasgow University	MSE-based	0.066
Glasgow University	Custom objective function	0.098
CFD	Physics-informed	0.087

From Figure 5.8 and Table 5.10, it can be concluded that neither of the tuned Risø models shows a clear advantage in error for VAWT motion lift coefficient prediction. No conclusive answer can thus be given on which model performs the best and should be used in aero-elastic codes. Potentially, a combination of all models could provide a middle ground. The experimental MSE tuning could provide a good baseline for power production, as this reduces the error as much as possible over the whole cycle, which is important for VAWT power production. For the loading and strength analysis, the physics-informed tuning parameters provide a good agreement with the maximum lift coefficient, and could thus be used to perform ultimate strength and fatigue load analysis. For these analyses, the key criterion is the magnitude of the loads, and the lag is only of secondary importance.

5.5.2. Impact on VAWT performance

The airfoil-level performance did not provide a conclusive result on the performance of different tuning sets. Some small differences were apparent in the response to a VAWT airfoil motion. The effect of these differences is analysed on the turbine level using the actuator cylinder developed by [4] and described in section 2.3.

$C_P(\lambda)$ curves, optimal TSR λ_{opt}, and AEP are computed using the actuator-cylinder model, demonstrating the practical implications of the tuning for a VAWT rotor. The results of this analysis are shown in Figure 5.9 and Table 5.11. Figure 5.9 shows the power coefficient of the turbine, varying with tip speed ratio for the different sets. Table 5.11 shows some of the key metrics obtained from these power curves, as well as the difference in predicted Annual Energy Production (AEP) between the different tuning sets. The AEP is calculated based on a 10 m/s average wind speed assuming a Rayleigh wind distribution. This is the average wind speed defined in the IEC 61400 standard for wind turbine class I.

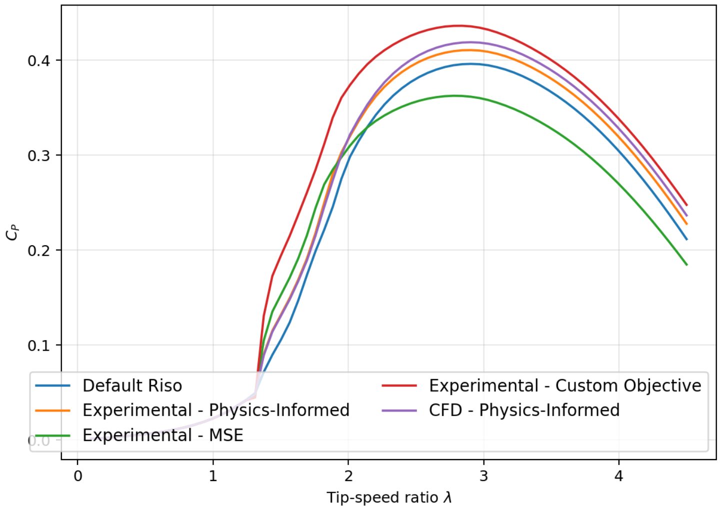

Figure 5.9: Predicted power coefficient curve for a three-bladed VAWT using an actuator cylinder model tuned using different tuning methods

Table 5.11: Comparison of dynamic stall models and parameter sets.

Data source	**Tuning Method**	$C_{P,\max}$	λ_{opt}	ΔAEP vs Default [%]
-	No DSM	0.42	2.97	2.29
Risø	Default values	0.39	2.91	*n.a.*
Glasgow University	Physics-informed	0.411	2.91	2.06
Glasgow University	MSE-based	0.36	2.78	-2.58
Glasgow Universisty	Custom Objective	0.44	2.84	5.27
CFD	Physics-informed	0.42	2.91	2.82

These analyses show that, even though the airfoil-level results show limited differences, the effect on the power output of the rotor can be significant. The physics-informed models show a noticeably higher power output compared to other models. Currently, there is no guarantee that a given tuning methodology will provide more accurate results than another. Therefore, future research should corroborate these results with experimental data from experimental VAWTs.

5.6. Tuning limitations

Despite the extensive tuning efforts, several remarks can be made. These apply to the certainty of the parameters and the generalisability of the tuned parameters. These limitations originate from modelling (both the Risø and CFD models) and dataset limitations. They include: model assumptions in the Risø formulation, limited dataset size (Reynolds number and number of airfoils), URANS limitations and the absence of drag and moment tuning.

First, the Risø model is a simplification of the Beddoes-Leishman model [36]. Simplifications have been made regarding incompressibility and vortex shedding. For the SeaTwirl VAWT concept, the incompressibility assumption can be seen as valid. Ignoring the Leading-Edge Vortex might not be valid. At lower Reynolds numbers, it was proven that the LEV is highly likely to occur (chapter 2). However, it is not guaranteed that the LEV will occur at higher Reynolds numbers. An attempt to investigate this assumption can be seen in Appendix A, which shows some flow field visualisations at Re=$1.5e6$ for a VAWT motion with TSR=3.2. There is a leading-edge vortex occurring in this flow case. However, this effect is expected to happen in the region where the accuracy of the CFD simulation is low. This conclusion might have to be analysed in more detail, and if it is found that the leading-edge vortex is consistently occurring, the Risø model could be extended with a leading-edge vortex module, as in the

Beddoes-Leishman model.

The second limitation is the dataset size used; the Glasgow University dataset contains a wide range of airfoils and Reynolds numbers analysed. However, the CFD was only carried out for one Reynolds number and one airfoil, with a limited number of pitching motions. The tuning was carried out to take this into account, with specific cases selected to tune certain parameters. But this limited set of simulations can lead to overfitting of the model to these simulations. Future work should thus include a larger number of airfoil shapes and pitching motions.

Moreover, the incompressible URANS also introduced some uncertainties. Firstly, the incompressible flow assumption limits the calculation of the time-lag parameters, as shown in subsection 5.4.2. URANS also smoothens out vortex structures, losing information useful for tuning these time-lag parameters. Incompressible URANS simulations could already provide a more accurate estimation of these parameters, but hybrid LES/RANS or LES models could provide more accurate data for the parameter tuning, albeit at a higher cost. The T_f parameter could also be tuned more accurately using dynamic separation point locations, instead of being fitted to match lift data.

Lastly, drag is not included in the tuning. There were two reasons for that. First of all, the Glasgow University dataset did not measure any forces using a balance, but instead used pressure measurements to calculate the forces. Therefore, only the pressure component of the forces is included. Any viscous force contributions cannot be analysed. For the normal force, which is the main contributor to the lift force, this is a reasonable assumption. The tangential force, on the other hand, has a larger viscous component. For higher Reynolds numbers, these viscous effects are less pronounced, but they were still chosen not to be included in the tuning.

6

Conclusions

6.1. Summary

Dynamic stall is a dominant aerodynamic mechanism in vertical-axis wind turbines. It arises directly from the cyclic and unsteady inflow experienced by the blades. The periodic variation of the angle of attack ensures that VAWTs operate in highly unsteady conditions. This large variation creates a strong hysteresis behaviour in the experienced lift on the blades. This hysteresis originates from stall delay and pressure build-up. Consequently, accurate modelling of dynamic stall is essential for predicting both power production and structural loading in stall-regulated VAWTs.

Semi-empirical dynamic stall models, such as the Risø adaptation to the Beddoes-Leishman, provide a computationally efficient method for incorporating unsteady aerodynamics into turbine-level aeroelastic simulations. However, this work has shown that their performance is highly sensitive to semi-empirical parameter tuning. Additionally, several key assumptions embedded in the Risø model, such as the dominance of trailing-edge separation and the simplified treatment of vortex lift, do not always align with the physical reality observed in experiments for VAWT-type kinematics. For instance, the inability of any tuned parameter set to reproduce the lift time-history from the Glasgow University experiments indicates that the model structure lacks sufficient flexibility to simultaneously capture stall delay, peak-lift overshoot, and reattachment timing. The deviations are especially noticeable in the separated flow regions of the model.

The CFD simulations performed, aimed to clarify the applicability and limitations of URANS for tuning of these semi-empirical stall models. As also shown in previous research, it can be concluded that URANS performs well in attached-flow states, both in static and dynamic cases. It can reliably model circulatory lift due to dynamic motion. The URANS calculations show the ability to capture vortex shedding, albeit with low confidence. This uncertainty mainly originates from the fact that URANS models struggle to reliably model separation and reattachment, which are key drivers of vortex build-up and shedding.

Using URANS data to tune the Risø model reveals that some, but not all, model features can be reliably calibrated using CFD. Parameters associated with attached-flow unsteadiness (e.g., A_1, A_2, b_1, b_2) show good consistency across CFD and experimental datasets, since URANS can predict those rather well. In contrast, parameters controlling separated-flow behaviour (e.g., T_p, T_f and the vortex-related terms) cannot reliably be captured. This is not critical to the Risø model tuning, though, as it has been shown in literature that these parameters are only slightly, if at all, affected by the airfoil shape. The airfoil shape mainly has an influence on the attached-flow parameters. Therefore, URANS models can be used in the early design phase of new experimental airfoils to determine these attached-flow parameters.

Taken together, these findings suggest a hybrid tuning strategy as an effective approach for tuning dynamic stall models for VAWTs. In this hybrid approach, CFD is used to determine airfoil-dependent parameters. These are mainly those related to attached-flow dynamics (A_1, A_2, b_1, b_2), while experimental data determine the parameters used in the vortex shedding modules that URANS cannot reliably reproduce. These parameters, however, are more generalisable and less airfoil-dependent. This approach balances cost, flexibility, and physical accuracy. It also enables the rapid exploration of new VAWT airfoil geometries, which is essential for concepts such as SeaTwirl's floating turbine, where full wind-tunnel characterisation across relevant Reynolds-number ranges is limited.

Overall, this thesis concludes that incompressible URANS models cannot replace experiments for dynamic stall model tuning, but they can act as a strong early-design phase tool to aid the tuning of these models. The semi-empirical models are also a crucial element in the design and verification of modern VAWTs, as dynamic stall is a key driver of loads and power production. It is therefore crucial to have an accurate way of tuning these models, to ensure uncertainties (which remain very large) in VAWTs can be reduced. This will aid the development and diversification of this alternative technology.

6.2. Limitations and recommendations

The results of this thesis highlight several limitations that require targeted follow-up work. Four main areas are identified, related to: (1) the accuracy and reliability of URANS, (2) the ability of dynamic stall models to model real-world dynamic stall, (3) the limited airfoil database, and (4) the uncertainty about the impact on the loads and power production of a full-scale turbine.

The present work demonstrated that the URANS approach is able to reproduce major unsteady features of the flow, but remains fundamentally limited in its ability to resolve separation and reattachment dynamics with sufficient fidelity for parameter identification. Another limitation of the current state of the art is the limited data available on dynamic stall. Only one database with one airfoil has been analysed, removing the generalisability of the model.

The analysis also confirmed that the Risø adaptation to the Beddoes–Leishman model provides a practical starting point for dynamic stall prediction but fails to reproduce several key features of VAWT-relevant unsteady aerodynamics. In particular, the model's assumptions regarding the LEV are not always consistent with the flow regimes observed in high reduced-frequency VAWT operation. Additionally, an extensive comparison of modern dynamic stall models for VAWT performance prediction is still absent in the literature. Early studies exist, but only tackle a limited number of dynamic stall models. Similarly, a key limitation of the current study is the lack of VAWT-scale validation for power coefficient predictions.

These limitations provide a clear starting point for future research, which can focus on tackling these limitations. A follow-up study would therefore focus on carrying out parameter tuning using higher-fidelity methods such as Large Eddy Simulations (LES) or hybrid RANS/LES (e.g., DDES). These approaches can capture vortex formation, convection, and breakup with considerably higher accuracy, providing a more defensible basis for estimating model parameters that are currently poorly constrained (e.g., separation-point dynamics and time constants). These higher-fidelity methods are considerably more computationally expensive, but a smart, targeted approach to specific parameters could provide sufficient accuracy with a reasonable computational cost.

Using the relatively cheap URANS simulations, a larger knowledge base can also be created. Such a database should cover a wider range of reduced frequencies, Mach numbers, Reynolds numbers, and pitch trajectories. This database should be constructed using wind tunnel tests of current airfoils, which can be used to generate confidence in a simulation. Once the confidence is high enough, the analysis can be extended to different Reynolds numbers and airfoils.

If dynamic stall models such as the Risø model continue to be used, their assumptions should be revisited in light of VAWT-specific applications. A first example could be by including an explicit LEV module. The current formulation of the Risø model does not include LEV effects, which is insufficient for the high-amplitude, short-timescale movement seen in VAWTs. A physically motivated LEV growth and convection model, as implemented in the original Beddoes-Leishman model, could improve the accuracy or confidence in these models. Different dynamic stall models can also be compared to find a suitable model for VAWT applications, as these applications experience very high angles of attack.

Furthermore, machine–learning–based parameter tuning may be effective when trained on a combined dataset of Glasgow University measurements and a large database of CFD results. Such regressions could reduce the manual tuning burden and provide shape-based parameter predictions for arbitrary airfoils. Full machine-learning-based dynamic stall models could also provide an interesting pathway for further research. However, the risks of overtraining and 'black-box' behaviour could limit confidence in these models. These models would only have a limited physical support.

Because no clear ranking among tuned parameter sets emerged in this research, experimental validation on a VAWT in a controlled environment is required. Without such validation, it is not possible to determine which parameter sets generalise beyond the Glasgow dataset or how errors in dynamic stall modelling influence system-level performance estimates. Similarly, the present work focused on time-resolved aerodynamic forces and basic power prediction. The implications for structural loading, a key driver in VAWTs, remain unknown. Future research should integrate the tuned dynamic stall models into aeroelastic simulations to quantify their effect on both ultimate and fatigue loads. Given that dynamic stall has an impact on the amplitude, frequency, and phasing of normal and tangential force and moment fluctuations, even moderate improvements in modelling accuracy may translate into noticeable differences in predicted lifetime loads.

Overall, future work should carry out high-fidelity CFD to identify currently uncertain dynamic stall mechanisms, development or identification of VAWT-specific dynamic stall formulations that handle the large angle of attack excursions, extension to a broader set of airfoils and operating conditions, and validation at turbine scale, using developed aeroelastic tools. These steps are necessary for reducing the uncertainty that currently limits the predictive capability of semi-empirical dynamic stall models for VAWT applications.

Bibliography

[1] Castellani, F., Astolfi, D., Peppoloni, M., Natili, F., Buttà, D., and Hirschl, A., "Experimental vibration analysis of a small scale vertical wind energy system for residential use," *Machines*, Vol. 7, No. 2, 2019. https://doi.org/10.3390/MACHINES7020035.

[2] Green, R. B., and Giuni, M., "Dynamic stall database R and D 1570-AM-01: Final Report," 2017. https://doi.org/10.5525/GLA.RESEARCHDATA.464.

[3] Hezaveh, S. H., Bou-Zeid, E., Dabiri, J., Kinzel, M., Cortina, G., and Martinelli, L., "Increasing the Power Production of Vertical-Axis Wind-Turbine Farms Using Synergistic Clustering," *Boundary-Layer Meteorology*, Vol. 169, No. 2, 2018, pp. 275–296. https://doi.org/10.1007/S10546-018-0368-0.

[4] Cheng, Z., Madsen, H. A., Gao, Z., and Moan, T., "Aerodynamic Modeling of Floating Vertical Axis Wind Turbines Using the Actuator Cylinder Flow Method," *Energy Procedia*, Vol. 94, 2016, pp. 531–543. https://doi.org/10.1016/J.EGYPRO.2016.09.232, URL https://www.sciencedirect.com/science/article/pii/S1876610216309195.

[5] Leishman, J. G., "Challenges in modelling the unsteady aerodynamics of wind turbines," *Wind Energy*, Vol. 5, No. 2-3, 2002, pp. 85–132. https://doi.org/10.1002/WE.62), URL https://onlinelibrary.wiley.com/doi/10.1002/we.62.

[6] Le Fouest, S., Fernex, D., and Mulleners, K., "Time scales of dynamic stall development on a vertical-axis wind turbine blade," *Flow*, Vol. 3, 2023, p. E11. https://doi.org/10.1017/FLO.2023.5, URL https://www.cambridge.org/core/journals/flow/article/time-scales-of-dynamic-stall-development-on-a-verticalaxis-wind-turbine-blade/7999A5BBEBABBA738ECE090809E52F6F.

[7] Hansen M H, Gaunaa, M., and Madsen, H. A., "A Beddoes-Leishman type dynamic stall model in state-space and indicial formulations," Tech. rep., Forskningscenter Risoe, 2004.

[8] Leong, W.-U. A., "A Study of the Aerodynamic and Mechanical Interference Effects Between Two Neighbouring Square Towers," 1987, pp. 21–41.

[9] Chen, W., Zheng, H., Yan, Z., and Chen, R., "Shape design of an artificial pump-lung using high-resolution hemodynamic simulation with high-performance computing," *Physics of Fluids*, Vol. 35, No. 3, 2023. https://doi.org/10.1063/5.0140986.

[10] Leishman, J. G., and Beddoes, T. S., "A generalised model for airfoil unsteady aerodynamic behaviour and dynamic stall using the indicial method," *Proceedings of the 42nd Annual forum of the American Helicopter Society*, Vol. 34, Washington DC, 1986, pp. 3–17.

[11] Barooni, M., Ashuri, T., Velioglu Sogut, D., Wood, S., and Ghaderpour Taleghani, S., "Floating Offshore Wind Turbines: Current Status and Future Prospects," *Energies 2023, Vol. 16, Page 2*, Vol. 16, No. 1, 2022, p. 2. https://doi.org/10.3390/EN16010002, URL https://www.mdpi.com/1996-1073/16/1/2/htmhttps://www.mdpi.com/1996-1073/16/1/2.

[12] ETIPWind Executive Committee, "FLOATING OFFSHORE WIND DELIVERING CLIMATE NEUTRALITY," Tech. rep., ETIPWind, 6 2020.

[13] Stehly, T., Duffy, P., and Mulas Hernando, D., "Cost of Wind Energy Review: 2024 Edition," Tech. Rep. NREL/PR-5000-91775, National Renewable Energy Laboratory, Golden, CO, 11 2024. https://doi.org/10.2172/2479271, URL https://www.nrel.gov/docs/fy25osti/91775.pdf.

[14] "Hywind Tampen - Equinor," , 2025. URL https://www.equinor.com/energy/hywind-tampen.

[15] Ghigo, A., Faraggiana, E., Giorgi, G., Mattiazzo, G., and Bracco, G., "Floating Vertical Axis Wind Turbines for offshore applications among potentialities and challenges: A review," *Renewable and Sustainable Energy Reviews*, Vol. 193, 2024, p. 114302. https://doi.org/10.1016/J.RSER.2024.114302, URL https://www.sciencedirect.com/science/article/pii/S136403212400025X.

[16] Principia, "AeroDeep Theory Guide 2.2," Tech. rep., Principia & IFP Energies Nouvelles, 1 2021.

[17] "OYE Model — QBlade Documentation 2.0.8 documentation," , 2024. URL https://docs.qblade.org/src/theory/aerodynamics/dynamic_stall/OYE_stall.html.

[18] Oye, S., "Dynamic stall, simulated as a time lag of separation," *Proceedings of the Fourth IEA Symposium on the Aerodynamics of Wind Turbines*, Rome, 1991, p. 28.

[19] Melani, P. F., Aryan, N., Greco, L., and Bianchini, A., "The Beddoes-Leishman dynamic stall model: Critical aspects in implementation and calibration," *Renewable and Sustainable Energy Reviews*, Vol. 202, 2024, p. 114677. https://doi.org/10.1016/J.RSER.2024.114677.

[20] Hand, B., Kelly, G., and Cashman, A., "Numerical simulation of a vertical axis wind turbine airfoil experiencing dynamic stall at high Reynolds numbers," *Computers & Fluids*, Vol. 149, 2017, pp. 12–30. https://doi.org/10.1016/J.COMPFLUID.2017.02.021.

[21] De Tavernier, D., and Ferreira, C. S., "A new dynamic inflow model for vertical-axis wind turbines," *Wind Energy*, Vol. 23, No. 5, 2020, pp. 1196–1209. https://doi.org/10.1002/WE.2480, URL https://onlinelibrary.wiley.com/doi/full/10.1002/we.2480https://onlinelibrary.wiley.com/doi/abs/10.1002/we.2480https://onlinelibrary.wiley.com/doi/10.1002/we.2480.

[22] Dabiri, J. O., "Potential order-of-magnitude enhancement of wind farm power density via counter-rotating vertical-axis wind turbine arrays," *Journal of Renewable and Sustainable Energy*, Vol. 3, No. 4, 2011. https://doi.org/10.1063/1.3608170/284824, URL /aip/jrse/article/3/4/043104/284824/Potential-order-of-magnitude-enhancement-of-wind.

[23] Abkar, M., "Theoretical Modeling of Vertical-Axis Wind Turbine Wakes," *Energies 2019, Vol. 12, Page 10*, Vol. 12, No. 1, 2018, p. 10. https://doi.org/10.3390/EN12010010, URL https://www.mdpi.com/1996-1073/12/1/10/htmhttps://www.mdpi.com/1996-1073/12/1/10.

[24] Hyae Ryung Kim, Quint Houwink, Petr Jenicek, Taicheng Jin, Abha Nirula, and Gernot Wagner, "Reconsidering Wind," , 3 2025. URL https://business.columbia.edu/insights/climate/wind.

[25] Kato, Y., Seki, K., and Y Shimizu, "Vertical axis wind turbine designed aerodynamically at Tokai University," *Symposium Tokay University*, 1981. URL https://pp.bme.hu/me/article/download/5832/4937/9590.

[26] Migliore, P. G., and Wolfe, W. P., "Effects of flow curvature on the aerodynamics of Darrieus wind turbines," 1980. https://doi.org/10.2172/5049529, URL http://www.osti.gov/servlets/purl/5049529/.

[27] Pan, J., Ferreira, C., and van Zuijlen, A., "A numerical study on the blade-vortex interaction of a two-dimensional Darrieus-Savonius combined vertical axis wind turbine," *Physics of Fluids*, Vol. 35, No. 12, 2023, p. 125152. https://doi.org/10.1063/5.0174394/2931797, URL /aip/pof/article/35/12/125152/2931797/A-numerical-study-on-the-blade-vortex-interaction.

[28] Aagaard Madsen, H., "Actuator cylinder. A flow model for vertical axis wind turbines," Ph.D. thesis, Institue of Industria Constructions and Energy Technology, 1 1982.

[29] Madsen, H. A., Larsen, T. J., Paulsen, U. S., and Vita, L., “Implementation of the Actuator Cylinder flow model in the HAWC2 code for aeroelastic simulations on vertical Axis Wind Turbines,” *51st AIAA Aerospace Sciences Meeting including the New Horizons Forum and Aerospace Exposition 2013*, 2013. https://doi.org/10.2514/6.2013-913, URL /doi/pdf/10.2514/6.2013-913.

[30] Burton, T., Jenkins, N., Bossanyi, E., Sharpe, D., and Graham, M., “Wind Energy Handbook, Third Edition,” *Wind Energy Handbook, Third Edition*, 2024, pp. 1–988. https://doi.org/10.1002/9781119992714.

[31] Aihara, A., Mendoza, V., Goude, A., and Bernhoff, H., “A numerical study of strut and tower influence on the performance of vertical axis wind turbines using computational fluid dynamics simulation,” *Wind Energy*, Vol. 25, No. 5, 2022, pp. 897–913. https://doi.org/10.1002/WE.2704, URL /doi/pdf/10.1002/we.2704https://onlinelibrary.wiley.com/doi/abs/10.1002/we.2704https://onlinelibrary.wiley.com/doi/10.1002/we.2704.

[32] Siddiqui, M. S., Durrani, N., and Akhtar, I., “Numerical study to quantify the effects of struts & central hub on the performance of a three dimensional vertical axis wind turbine using sliding mesh,” *American Society of Mechanical Engineers, Power Division (Publication) POWER*, Vol. 2, 2013. https://doi.org/10.1115/POWER2013-98300.

[33] Tavernier, D., “Aerodynamic advances in vertical-axis wind turbines,” 2021. https://doi.org/10.4233/UUID:7086F01F-28E7-4E1B-BF97-BB3E38DD22B9, URL https://repository.tudelft.nl/record/uuid:7086f01f-28e7-4e1b-bf97-bb3e38dd22b9.

[34] Goude, A., “Fluid mechanics of vertical axis turbines: Simulations and model development,” 2012. URL https://www.diva-portal.org/smash/record.jsf?pid=diva2:564033.

[35] Le Fouest, S., and Mulleners, K., “The dynamic stall dilemma for vertical-axis wind turbines,” *Renewable Energy*, Vol. 198, 2022, pp. 505–520. https://doi.org/10.1016/j.renene.2022.07.071, URL https://arxiv.org/pdf/2204.06560.

[36] Leishman, J. G., and Bcddoes, T. S., “A Semi-Empirical Model for Dynamic Stall,” *Journal of the American Helicopter Society*, Vol. 34, No. 3, 1989, pp. 3–17. https://doi.org/10.4050/JAHS.34.3.

[37] Tran, C. T., and Petot, D., “Semi-empirical model for the dynamic stall of airfoils in view of the application to the calculation of responses of a helicopter blade in forward flight,” 1980.

[38] Holierhoek, J. G., De Vaal, J. B., Van Zuijlen, A. H., and Bijl, H., “Comparing different dynamic stall models,” *Wind Energy*, Vol. 16, No. 1, 2013, pp. 139–158. https://doi.org/10.1002/WE.548.

[39] Faber, M. J., “A comparison of dynamic stall models and their effect on instabilities,” Tech. rep., Delft University of Technology, 2018. URL https://repository.tudelft.nl/record/uuid:0001b1eb-c19f-48c3-973d-57eca4996a91.

[40] Bierbooms, W. A., “A comparison between unsteady aerodynamic models,” *Journal of Wind Engineering and Industrial Aerodynamics*, Vol. 39, No. 1-3, 1992, pp. 23–33. https://doi.org/10.1016/0167-6105(92)90529-J, URL https://www.sciencedirect.com/science/article/pii/016761059290529J.

[41] Ning, A., “Actuator cylinder theory for multiple vertical axis wind turbines,” *Wind Energy Science*, Vol. 1, No. 2, 2016, pp. 327–340. https://doi.org/10.5194/WES-1-327-2016.

[42] Ferreira, C. S., Madsen, H. A., Barone, M., Roscher, B., Deglaire, P., and Arduin, I., “Comparison of aerodynamic models for Vertical Axis Wind Turbines,” *Journal of Physics: Conference Series*, Vol. 524, No. 1, 2014, p. 012125. https://doi.org/10.1088/1742-6596/524/1/012125, URL https://iopscience.iop.org/article/10.1088/1742-6596/524/1/012125https://iopscience.iop.org/article/10.1088/1742-6596/524/1/012125/meta.

[43] Gülçat, U., *Fundamentals of Modern Unsteady Aerodynamics*, Springer International Publishing, 2021. https://doi.org/10.1007/978-3-030-60777-7/COVER.

[44] Mccroskey, W. J., “The Phenomenon of Dynamic Stall,” Tech. rep., NASA, 1981.

[45] Ramesh, K. K., Ke, J., Gopalarathnam, A., and Edwards, J. R., “Effect of airfoil shape and reynolds number on leading edge vortex shedding in unsteady flows,” *30th AIAA Applied Aerodynamics Conference 2012*, 2012, pp. 1505–1515. https://doi.org/10.2514/6.2012-3025, URL https://arc.aiaa.org/doi/10.2514/6.2012-3025.

[46] Narsipur, S., “Effect of Reynolds number and airfoil thickness on the leading-edge suction in unsteady flows,” *Theoretical and Computational Fluid Dynamics*, Vol. 36, No. 5, 2022, pp. 845–863. https://doi.org/10.1007/S00162-022-00621-2/FIGURES/24, URL https://link.springer.com/article/10.1007/s00162-022-00621-2.

[47] Pereira, R. S., “Dynamic Stall,” *Handbook of Wind Energy Aerodynamics: With 678 Figures and 33 Tables*, 2022, pp. 331–351. https://doi.org/10.1007/978-3-030-31307-4{_}14/FIGURES/4, URL https://link.springer.com/referenceworkentry/10.1007/978-3-030-31307-4_14.

[48] Simão Ferreira, C., Van Kuik, G., Van Bussel, G., and Scarano, F., “Visualization by PIV of dynamic stall on a vertical axis wind turbine,” *Experiments in Fluids*, Vol. 46, No. 1, 2009, pp. 97–108. https://doi.org/10.1007/S00348-008-0543-Z/FIGURES/20, URL https://link.springer.com/article/10.1007/s00348-008-0543-z.

[49] Buchner, A. J., Soria, J., Honnery, D., and Smits, A. J., “Dynamic stall in vertical axis wind turbines: scaling and topological considerations,” *Journal of Fluid Mechanics*, Vol. 841, 2018, pp. 746–766. https://doi.org/10.1017/JFM.2018.112, URL https://www.cambridge.org/core/journals/journal-of-fluid-mechanics/article/dynamic-stall-in-vertical-axis-wind-turbines-scaling-and-topological-considerations/1DC59C2F9D2D13666EEADB3144699282.

[50] Persico, R. . G., “Impact of dynamic stall on VAWT performance: implementation into a Double Multiple Stream-Tube tool and quantification of model uncertainty,” Tech. rep., Politecnico di Milano, 2019.

[51] Theodorsen, T., “General Theory of Aerodynamic Instability and the Mechanism of Flutter,” , 1935.

[52] Snel, H., “Heuristic modelling of dynamic stall characteristics,” *EWEC-CONFERENCE*, 1997, pp. 429–433.

[53] Mert, M., “Optimization of Semi Empirical Parameters in the FFA Beddoes Dynamic Stall Model,” *FFA*, 1999.

[54] Gupta, S., and Leishman, J. G., “Dynamic stall modelling of the S809 aerofoil and comparison with experiments,” *Wind Energy*, Vol. 9, No. 6, 2006, pp. 521–547. https://doi.org/10.1002/WE.200;PAGE:STRING:ARTICLE/CHAPTER, URL /doi/pdf/10.1002/we.200https://onlinelibrary.wiley.com/doi/abs/10.1002/we.200https://onlinelibrary.wiley.com/doi/10.1002/we.200.

[55] Sorensen, N., Bertagnolio, F., Jost, E., and Lutz, T., “Aerodynamic effects of compressibility for wind turbines at high tip speeds,” *Journal of Physics: Conference Series*, Vol. 1037, No. 2, 2018, p. 022003. https://doi.org/10.1088/1742-6596/1037/2/022003, URL https://iopscience.iop.org/article/10.1088/1742-6596/1037/2/022003https://iopscience.iop.org/article/10.1088/1742-6596/1037/2/022003/meta.

[56] Yan, C., and Archer, C. L., “Assessing compressibility effects on the performance of large horizontal-axis wind turbines,” *Applied Energy*, Vol. 212, 2018, pp. 33–45. https://doi.org/10.1016/J.APENERGY.2017.12.020, URL https://www.sciencedirect.com/science/article/pii/S0306261917317348.

[57] Newman, J. N., “Marine Hydrodynamics,” The MIT Press, 2018, pp. 229–232.

[58] Thwaites, B., *Incompressible aerodynamics; an account of the theory and observation of the steady flow of incompressible fluid past aerofoils, wings, and other bodies.*, Clarendon Press, Oxford, 1960.

[59] Brill, P. A., Pool, D. M., and de Visser, C. C., "Improved Kirchhoff Stall Model Parameter Estimation Accuracy through Optimal Data Slicing," *AIAA Science and Technology Forum and Exposition, AIAA SciTech Forum 2025*, 2025. https://doi.org/10.2514/6.2025-1248, URL https://arc.aiaa.org/doi/10.2514/6.2025-1248.

[60] Galbraith, R., Gracey, M., and Leitch, E., "Summary of Pressure Data for Thirteen Aerofoils on the University of Glasgow's Aerofoil Database. G.U. Aero Report 9221," 1992.

[61] Abbott, I. H., and Von Doenhoff, A. E., *Theory of wing sections: including a summary of airfoil data*, Dover Publications, Mineola, 1999. URL http://app.knovel.com/hotlink/toc/id:kpTWSISAD3/theory-of-wing.

[62] Jones, J. P., and Council, A. R., *The influence of the wake on the flutter and vibration of rotor blades.*, Aeronautical Research Council, Teddington, 1956.

[63] Fuglsang, P., and Dahl, K. S., "Design of the new Risø-A1 airfoil family for wind turbines," *1999 European Wind Energy Conference*, Routledge, 2014, pp. 134–137.

[64] Mohamed, O. S., Melani, P. F., Bangga, G., Aryan, N., Greco, L., and Bianchini, A., "Accuracy assessment of Beddoes-Leishman and IAG dynamic stall models for wind turbine applications," *Journal of Physics: Conference Series*, Vol. 2767, No. 5, 2024, p. 052053. https://doi.org/10.1088/1742-6596/2767/5/052053, URL https://iopscience.iop.org/article/10.1088/1742-6596/2767/5/052053https://iopscience.iop.org/article/10.1088/1742-6596/2767/5/052053/meta.

[65] Singapore Wala, A. A., Ng, E. Y., and Narasimalu, S., "A Beddoes-Leishman–type model with an optimization-based methodology and airfoil shape parameters," *Wind Energy*, Vol. 21, No. 7, 2018, pp. 590–603. https://doi.org/10.1002/WE.2180, URL /doi/pdf/10.1002/we.2180https://onlinelibrary.wiley.com/doi/abs/10.1002/we.2180https://onlinelibrary.wiley.com/doi/10.1002/we.2180.

[66] Huang, B., Wang, P., Wang, L., Cao, T., Wu, D., and Wu, P., "A combined method of CFD simulation and modified Beddoes-Leishman model to predict the dynamic stall characterizations of S809 airfoil," *Renewable Energy*, Vol. 179, 2021, pp. 1636–1649. https://doi.org/10.1016/J.RENENE.2021.07.131, URL https://www.sciencedirect.com/science/article/pii/S0960148121011411#sec6.

[67] Wang, Q., Zhao, Q., and Wu, Q., "Aerodynamic shape optimization for alleviating dynamic stall characteristics of helicopter rotor airfoil," *Chinese Journal of Aeronautics*, Vol. 28, No. 2, 2015, pp. 346–356. https://doi.org/10.1016/J.CJA.2014.12.033, URL https://www.sciencedirect.com/science/article/pii/S1000936115000187.

[68] "4.2.8. Unsteady Aerodynamics — OpenFAST v4.0.2 documentation," , 2023. URL https://openfast.readthedocs.io/en/main/source/user/aerodyn/theory_ua.html#ua-notations.

[69] Sheng, W., Galbraith, R. A. D., and Coton, F. N., "A Modified Dynamic Stall Model for Low Mach Numbers," *Journal of Solar Energy Engineering*, Vol. 130, No. 3, 2008, pp. 0310131–03101310. https://doi.org/10.1115/1.2931509, URL https://dx-doi-org.tudelft.idm.oclc.org/10.1115/1.2931509.

[70] "OpenFOAM | Free CFD Software | The OpenFOAM Foundation," , 2025. URL https://openfoam.org/.

[71] (DHPC), D. H. P. C. C., "DelftBlue Supercomputer (Phase 2)," https://www.tudelft.nl/dhpc/ark:/44463/DelftBluePhase2, 2024.

[72] Israel, D., "The Myth of URANS," *Journal of Turbulence*, Vol. 24, No. 8, 2022, pp. 367–392. https://doi.org/10.1080/14685248.2023.2225140, URL http://arxiv.org/abs/2212.01313http://dx.doi.org/10.1080/14685248.2023.2225140.

[73] Heinz, S., "A review of hybrid RANS-LES methods for turbulent flows: Concepts and applications," *Progress in Aerospace Sciences*, Vol. 114, 2020, p. 100597. https://doi.org/10.1016/J.PAEROSCI.2019.100597, URL https://www.sciencedirect.com/science/article/pii/S0376042119301861.

[74] Menter, F., "Two-equation eddy-viscosity turbulence models for engineering applications," *arc.aiaa.org*, Vol. 32, No. 8, 1994, pp. 1598–1605. https://doi.org/10.2514/3.12149, URL https://arc.aiaa.org/doi/abs/10.2514/3.12149.

[75] Menter, F. R., Kuntz, M., and Langtry, R., "Ten years of industrial experience with the SST turbulence model," *Turbulence, heat and mass transfer*, Vol. 4, No. 1, 2003, pp. 625–632.

[76] "Menter Shear Stress Transport Model," , 2024. URL https://turbmodels.larc.nasa.gov/sst.html.

[77] Roache, P. J., "A method for uniform reporting of grid refinement studies," *ASME-publications-fed*, Vol. 158, 1993, p. 109.

[78] John W Slater, "Examining Spatial (Grid) Convergence," , 2021. URL https://www.grc.nasa.gov/www/wind/valid/tutorial/spatconv.html.

[79] "OpenFOAM: User Guide: Crank-Nicolson time scheme," , 2016. URL https://www.openfoam.com/documentation/guides/latest/doc/guide-schemes-time-crank-nicolson.html.

[80] "OpenFOAM: User Guide: Divergence scheme example," , 2016. URL https://www.openfoam.com/documentation/guides/latest/doc/guide-schemes-divergence-example.html.

[81] Warming, R. F., and Beam, R. M., "Upwind Second-Order Difference Schemes and Applications in Aerodynamic Flows," *https://doi-org.tudelft.idm.oclc.org/10.2514/3.61457*, Vol. 14, No. 9, 2012, pp. 1241–1249. https://doi.org/10.2514/3.61457, URL /doi/pdf/10.2514/3.61457?download=true.

[82] Golub, G. H., and Van Loan, C. F., "Matrix computations," 1996, p. 694. URL https://search.worldcat.org/title/844930332.

[83] "OpenFOAM: User Guide: pimpleFoam," , 2018. URL https://www.openfoam.com/documentation/guides/latest/doc/guide-applications-solvers-incompressible-pimpleFoam.html.

[84] Maskell, E. C., "A Theory of the Blockage Effects on Bluff Bodies and Stalled Wings in a Closed Wind Tunnel," , 11 1963.

[85] Barlow, J. B., Rae, W. H., and Pope, A., *Low-speed wind tunnel testing*, John wiley & sons, 1999.

[86] Spalart, P. R., "Strategies for turbulence modelling and simulations," *International Journal of Heat and Fluid Flow*, Vol. 21, No. 3, 2000, pp. 252–263. https://doi.org/10.1016/S0142-727X(00)00007-2, URL https://www-sciencedirect-com.tudelft.idm.oclc.org/science/article/pii/S0142727X00000072#aep-section-id16.

[87] Nived, M. R., Mukesh, B. S., Athkuri, S. S. C., and Eswaran, V., "On the performance of RANS turbulence models in predicting static stall over airfoils at high Reynolds numbers," *International Journal of Numerical Methods for Heat & Fluid Flow*, Vol. 32, No. 4, 2022, pp. 1299–1323. https://doi.org/10.1108/HFF-08-2021-0519, URL https://dx-doi-org.tudelft.idm.oclc.org/10.1108/HFF-08-2021-0519.

A

Visualisations of leading-edge vortex

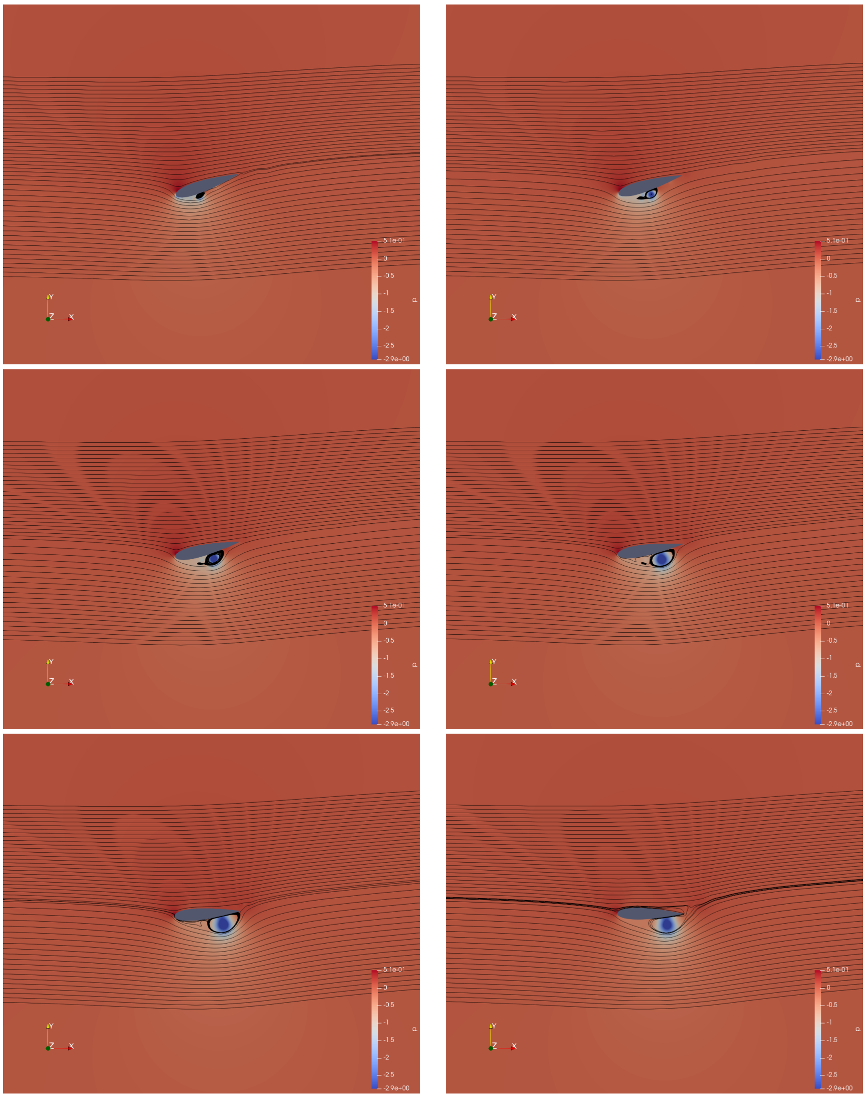

Figure A.1: Flow visualisations of the leading-edge vortex at an angle of attack of. Each row corresponds to a successive time instance on the downstroke, after the maximum angle of attack has been reached, illustrating the evolution of vortex convection.